A Closed-Loop EMG-Assisted Shoulder Model

THÈSE N^{O} 8658 (2018)

PRÉSENTÉE LE 29 JUIN 2018
À LA FACULTÉ DES SCIENCES ET TECHNIQUES DE L'INGÉNIEUR
PROGRAMME DOCTORAL EN ROBOTIQUE, CONTRÔLE ET SYSTÈMES INTELLIGENTS

ÉCOLE POLYTECHNIQUE FÉDÉRALE DE LAUSANNE

POUR L'OBTENTION DU GRADE DE DOCTEUR ÈS SCIENCES

PAR

Ehsan SARSHARI

acceptée sur proposition du jury:

Dr D. Gillet, président du jury
Prof. D. Pioletti, Dr Ph. Müllhaupt, directeurs de thèse
Prof. F. van der Helm, rapporteur
Prof. Ph. Büchler, rapporteur
Prof. K. Aminian, rapporteur

ÉCOLE POLYTECHNIQUE
FÉDÉRALE DE LAUSANNE
Suisse
2018

To my parents.

Acknowledgements

This thesis evolved hand in hand with me during the past four years. So many others helped in the thesis work in one way or another to whom I would like to express my thanks.

First, I express my deepest gratitude to my thesis directors, Dr. Philippe Müllhaupt and Prof. Dominique Pioletti, for giving me the opportunity to start my PhD at LA and LBO and supporting me. The interactions with Dr. Müllhaupt significantly assisted me in developing my problem solving skills. He persistently encouraged me to transform abstract concepts to tangible problems by cooking up toy examples. This often paid off in illustrative solutions and novel research ideas. He put his trust in me to work on my own way, and the door of his office was always open on me anytime I needed his expertise. I would like to thank the members of the jury, Prof. Frans van der Helm, Prof Philippe Büchler, Prof. Kamiar Aminian, and Dr. Denis Gillet for taking their time to review this thesis and making my defense an enjoyable closure to my PhD. A special mention to Prof. van der Helm for his constructive criticism and insightful comments. I would also like to thank Dr. Alexandre Terrier for his commitment to the project and his help in communicating my research across the biomechanics society. I would also like to thank Prof. Alain Farron from CHUV university hospital for overseeing the clinical side of my work. I thank my predecessor, Dr. David Ingram for helping me start off my PhD on the right track. I thank my teammates, Yasmine Boulanaache and Matteo Mancuso for the MRI segmentation and the measurements, respectively.

LA is well-known for its great atmosphere. I would therefore like to thank the members of the LA direction, Prof. Ronald Longchamp, Prof. Dominique Bonvin, and Prof. Colin Jones for their contributions in preserving this atmosphere and hosting me at LA. I would also like to thank Ruth, Virginie, Nicole, Francine, Eva, and Margot for facilitating administrative paperworks. I want to also thank all those who enriched my stay at LA and made it memorable. Philippe, for never giving up the chair of "Empty Head Research Group" and his constant aid in establishing the commercial university of "Vasco" in Moscow where people can grow old by exploring wacky ideas. Dr. Alireza Karimi, for all the coffee-break discussions and his outlook to life that served as a great source of inspiration for me. Dr. Christophe Salzmann, for his help in laboratory setups and IT, in particular during my collaborations with students on the inverted pendulum project. Sandra for her friendship and empathy. Christoph, Martand, Tafarel, and Petr, for being really good office partners, for always being ready for a good laugh, for sharing all the

ups and downs of the daily PhD life, and for all the time we spent while I was playing backgammon with Christoph. Luca, for being my gym guru and "pulling me down". Ioannis, for the good handshakes. Andrea, Milan, Tomasz, Georgios, Faran, Predrag, Altug, Diogo for the good humor and their friendships. Sanket; Renè; Harsh; Sohail; Mustafa; Pulkit; Ivan; Prabhat. Thank you to all my other lab-mates, please keep up the good spirit.

I am also grateful to my friends in and around Lausanne and elsewhere who provided great moments.

Finally, I would like to thank my family for their boundless love and support. I feel extremely blessed for having a family to whom I can turn anytime, being sure that they would support me in every means possible. My mom, Mehri, and my dad, Mohammad, words do not suffice to express my feelings for all the sacrifices you made on my behalf. Thank you for helping me focus on important things in life. I am thankful to my sweet sister, Azadeh, and my lovely brother, Amin, for being my lifetime mentors and always reminding me how to have a good laugh. I wish to thank my beloved wife, Mehrnoush, for all the love, support, and encouragement that she provided for me, even when I did not deserve it. Thank you for understanding the late-night and weekend workings. You got me so well through the smooth and the rough times. Thank you for being my dearest and best friend on every part of the way. Life wouldn't be the same without you.

Lausanne, 15 Jun 2018 Ehsan Sarshari

Abstract

The human shoulder is a complex musculoskeletal system. Knowledge about its kinematics and dynamics can help improve associated treatments. However, to date direct measurements of these quantities can be only granted through invasive investigations or expensive imaging techniques. Musculoskeletal shoulder models provide useful predictions of shoulder kinematics and dynamics. Nevertheless, there remain significant gaps between the model predictions and behaviors of the real system. This thesis aims at extending an existing shoulder musculoskeletal model for patient-specific clinical applications. To this end, number of improvements are considered.

The initial model only considered an outstretch arm. Therefore, the elbow and the muscles spanning it are added in the extended model. To this end, the bone morphologies of the ulna and the radius and muscles architectures are obtained from MRI scans. The elbow is modeled using two hinge joints replicating its flexion/extension and pronation/supination motions.

The model is developed based on anthropometric data of a single subject. Given anthropometric variabilities among subjects, it cannot predict inter-individual differences. Therefore, scaling routines are developed to scale the model to a specific subject. The model's bone segment inertial properties, skeletal morphologies, and muscles architectures are scaled according to any specific subject. The effects of anthropometric parameters on glenohumeral (GH) joint reaction force predictions are evaluated.

Humeral head translations (HHT) play a crucial role in the GH joint functions. Given that the model is developed based on inverse dynamics, it falls short of predicting the HHT. Therefore, a framework is developed allowing forward-dynamics simulation of the model with a six DOF GH joint. A deformable articular contact is included in the framework defining the GH joint contact force in terms of the joint rotations and translations.

A videogrammetry systems is used for recording upper extremity motions. It measures trajectories of skin-fixed markers. However, it cannot practically track scapula motions and the GH joint center. Therefore, a method is developed estimating the GH joint center and consequently scapula motions. Multi-segment optimization is used to reconstruct the measured motions in terms of joints angles.

A musculotendon model is a key component for muscle-driven applications of the model. A Hill-type musculotendon model is developed. However, the initial state of the Hill-type model is not provided. Therefore, singular perturbation analysis is used to propose a method providing an initial state for the developed Hill-type model.

Given that the model is over-actuated, an optimal load-sharing is used to predict muscle forces. It overlooks antagonistic muscle co-contractions. However, muscle co-contractions play crucial roles in the GH joint stability. Therefore, the load-sharing is modified such that measured electromyography (EMG) data can be incorporated. It is hypothesized that inclusions of the measured EMG can improve model predictions of muscle co-contractions.

The developed model provides predictions of joints angles, muscles forces, and GH joint force and translations that are in good agreements with *in vivo* studies. It could be populated with pre/post operative patients of total shoulder arthroplasty to answer clinical questions regarding treatments of GH joint osteoarthritis.

Keywords: Upper extremity musculoskeletal model, scaled-generic model, forward-dynamics, humeral-head translations, multi-segment optimization, Hill-type musculotendon model, EMG-assisted, over-actuated systems

Résumé

L'épaule humaine est un système musculo-squelettique complexe. La connaissance de sa cinématique et de sa dynamique peut aider à améliorer les traitements associés. Cependant, à ce jour, les mesures directes de ces quantités ne peuvent être obtenues que par des investigations invasives ou des techniques d'imagerie coûteuses. Les modèles musculo-squelettiques de l'épaule fournissent des prédictions utiles sur la cinématique et la dynamique de l'épaule. Néanmoins, ils subsistent des écarts significatifs entre les prévisions du modèle et les comportements du système réel. Cette thèse vise à étendre un modèle musculo-squelettique existant de l'épaule pour des applications cliniques futures sur une cohorte de patients. À cet égard, plusieurs améliorations sont considérées.

Le modèle initial ne considére qu'un bras tendu. Par conséquent, le coude et les muscles qui l'entourent sont ajoutés dans le modèle étendu. À cette fin, les morphologies osseuses de l'ulna et du radius, et les architectures de muscles sont obtenues à l'aide de l'IRM. Le coude est modélisé en utilisant deux articulations de charnière reproduisant ses mouvements de flexion/extension et de pronation/supination.

Le modèle est développé sur la base de données anthropométriques d'un seul sujet. Étant donné les variabilités anthropométriques entre les sujets, il ne peut prédire les différences interindividuelles. Par conséquent, des routines de mise à l'échelle sont développées pour adapter le modèle à un sujet spécifique. Les propriétés inertielles du segment osseux du modèle, les morphologies squelettiques et les architectures musculaires sont mises à l'échelle en fonction de tout sujet spécifique. Les effets des paramètres anthropométriques sur les prédictions de force de réaction articulaire glénohumérale (GH) sont évalués.

Les translations de la tête humérale (TTH) jouent un rôle crucial dans les fonctions de l'articulation GH (Gluno-Humérale). étant donné que le modèle est développé en fonction de la dynamique inverse, il ne permet pas de prédire le TTH. Par conséquent, un cadre est développé permettant la simulation modele dynamique anticipatif du modèle avec une articulation GH à six DDL (degré de liberté). Un contact articulaire déformable est inclus dans le cadre définissant la force de contact de l'articulation GH en termes de rotations et translations articulaires.

Un système de vidéogrammétrie est utilisé pour enregistrer les mouvements des extrémités supérieures. Il mesure les trajectoires des marqueurs fixés à la peau. Cependant, il ne peut pas pratiquement suivre les mouvements de l'omoplate et le centre de l'articulation GH. Donc, une méthode est développée estimant le centre de l'articulation GH et ensuite les mouvements de l'omoplate. L'optimisation multi-segments est utilisée pour reconstruire les mouvements mesurés en termes d'angles d'articulations.

Un modèle musculotendon est un élément clé pour les applications du modèle où l'aspect moteur du muscle domine. Un modèle musculotendon de type Hill est développé. Cependant, l'état initial du modèle de type Hill n'est pas fourni. Par conséquent, l'analyse de perturbation singulière est utilisée pour proposer une méthode fournissant un état initial pour le modèle de type Hill développé.

Vue que le modèle est suractionné, un partage de charge optimal est utilisé pour prédire les forces musculaires. Il néglige les co-contractions des muscles antagonistes. Cependant, les co-contractions musculaires jouent un rôle crucial dans la stabilité de l'articulation GH. Par conséquent, le partage de charge est modifié de telle sorte que des données mesurées d'électronographie (EMG) puissent être incorporées. Il est supposé que les inclusions de l'EMG mesurée peuvent améliorer les prédictions modèles des co-contractions des muscles.

Le modèle développé fournit des prédictions des angles des articulations, des forces musculaires et de la force et les translations de l'articulation GH qui sont en bon accord avec les études in vivo. Il pourrait être peuplé de patients pré/post opératoires d'arthroplastie totale de l'épaule pour répondre aux questions cliniques concernant les traitements de l'arthrose de l'articulation GH.

Mots-clés : Le modèle musculo-squellettiques des extrémités supérieures, le modèle générique à l'échelle, le modele dynamique anticipatif, les translations de la tête humérale, l'optimisation multisegment, le modéle musculotendon type Hill, EMG-assisté, les systèmes suractionné

Contents

Acknowledgements **v**

Abstract (English/Français) **vii**

List of figures **xiii**

List of tables **xvi**

List of abbreviations **xix**

1 Introduction **1**
- 1.1 Research context . . . 1
- 1.2 State-of-the-art . . . 3
  - 1.2.1 Forearm kinematics . . . 3
  - 1.2.2 Subject-specific modeling . . . 3
  - 1.2.3 Humeral head translations . . . 5
  - 1.2.4 Upper extremity kinematics . . . 6
  - 1.2.5 Musculotendon dynamics . . . 7
  - 1.2.6 Load-sharing . . . 8
- 1.3 Contributions . . . 9
- 1.4 Thesis organization . . . 11

2 A Matlab toolbox for scaled-generic modeling of shoulder and elbow **13**
- 2.1 Introduction . . . 14
  - 2.1.1 Motivation . . . 14
  - 2.1.2 State-of-the-art . . . 15
  - 2.1.3 Research method . . . 16
- 2.2 Methods . . . 17
  - 2.2.1 Elbow kinematics . . . 17
  - 2.2.2 Elbow dynamics . . . 20
  - 2.2.3 Integration of the elbow model into the shoulder model . . . 21
  - 2.2.4 Model scaling . . . 23
  - 2.2.5 Shoulder and elbow Matlab toolbox . . . 27
  - 2.2.6 Parameter study . . . 28

2.3 Results 28
2.4 Discussion 31

3 A Simulation Framework for Humeral Head Translations 41
3.1 Introduction 42
3.2 Methods 43
  3.2.1 Indeterminacy in HHT 44
  3.2.2 Resolving the indeterminacy: deformable articular contact 45
  3.2.3 Resolving the indeterminacy: forward-dynamics simulation 47
  3.2.4 Simulation of the framework 49
3.3 Results 50
3.4 Discussion 54

4 Motion reconstruction in upper extremity in the absence of scapula kinematics measurement-devices 59
4.1 Introduction 60
4.2 Methods 62
  4.2.1 Kinematic model 62
  4.2.2 Measurements 65
  4.2.3 Estimation of GH, TS, and AI 65
  4.2.4 Multi-segment optimization 67
  4.2.5 Evaluation scenarios 67
4.3 Results 69
4.4 Discussion 72

5 An initialization technique for Hill-type musculotendon models 75
5.1 Introduction 76
5.2 Methods 77
  5.2.1 Hill-type musculotendon model 78
  5.2.2 Contraction dynamics 79
  5.2.3 Initialization 83
  5.2.4 Evaluation of the method 84
5.3 Results 85
5.4 Discussion 87

6 EMG-Assisted Load-Sharing for Muscle Force Prediction in Upper-Extremity 91
6.1 Introduction 92
6.2 Methods 93
  6.2.1 Upper extremity Musculoskeletal model 94
  6.2.2 Measurements 96
  6.2.3 Multi-segment optimization 97
  6.2.4 Musculotendon model 98

6.2.5 EMG-assisted load-sharing 100
6.2.6 Evaluations of the model 101
6.3 Results 102
6.3.1 Muscle forces 102
6.3.2 JRF 105
6.3.3 SR and intersection foci 105
6.4 Discussion 106

7 Conclusions **113**
7.1 Summary 113
7.2 General discussion 114
7.3 Perspectives 118

Bibliography **138**

Curriculum Vitae **139**

List of Figures

1.1 A block diagram summary of the thesis 12

2.1 Elbow MRI scans and kinematic model 19
2.2 The developed shoulder and elbow model 22
2.3 Scaling ribcage ellipsoids 25
2.4 Adapting glenoid inclination and version 27
2.5 Evaluations of the effects of subject specific parameters 30
2.6 The developed Matlab toolbox 34
2.7 The subject-specific tool 35
2.8 The muscle wrapping tool 36
2.9 The kinematics tool 37
2.10 The kinematics tool, option 2 38
2.11 The moment arms tool 39
2.12 Force prediction tool 40

3.1 A schematic view of the GH joint 44
3.2 The GH joint with deformable articular contact 47
3.3 A block diagram representation of the developed framework 50
3.4 Humeral head translations estimated by the model 52
3.5 The GH joint contact force predicted by the model 53
3.6 Contact pressure estimated by the model 53
3.7 Maximum normal strain predicted by the model 54

4.1 MRI scans and the developed kinematic model 64
4.2 GH joint center estimation 66
4.3 Model estimations for the GH joint center 70
4.4 Reconstructed motion in terms of joins angles 71

5.1 A block diagram representation of the developed initialization technique . 78
5.2 Musculotendon model and its normalized functions 82
5.3 Effect of the initial state on musculotendon response 84
5.4 Reproductions of the experimentally measured forces 86
5.5 Force predicted by the developed model for the middle deltoid 87

6.1 MRI scans and developed musculoskeletal kinematic model 95
6.2 An illustration of the developed model 98
6.3 Block diagram of the EMG-assisted load-sharing 102
6.4 Muscle forces predicted by EALS and SLS 104
6.5 JRF predicted by EALS and SLS 105
6.6 SR and intersection foci from EALS and SLS 106
6.7 Complete set of muscle forces predicted by EALS and SLS 110
6.8 Complete set of muscle forces predicted by EALS and SLS 111

List of Tables

2.1 Scaling bone segment inertial properties 24

List of Abbreviations

AA	Angulus Acromialis
AC	Acromioclavicular
AG	Anterior Glenoid
AI	Angulus Inferior
BMI	Body Mass Index
BSIP	Bone Segments Inertial Properties
C7	7th Cervical Vertebra
CE	Contractile Element
CNS	Central Nervous System
DOF	Degree of Freedom
EALS	EMG-Assisted Load-Sharing
EE	Elastic Element
EL	Epicondyle Lateral
EM	Epicondyle Medial
EMG	Electromyography
GC	Glenoid Center
GH	Glenohumeral
GUI	Graphical User Interface
HHT	Humeral Head Translations
HU	Humeroulnar
IG	Inferior Glenoid
IJ	Incisura Jagularis
Is	Infraspinatus
JRF	Joint Reaction Force
MRI	Magnetic Resonance Imaging
MSPE	Mean Squared Prediction Error
MVC	Maximum Voluntary Contractions
NRMSE	Normalized Root Mean Square Error
ODE	Ordinary Differential Equation
PCSA	Physiological Cross Section Area
PDE	Partial Differential Equation
PE	Passive Elastic Element
PG	Posterior Glenoid

PX	Process Xiphoideus
RC	Rotator Cuff
RS	Radial Styloid
RU	Radioulnar
SC	Sternoclavicular
Sc	Subscapularis
SG	Superior Glenoid
SKMD	Scapula Kinematics Measurement-Device
SLS	Standard Load-Sharing
SR	Stability Ratio
Ss	Supraspinatus
T8	8th Thoracic Vertebra
Tm	Teres Minor
TS	Trigonum Scapulae
TSA	Total Shoulder Arthroplasty
US	Ulnar Styloid

1 Introduction

1.1 Research context

Since 1970, the world has grown considerably older by gaining more than 10 years of life expectancy in overall [1, 2]. This has been achieved by a shift in contributors to world's health burden from infectious disease causing premature mortalities to chronic diseases and injuries such as musculoskeletal disorders [2]. The health burden intensifies as people become older, and consequently they spend more years living with injuries. The situation however can be mitigated regarding musculoskeletal disorders, if our techniques for pathology prevention, treatment, and rehabilitation planning are improved [3]. In order to achieve the desired improvements, extensive and in depth knowledge of internal interactions between bones and soft tissues and the role played by each one in acquiring joints mobility and stability is required [4–6]. Unfortunately, to date this knowledge cannot be yet granted, except through non-invasive investigations and expensive imaging techniques [7, 8]. However, musculoskeletal models can alternatively help fill the lack of knowledge by providing quantitative information [9].

Musculoskeletal models treat the musculoskeletal systems as cable-driven mechanical mechanisms [10, 11]. I.e. the bone segments are considered as rigid-body links, the muscles as massless elastic cables wrapping around the bones, and joints as ideal mechanical joints with different degrees of freedom (DOF). The models are therefore developed based on the laws and theories of multibody dynamics. Several musculoskeletal models have been developed for different anatomical sites of human body, including upper extremity [12–19], lower extremity [20–24], and spine [25–27]. They are established tools and strategies that provide quantitative information about joints kinematics and kinetics. Therefore, they play an increasingly crucial role in biomechanics [28–30].

The glenohumeral joint of upper extremity is the most dislocated joint in the human body [31]. It also has the highest average duration of temporary "total disability to work" with respect to other joints (37 days vs 26 days on average) [4]. Furthermore, using statistical analyses it was shown that the demand for its replacement (total shoulder arthroplasty) would continue to grow, even comparing to hip and knee arthroplasties [3, 32]. Therefore, musculoskeletal modeling of the upper extremity is attracting special attentions since last two decades.

Several musculoskeletal models were developed for the upper extremity. Very simplistic shoulder specimens in which muscle segments were replaced by threads were among the introductory attempts to model the upper extremity [33, 34]. Two dimensional models were next developed [35, 36]. The work by [37, 38] were the first models to represent the upper extremity as a mechanical mechanism in three dimensional (3D) space. However, the primary work of [12], known as the Swedish model today, was the first complete representation of upper extremity that included relative motions of scapula and ribcage and accounted for muscle paths. Finally, the pioneering work of [39, 40] that was a continuation of the kinematic model of [41] was the first comprehensive 3D model for upper extremity. Its development was continued through several studies [13, 42, 43], and it is now known as the Delft shoulder and elbow model. Other musculoskeletal models were also developed, including the Garner and Pandy model [14], the Anybody model [15, 44], the Opensim model [45], the UK National shoulder model [16], the Waterloo model [46], the Case model [47], the Portuguese model [17], and the models developed in Swiss Institute of Technologies in Zurich (ETHZ) [18] and in Lausanne (EPFL) [19, 48]. Comprehensive reviews of these models regarding their dynamics and kinematics are available in [49, 50] and [28, 51], respectively.

These models were extensively used for several applications concerning analysis the causes of musculoskeletal pathologies [19, 52], increasing performance or enhancing function specially in sport biomechanics and ergonomics [53–55], implant design [5, 56], improving rehabilitations planning [57, 58], development of neuroprosthetic systems [47, 59, 60], injury prevention [61], pre-surgical planning [62, 63], predicting surgical outcome [6, 64], and improving diagnosis of musculoskeletal disorders [9, 65].

Nevertheless, there remain significant gaps between predictions of musculoskeletal models of upper extremity and the performance of their respective physiological system [4, 28–30, 66]. Therefore, their realism must be considerably enhanced, before they can be considered as routinely exploitable clinical tools. The following section is a summary of the state-of-the-art of musculoskeletal modeling of the upper extremity. It provides a critique of the current progress and is organized in terms of 6 categories, including forearm kinematics (Subsection 1.2.1), subject-specific modeling (Subsection 1.2.2), humeral head translations (Subsection 1.2.3), upper extremity kinematics (Subsection 1.2.4), musculotendon dynamics (Subsection 1.2.5), and muscles forces prediction (load-sharing) (Subsection 1.2.6).

1.2 State-of-the-art

1.2.1 Forearm kinematics

Successful clinical applications of a musculoskeletal model of upper extremity required the model to include all major joints and muscles of the upper extremity [4, 28]. Neglecting a joint or a muscle group could alter its biofidelity and consequently posed limitations on its clinical applications. Some of the above-mentioned upper extremity models including the Swedish model [12] and the model that has been developed recently in our laboratory (EPFL model) [19] only include an outstretched arm. Therefore, these models neglect the elbow kinematics and consequently the muscle groups spanning the elbow itself and the shoulder (e.g. biceps and triceps). Nevertheless, the importance of elbow kinematics on upper extremity kinematics and kinetic was already highlighted [42, 67–69]. Biceps and triceps were shown to play a crucial role in active stability of glenohumeral joint [70–73].

Given the complex multiple DOF kinematics of forearm, there is no consensus in the literature concerning its modeling [50, 69]. Its multiple DOFs result in two distinguishable movements including extension/flexion and pronation/supination. A very simplistic cardanic joint was used to model the two movements of the forearm [74]. However, it was not realistic given that contrary to cardanic joints, the axes of rotations of forearm movements are not perpendicular [75]. Other studies used two non-perpendicular hinge joints [42, 76–79]. But, they yet considered a single body to represent two bone segments of the forearm (ulna and radius) and therefore neglected their interplay [80]. The sophisticated interplay of ulna and radius during forearm pronation/supination was addressed using MRI imaging [81, 82]. More complicated elbow models were developed considering a closed-kinematic chain [79, 80, 83]. They provided detailed representations of forearm kinematics, although they required more individualized parameters of the forearm that could not be readily obtained. They avoided an unrealistic tilt of the wrist relative to forearm during pronation/supination that often occurred with conventional two hinge joint models [80, 84].

1.2.2 Subject-specific modeling

A vast majority of the available musculoskeletal models developed for the upper extremity are generic models. I.e. they were developed based on anthropometric data of a single subject or cadaver. Therefore, given anthropometric variabilities among subjects [85], they fall short of predicting inter-individual differences. On the other hand, obtaining anthropometric data of each understudy subject, for instance using imaging techniques, is both time-consuming and expensive [85, 86]. Therefore, development of subject-specific musculoskeletal models in which all the model anthropometric data are personalized for the specific understudy subject is not yet feasible. Alternatively, scaling techniques are used that scale a generic model to each understudy subject [42, 87].

In order to adapt generic upper extremity musculoskeletal models to specific subjects, several aspects of the models must be scaled. This includes bone segments inertial properties (BSIP), skeletal morphologies, and muscles architectures and properties [88].

Several studies used predictive equations developed in [89–91] to scale BSIP [16, 42, 92]. These predictive equations were developed based on investigations of large groups of living subjects and cadavers. However, they require further adjustments to accurately scale BSIP in 3D coordinate systems. The predictive equations of [93, 94] were recently adjusted in [95] to provide 3D applicable regression equations to scale BSIP.

Scaling skeletal morphologies of upper extremity models are more challenging [96]. Isotropic scaling factors that equally scale the skeletal morphology in 3D were used [16, 42, 97]. However, this implied an unrealistic uniform scaling between different individuals [89], and furthermore they can lead to uncontinuous kinematics [97]. Anisotropic scaling factors provided more realistic scaling [98, 99]. However, they can cause non-anatomical configurations of bone segments that consequently result in infeasible kinematic solutions. This is mainly due to relative movements of scapula with respect to ribcage that make the upper extremity a closed kinematic chain [100]. Isotropic scaling factors were defined by comparing subjects' arm length to the arm length of a generic model [42]. Anisotropic scaling factors were used to scale ribcage, clavicle, and scapula while a soft constraint was used for constraining scapula motions relative to ribcage [98]. However, the choice of weighting factors for the soft constraints was not straightforward, and non-anatomical configurations of scapula relative to ribcage could be reached. A more advanced scaling for skeletal morphology was used in [92]. It was based on anisotropic scaling factors together with an optimal scaling of an ellipsoid approximating ribcage. On the other hand, effects of glenoid inclination and version on model force predictions and joint translations were already highlighted [64, 101, 102]. However, their adaptations to each understudy subject were not addressed in upper extremity musculoskeletal models.

Scaling muscles architectures and properties includes defining scaling factors for their origins/insertions, wrapping objects, muscles physiological cross section areas (PCSA), and other musculotendon parameters [103].

Three different approaches were used to scale muscles origins/insertions, including linear bone mapping [104, 105], anisotropic bone morphing [106–108], and statistical bone morphing [109, 110]. Linear mappings were introduced based on positions of few bony landmarks [104, 105]. They approximated muscles origins/insertions for a specific subject by rotating their corresponding origins/insertions from a generic model. However, their approximation could be considerably improved by considering not only rotations but also translations, scaling, and bone deformation in the mappings. This was achieved by development of anisotropic bone morphings [106–108]. However, they required complete bone morphologies of each understudy subject that could be obtained only by imaging techniques. Statistical bone morphing methods were developed based on investigating statistical shape variations of bone morphologies [109, 110]. They also required at least part of the bone morphologies from each understudy subject.

Scaling of wrapping objects were not found at least explicitly in any of the aforementioned available musculoskeletal models of upper extremity. However, the path taken by muscles defined by their wrapping objects and origins/insertions can considerably alter their moment arms and therefore model predictions [111, 112].

The total muscle bulk of upper extremity obtained from MRI scans of each subject was used to define a scaling ratio for PCSA scaling [113, 114]. However, the dependency on MRI scan might affect its practical use. Another PCSA scaling ratio was defined by comparing the BMI (body mass index [115]) of an understudy subject to that of a generic model [42]. However, direct association of BMI with total muscle bulk and therefore PCSA was arguable [116]. A predictive equation based on BMI was introduced in [117] that defined fat/muscle percentage of body composition. Scaling of other musculotendon parameters were addressed by using isotropic scaling factors [118].

1.2.3 Humeral head translations

A vast majority of the aforementioned upper extremity models were developed based on inverse dynamics, e.g. [12–16, 19, 39, 44–47]. In inverse dynamics the muscle forces are defined for a given (measured) joints kinematics. However, with the available measurement techniques, it is not straightforward to measure the translational DOF of the GH joint [8]. Therefore, it is often approximated as an ideal ball-and-socket joint in the musculoskeletal models, neglecting its translations [119]. Nonetheless, the GH joint translations has a key impact on the GH joint function, specially its stability mechanism [28, 120]. Furthermore, predictions of the GH joint translations, the contact pressure, and the contact areas are required in designing shoulder prostheses [121, 122].

Indeed, few studies have investigated the humeral head translations (HHT) using biomechanical models. To this end, they tailored either available musculoskeletal models [122, 123] or developed finite element models [119, 121, 124, 125]. Other studies mainly used cadaveric [126, 127] or clinical [8, 128–133] approaches to address the GH joint translations. However, there are limitations associated to each of these studies.

The Anybody shoulder model [44] was tailored using the force dependent kinematic method, introduced in [134], to address the HHT after total shoulder arthroplasty (TSA) [122]. The dynamic effects of motion were neglected although their influence on the HHT has been already highlighted [128]. The Portuguese shoulder model [17] was adapted in [123] to address the HHT using a novel inverse-dynamics framework. The HHT was considered as an extra design variable in an optimization scheme within this framework. Despite [122], the dynamic effects of motion were partially considered. However, the articular contact was approximated by an elastic potential function. This deviates from the nonlinear and viscoelastic behavior of the cartilage [135] and does not account for the moment applied on the humerus due to the articular contact. The different 3D finite element models developed in [119, 121, 124, 125] share the same attributes. They include more realistic estimation for the articular contact although they were simulated under a sequence of static conditions, neglecting the dynamics of motion. Furthermore, they all lack a physiological muscle force load-sharing. The 3D finite element model developed in [119] was used in [120, 136, 137] to further study the HHT after the TSA.

The *in vivo* or *in vitro* measurement of the HHT remains a challenging task [8]. Specifically, *in vitro* studies cannot accurately simulate the *in vivo* conditions in terms of the muscle and joint contact forces. The *in vivo* studies are also either limited to 2 dimensional analysis [128, 129] or otherwise their accuracy is limited by the 3D reconstruction of the bones [8, 132, 133]. Furthermore, they are not developed to assess the GH joint translations during dynamic activities [130, 131].

1.2.4 Upper extremity kinematics

Pathologies of upper extremity are correlated to its kinematic dysfunctions [138, 139]. Therefore, accurate estimations of upper extremity kinematics are essential for clinical applications. Furthermore, inaccurate estimations of upper extremity kinematics can alter the kinetic estimations obtained using biomechanical models [49].

Videogrammetry systems are extensively used for noninvasive measurements of upper extremity kinematics [91]. They track the trajectories of skin-fixed palpated markers. These markers are placed on the bony landmarks used to define the spatial configuration of each bone segment in a kinematic model. The markers trajectories are subject to relative movements of the skin with respect to their underlying bony landmarks (soft tissue artifacts) [140]. For instance, up to 48% of the humeral axial rotation was shown to be influenced by soft tissue artifacts [141]. Therefore, a so-called multi-segment optimization is used to exclude the effects of soft tissue artifacts [74, 142]. It reconstructs a measured motion by minimizing a cost function, while taking into account the interactions between different upper extremity bone segments [50]. The cost is defined as the overall Euclidean distance between all the measured markers and the model defined landmarks. Therefore, evaluations of the cost require a one-to-one association between the bony landmarks in the kinematic model and the palpated skin-fixed markers. However, it is not possible to palpate all the bony landmarks required in the kinematic model. Glenohumeral joint center (GH) is one such landmark, given that it is not a physical landmark. More specifically, GH is the center of a sphere that approximates the humeral head [143].

Several methods have been developed to estimate the GH positions during upper extremity movements. They can be broadly divided into two categories, namely formal methods [144–149] and predictive methods [150–153]. The formal methods estimate the

GH positions by finding either the closet point to all the instantaneous helical axes of humerus [144–147] or the center of a sphere passing through humerus markers [148, 149]. The predictive methods provide estimations of GH positions either through regressive equations between scapula markers and GH positions [150–152] or generic offsets from one of scapula markers [152, 153]. The formal methods provide more accurate estimations of GH positions and are therefore preferred over predictive methods whose accuracy drops significantly during dynamic motions [147, 152]. Furthermore, given that the predictive methods developed based on anthropometry studies, they fall short of replicating inter-individual differences [152]. However, the main limitation of the formal methods is that they require measuring scapula kinematics. A majority of the predictive methods also require scapula kinematic measurements, otherwise their estimations are impractical (±5 cm error) [153].

Noninvasive measurements of scapula kinematics on the other hand are not yet straightforward [154]. Given that the scapula is heavily masked by soft tissues, it cannot be adequately tracked by its skin-fixed markers [155]. More specifically, soft tissue artifacts can reach up to 8.7 cm on scapula [156]. However, there are alternative methods to measure scapula kinematics. An intracortical bone-fixed pin drilled into scapula was introduced [157], although it was invasive and compromised the motion by causing pain. Regressive equations were also introduced providing estimations of scapula kinematics based on thoracohumeral joint angles [45, 46, 158–161]. However, information of thoracohumeral joint angles required *a priori* knowledge of GH positions. Furthermore, their accuracy was limited to small range of motions. Manual palpation of the scapula surface and application of a so-called scapula locator fixture were proposed in [162, 163] and [164, 165], respectively. However, they are neither time efficient nor practical during dynamic motions [166]. A marker tree including three markers was fixed to the acromion to track scapula [167]. However, this so-called acromion marker cluster tended to move medially with skin during abduction [168] and was very sensitive to its initial placement [169].

1.2.5 Musculotendon dynamics

Musculotendons are the interface between the central nervous system (CNS) and the articulated skeletal system. They transform neural excitation received from the CNS to forces that are applied to the skeletal system in order to perform a motor task. Therefore, a musculotendon model that can reproduce musculotendon forces for given musculotendon properties is a key component in simulations of coordinated movements [170, 171].

There exist several musculotendon models that can be broadly divided into two categories based on their development approaches, including (1) Huxley-based [172–174] and (2) Hill-type [170, 175–178] models. The former is developed based on a reductionist approach that takes into account physiological microscopic properties of tissues. It provides a distributed-parameter model of musculotendon using either a single partial differential equation (PDE) [172, 173] or a set of ordinary differential equations (ODE) [174]. In contrast, Hill-type models are developed based on a black-box description of input-output behaviors of musculotendon and its phenomenological properties. It results in a lumped-parameter model represented as a single ODE [170, 178].

The type of the model utilized depends on the goal of the simulation [171]. Given that several musculotendons are typically involved in simulations of coordinated movements [43], applications of Huxley-based models immediately become computationally demanding. Furthermore, they require several number of musculotendon parameters that are not straightforward to identify [179]. Therefore, the use of Hill-type models in simulations associated with coordinated movements are justified [170, 171].

The resulting ODE from a Hill-type model typically associates the muscle fiber velocity to a function of muscle fiber length, musculotendon length, and neural excitation [170, 175]. However, the initial state (muscle fiber length at the initial time) required to solve this ODE is not granted by the model. The procedure of estimation an initial state corresponding to a given musculotendon length and neural excitation for a Hill-type model is called initialization [171, 180]. Although, Hill-type models were extensively used in simulations of coordinated movements [21, 43], a limited effort was made regarding their initialization techniques. Nevertheless, forces reproduced by a Hill-type model can be considerably disturbed by the initialization, specially their transient behaviors [171, 181–183].

There are indeed few studies who investigated initialization techniques for Hill-type models. Musculotendon velocity was acquired and apportioned between the muscle fiber and tendon according to their linearized compliances [180, 184]. An initial state was then estimated by using the resulted muscle fiber velocity in the kinematic model of the musculotendon. However, the initialization was subject to singularities of the relative stiffness of muscle fiber and tendon. Furthermore, the estimated initial state might lack biophysical correspondence.

1.2.6 Load-sharing

While noninvasive measurement of muscle forces remains an elusive goal [185], musculoskeletal models provide predictions of muscle and joint forces. In available musculoskeletal models net joint moments are calculated for a given joint kinematics through inverse dynamics [14, 22, 100]. There are more muscles available than the degrees of freedom of the joints (over-actuation). Therefore, a standard load-sharing (SLS) scheme is commonly casted for optimal distribution of the net joint moments among muscles [52, 186]. The SLS predicts muscle forces by optimizing an efficiency-based physiological cost function subject to constraints. The constraints are associated with the net moment equilibrium, muscle forces upper/lower bounds, and joints stability [39]. However, given that antagonistic muscles are counterproductive in the net joint moments, SLS overlooks muscle co-contractions [26, 187–189] and consequently underestimates joint contact forces [43, 190, 191]. Nonetheless, model predictions of muscle and joint forces can be improved by considering muscle co-contractions, especially in upper extremity joints where stability is mainly achieved through muscle co-contractions [67, 192, 193].

For upper extremity, few studies investigated numerical approaches to improve muscle force predictions by accounting for co-contractions. They enforced co-contractions either by tailoring the optimization scheme of SLS [39, 194, 195] or by explicit use of measured EMG data [43, 188, 196–198]. However, there were limitations associated to each of these studies.

Co-contraction was promoted by introducing shift parameters [194] and negative weighting factors [195]. They were used to alleviate the SLS cost function growth due to antagonistic muscles activities (co-contractions). The choice of shift parameters and weighting factors required *a priori* knowledge of antagonistic muscles. However, this was not straightforward to achieve, given the three dimensional multi-joint morphology of upper extremity. Furthermore, in upper extremity, muscles could act simultaneously as agonistic and antagonistic throughout the motion. A stability constraint was introduced for glenohumeral joint [39] and commonly used in upper extremity musculoskeletal models [14, 100]. It constrained SLS solutions such that resulted glenohumeral joint reaction forces (JRF) always point towards the glenoid fossa. Co-contractions were therefore enforced by compromising the SLS optimal solution. However, the model underestimated the co-contractions [43].

Explicit use of measured EMG data in models did not require further information of antagonistic muscles. It could therefore provide rather straightforward predictions of muscle co-contractions [43, 188, 196–198]. However, the relationship between predicted muscle forces and measured EMG data was over-simplified [188, 196–198]. This deviated from the nonlinear dynamical behavior of the musculotendon actuator [170]. Furthermore, the resulted moment produced by direct applications of measured EMG failed to satisfy the net moment equilibrium [188, 196, 197]. Therefore, the predicted co-contractions might lack a physiological correspondence. Several combinations of measured EMG data were used in [43] to predict a joint reaction force closer to experimental results of [199]. However, the model did not allow inclusion of all the 14 measured EMG data and only a subset of them (4 muscles) were used.

1.3 Contributions

This thesis aims at extending an existing shoulder musculoskeletal model (EPFL shoulder model [19]) for patient-specific clinical applications. To this end, number of improvements are considered as follows.

- The full kinematics of the forearm including 2 DOFs for flexion/extension and pronation/supination are incorporated into the model. The forearm is modeled using two non-perpendicular hinge representing the humeroulnar and radioulnar distal/proximal joints. Both ulna and radius are considered as distinguished bone segments. Eight muscle groups, that were previously neglected, are added.
- Subject-specific attributes are considered to adapt different generic properties of the model to those of an understudy subject through scaling. BSIP is scaled by 3D regression equations of [95]. A method is developed for scaling skeletal morphologies of the model based on subject's height and shoulder width. Muscles origins/insertions as well as their wrapping objects are also scaled accordingly. The regression equation of [117] is used to scale muscles PCSAs according to body muscle percentage. The glenoid inclination and version are also included in the model. Furthermore, in order to facilitate clinical applications of the model a graphical user interface (GUI) is also developed exempting users from cumbersome programming.
- A framework that allows forward-dynamics simulation of the model including a 6 DOF GH joint is developed. It provides a straightforward solution to the HHT problem. We show that even within a forward-dynamics simulation addressing the HHT requires further information about the contact. To that end, a deformable articular contact is included in the framework defining the GH joint contact force in terms of the joint kinematics.
- Videogrammetry based measured motions of the upper extremity in the absence of scapula kinematics measurement-devices are reconstructed. To this end, a method is proposed to first estimate the GH positions independent of the scapula kinematics. It requires trajectories of few palpated markers and an MRI scan of the glenohumeral joint from the understudy subject. Scapula kinematics are then defined from the provided estimations of the GH positions.
- An initialization technique for a Hill-type model that avoids artificial transient behaviors is developed. To this end, it is shown that the contraction dynamics of a Hill-type model is a singular perturbed system. The singular perturbation analysis is therefore applied on the system in order to define an approximation of its central solution. The initial value of the approximated central solution is then used as an initial state for the contraction dynamics.
- Muscle co-contractions are promoted in the model by incorporating measured EMG data into the model. To this end, an EMG-assisted load-sharing (EALS) scheme is developed. Muscle forces associated with measured EMG of 15 superficial muscles are calculated and fed into the model. The EMG-based estimated muscle forces are used as upper/lower bounds on feasible solutions of the EALS.

1.4 Thesis organization

The reminder of the thesis is organized as follow. Chapter 2 presents our approach in adding subject-specific attributes to the model. It also details the incorporation of the forearm in the model and development of its GUI. Chapter 3 explains a framework for addressing humeral head translations within upper-extremity musculoskeletal models. A non-invasive approach for reconstructing scapula kinematics and consequently upper extremity kinematics is developed in Chapter 4. Musculotendon dynamics in general and a specific approach for their initializations are the subject of Chapter 5. Finally, in Chapter 6, different pieces developed in the previous chapters are placed together to provide an EMG-assisted Load-sharing scheme for addressing muscle co-contractions. Chapter 7 provides a summary/conclusion of the work and suggests recommendations for future improvements in upper-extremity musculoskeletal modeling. A summary of these improvements and developments is presented using a block digram representation (Fig. 1.1).

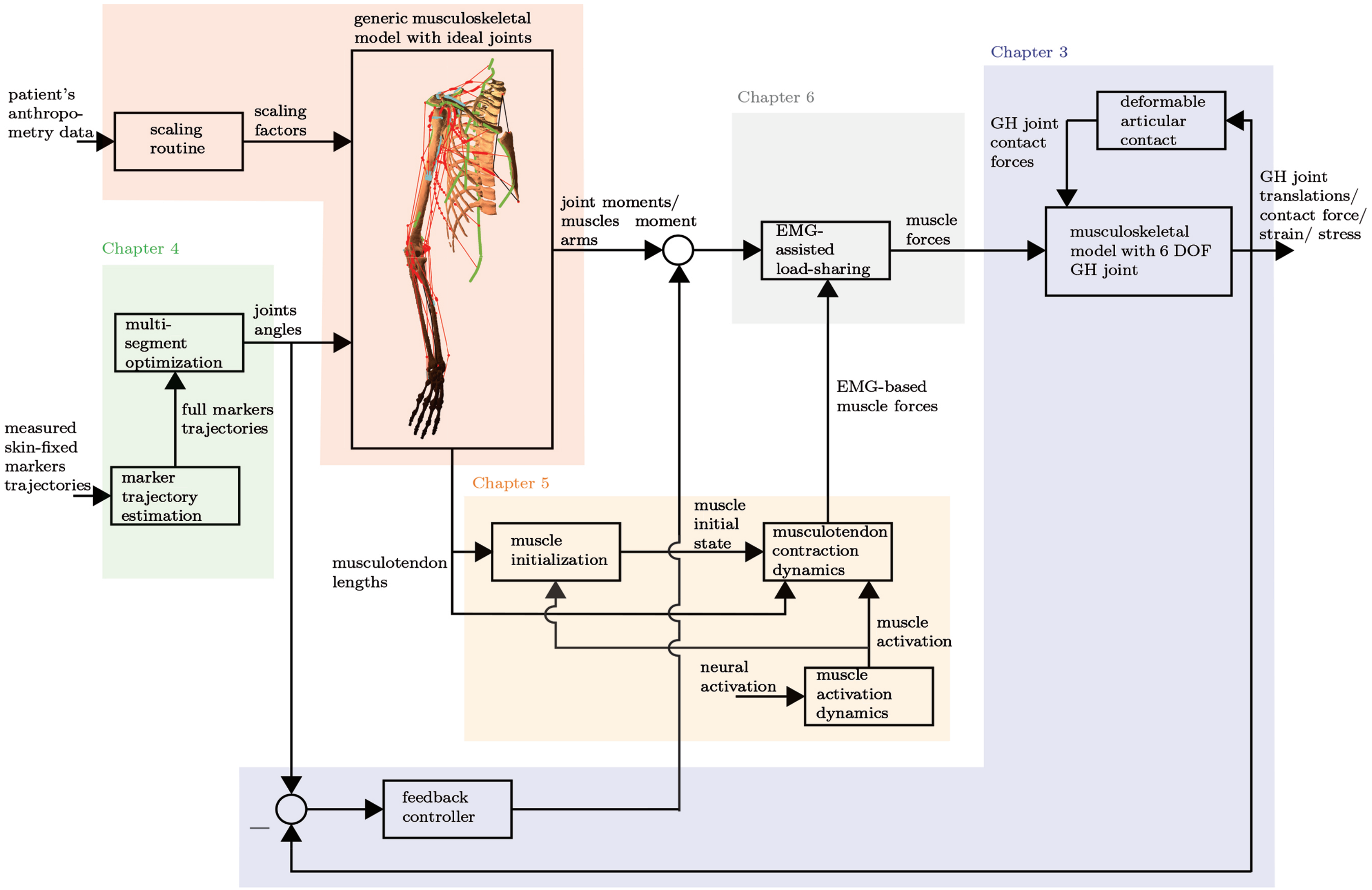

Figure 1.1: A block diagram representation of different improvements and developments considered to extend the EPFL shoulder model. They are categorized in 5 chapters. Chapter 2 deals with adding subject-specific attributes to the model and incorporating the forearm. Chapter 3 provides a framework allowing estimation of HHT and GH joint strain and stress. Chapter 4 presents a non-invasive method to estimate trajectories of glenohumeral joint center and consequently reconstruct a motion measured using skin-fixed markers. Chapter 5 explains musculotendon dynamics and details our approach in initialization of the muscle contraction dynamics. Finally, Chapter 6 exploits the subject-specific joint moments, moment arms, and EMG-based muscle forces obtained respectively from chapter 2, 4, and 5 to provide muscle forces such that co-contractions are promoted.

2 A Matlab toolbox for scaled-generic modeling of shoulder and elbow

This chapter is a preprint version of the following self-authored article that has been submitted to Journal of Source Code for Biology and Medicine.

Ehsan Sarshari, Yasmine Boulanaache, Alexandre Terrier, Alain Farron, Philippe Mullhaupt, Dominique Pioletti, “A Matlab toolbox for scaled-generic modeling of shoulder and elbow”, SCBM-D-18-00009, 2018.

Abstract

There still remains a barrier ahead of widespread clinical applications of upper extremity musculoskeletal models. This study is a step toward lifting this barrier for a shoulder musculoskeletal model by enhancing its realism and facilitating its applications. To this end, two main improvements are considered. First, the elbow and the muscle groups spanning it are included in the shoulder model. Second, scaling routines are developed that scale model's bone segment inertial properties, skeletal morphologies, and muscles architectures according to a specific subject. The model is also presented as a Matlab toolbox with a graphical user interface to exempt its users from further programming. We evaluated effects of anthropometric parameters, including subject's gender, height, weight, glenoid inclination, and degenerations of rotator cuff muscles on the glenohumeral joint reaction force (JRF) predictions. An arm abduction motion in the scapula plane is simulated while each of the parameters is independently varied. The results indeed illustrate the effect of anthropometric parameters and provide JRF predictions with less than 13% difference comparing to *in vivo* studies.

2.1 Introduction

2.1.1 Motivation

There exist several musculoskeletal models for the human upper extremity, e.g. [12–19, 46, 47]. They provide useful predictions of the joint and muscle forces that cannot be measured non-invasively [28].

In a musculoskeletal model of the upper extremity any major joints or muscles should not be neglected [4, 28]. Otherwise, its clinical applications will be limited. Some of the above-mentioned upper extremity models [12, 19] only include an outstretched arm. Therefore, the elbow and the muscle groups spanning the elbow and the shoulder (biceps and triceps) were neglected. Several studies highlighted the importance of the elbow on upper extremity kinematics and kinetics, e.g. [42, 69]. Biceps and triceps were also shown to play a crucial role in the stability of the glenohumeral joint [67, 73].

On the other hand, a vast majority of these models were developed based on anthropometric data of a single subject. Therefore, they are called generic models. Given anthropometric variabilities among subjects, they cannot predict inter-individual differences [85]. It is not yet straightforward to personalize all the anthropometric data used in a model to any subject. Obtaining these data is both time-consuming and expensive [85, 86]. Alternatively, scaling techniques are used that scale a generic model to a specific subject (scaled-generic modeling) [42, 87].

2.1.2 State-of-the-art

Given the complex multiple degrees of freedom (DOF) kinematics of the elbow, there is no consensus in the literature concerning its modeling [50, 69]. Its multiple DOF result in two distinguished movements, including extension/flexion and pronation/supination. A very simplistic cardanic joint was used to model the two movements of the elbow [74]. But, it was not realistic, given that contrary to cardanic joints, the rotation axes of the elbow are not perpendicular [75]. Other studies used two non-perpendicular hinge joints [42, 76–79]. They yet considered a single body to represent two bone segments of the forearm (ulna and radius) and neglected their interplay [80]. The sophisticated interplay of the ulna and the radius during forearm pronation/supination was studied using MRI imaging [81, 82]. More complicated elbow models were developed considering a closed-kinematic chain [79, 80, 83]. They provided detailed representations of the elbow kinematics. But, they required more individualized parameters that could not be readily obtained.

Several aspects of an upper extremity model must be scaled, in order to adapt it to a specific subject. This includes bone segments inertial properties (BSIP), skeletal morphologies, and muscles architectures [88].

Scaling BSIP: Predictive equations for BSIP were developed by investigating the BSIP of large groups of living subjects and cadavers [89–91]. They were commonly used to scale BSIP in upper extremity models [16, 42, 92]. However, they require further adjustments to accurately scale BSIP in the three dimensional (3D) space. The predictive equations of [93, 94] were adjusted by [95] to provide 3D applicable predictive equations to scale BSIP.

Scaling skeletal morphologies: This includes scaling the positions of all bony landmarks based on which a generic model is developed. Isotropic scaling factors equally scaled the skeletal morphologies of a generic model in 3D [16, 42, 97]. However, this implied an unrealistic uniform scaling between different individuals [89] and could also lead to discontinuous kinematics [97]. Anisotropic scaling factors provided more realistic scaling [98, 99]. But, they could cause non-anatomical configurations of the scapula relative to ribcage [96]. This was improved by relaxing a kinematic constraint used to force the scapula medial boarder to glide over the ribcage [98]. However, the scapula motions could be compromised. A more advanced scaling based on an optimal scaling of the ribcage was introduced in [92].

Several studies reported the effects of glenoid inclination/version on model force predictions and joint translations [64, 101, 193, 200]. However, the available models do not allow adapting them to an understudy subject.

Scaling muscles architectures: This includes scaling muscle origins/insertions, wrapping objects, and musculotendon parameters such as physiological cross section areas

(PCSA) [103].

Muscle origins/insertion: Three different approaches were used to scale muscles origins/insertions, namely linear bone mapping [104, 105], anisotropic bone morphing [106–108], and statistical bone morphing [109, 110]. A linear bone mapping was defined using the positions of few bony landmarks on a specific subject [104, 105]. The resulting mapping was used to approximate the muscle origins/insertions by rotating their corresponding origins/insertions from a generic model. This was considerably improved by considering not only rotations but also displacements and bone deformations in anisotropic bone morphing methods [106–108]. But, they required complete bone morphologies of each subject that could be obtained only by expensive imaging techniques. Statistical bone morphing methods were developed by investigating statistical shape variations of bones [109, 110]. They also required at least part of the bone morphologies from each subject.

Muscle wrapping objects: The paths taken by muscles are not always a straight line from their origins to their insertions. They instead wrap around their underlying bones and soft tissues that are approximated by wrapping objects. Scaling the wrapping objects was not addressed at least explicitly in the literature. However, they can considerably alter muscle moment arms and model force predictions [111, 112].

Musculotendon parameters: PCSA was scaled by comparing the total muscle bulk of a subject to that of a generic model [113, 114]. However, an MRI scan was required that might affect the practical use of this method. The body mass index (BMI) [115] was also used to scale PCSA [42]. But, direct association of the BMI to PCSA was arguable [116]. A predictive equation based on the BMI was introduced in [117] that defined muscle percentage of the body composition. Scaling of other musculotendon parameters such as tendon length were addressed by using isotropic scaling factors [118].

2.1.3 Research method

Therefore, the aim of this study is to develop a scaled-generic musculoskeletal model of the shoulder and the elbow. The model is used to evaluate the effects of subject's gender, height, weight, glenoid inclination, and rotator cuff (RC) PCSAs on the JRF. To this end, the elbow is included into our previously developed shoulder model [19]. Scaling routines are developed to scale model's BSIP, skeletal morphologies, and muscles architectures according to a subject's gender, height, weight. It also allows adapting the model's glenoid inclination/version. An abduction motion in the scapula plane is simulated. The results are presented in terms of the JRF predictions along the arm abduction angle. Also, the model is developed as a Matlab toolbox with a graphical user interface (GUI) to facilitate its clinical applications.

2.2 Methods

A kinematic model of the elbow is developed (Section 2.2.1). Build on the resulting kinematic model, a dynamic model of the elbow is derived (Section 2.2.2). The dynamic model of the elbow together with fourteen muscles spanning the elbow are integrated into the shoulder model (Section 2.2.3). Our approaches in scaling the developed shoulder and elbow model are detailed (Section 2.2.4). The shoulder and elbow Matlab toolbox is also introduced (Section 2.2.5). Finally, a parameter study is performed to evaluate the model (Section 2.2.6).

2.2.1 Elbow kinematics

The kinematic development of our shoulder model including the thorax, the clavicle, the scapula, and an outstretched arm has been described in [19, 100]. It was developed from MRI scans of the right shoulder of a healthy male subject (29 years, 186 cm, and 85.5 kg). It had seven DOF attributing to three ball-and-socket joints and two holonomic constraints. The joints were associated to the sternoclavicular, the acromioclavicular, and the glenohumeral (GH) joints. The constraints were considered for restricting the scapula to always glide on the ribcage. Here we focus on extending the kinematic model to incorporate the elbow.

Surface boundaries of the forearm bones are obtained from MRI scans of the same subject (Fig. 2.1a). The ulna and the radius are considered as two segments. The hand is assumed to be rigidly tied to the radius by neglecting the carpal joint. Two DOFs are considered attributing to two non-perpendicular hinge joints. The two hinge joints replicate the kinematics of four anatomical joints, including the humeroulnar, the radioulnar proximal/distal, and the humeroradial joints. They allow simulating forearm flexion/extension and pronation/supination. Three non-collinear bony landmarks are required to uniquely define the spatial configuration of each bone segment in the 3D space [11]. Only one landmark can be discerned on each one of the ulna and the radius, i.e. the ulnar styloid process (US) and the radial styloid process (RS), respectively (Fig. 2.1b). Therefore, three bony landmarks on the humerus are borrowed, including the lateral epicondyle (EL) and the medial epicondyle (EM) and their middle point (HU). Two bone-fixed frames are defined for the ulna and the radius using these landmarks as follows:

- Ulna bone-fixed frame: $\{\boldsymbol{O}_u, \hat{x}_u, \hat{y}_u, \hat{z}_u\}$

$$\begin{aligned}
&\boldsymbol{O}_u \equiv {}_t\boldsymbol{HU} \\
&\hat{x}_u = {}_t\boldsymbol{EL} - {}_t\boldsymbol{HU} \implies \hat{x}_u = {}^{\hat{x}_u}\!/\!_{|\hat{x}_u|} \\
&\hat{y}_u = ({}_t\boldsymbol{US} - {}_t\boldsymbol{EL}) \times ({}_t\boldsymbol{EM} - {}_t\boldsymbol{EL}), \implies \hat{y}_u = {}^{\hat{y}_u}\!/\!_{|\hat{y}_u|} \\
&\hat{z}_u = \hat{x}_u \times \hat{y}_u \\
&{}^{t}_{u}R = [\hat{x}_u \ \hat{y}_u \ \hat{z}_u]
\end{aligned} \tag{2.1}$$

- Radius bone-fixed frame: $\{\boldsymbol{O}_r, \hat{x}_r, \hat{y}_r, \hat{z}_r\}$

$$\begin{aligned}
&\boldsymbol{O}_r \equiv {}_t\boldsymbol{EL} \\
&\hat{z}_r = {}_t\boldsymbol{EL} - {}_t\boldsymbol{US} \implies \hat{z}_r = {}^{\hat{z}_r}\!/\!_{|\hat{z}_r|} \\
&\hat{y}_r = ({}_t\boldsymbol{EL} - {}_t\boldsymbol{RS}) \times ({}_t\boldsymbol{RS} - {}_t\boldsymbol{US}), \implies \hat{y}_r = {}^{\hat{y}_r}\!/\!_{|\hat{y}_r|} \\
&\hat{x}_r = \hat{y}_r \times \hat{z}_r \\
&{}^{t}_{r}R = [\hat{x}_r \ \hat{y}_r \ \hat{z}_r]
\end{aligned} \tag{2.2}$$

Where, the symbol × denotes the cross product of vectors, and $\boldsymbol{O}_u$ and $\boldsymbol{O}_r$ are the origins of the ulna and the radius frames, respectively. The left hand side subscript t specifies that the landmarks are expressed in the thorax (inertial) frame, and ${}^{t}_{u}R$ and ${}^{t}_{r}R$ are also the rotation matrices from the ulna and the radius frames to the thorax frame, respectively.

The joint coordinates are considered to be aligned with the bone-fixed frames (Fig. 2.1b). Two generalized coordinates (q_{10} and q_{11}) are used to uniquely define each joint configuration. More specifically, q_{10} and q_{11} represent the elbow flexion/extension and pronation/supination, respectively. The rotation matrices in terms of the generalized coordinates can be obtained as Eq. 2.3.

$$\begin{aligned}
&{}^{t}_{u}R = {}^{t}_{h}R \ {}^{h}_{u}R_f \ R_{\hat{x}_u}(q_{10}) \\
&{}^{t}_{r}R = {}^{t}_{u}R \ {}^{u}_{r}R_f \ R_{\hat{z}_r}(q_{11})
\end{aligned} \tag{2.3}$$

Where, ${}^{t}_{h}R$ is the rotation matrix from the humerus frame to thorax frame. The rotation matrices ${}^{h}_{u}R_f$ and ${}^{u}_{r}R_f$ are used to align the ulna and the radius frames to their proximal bone frames. Once they are defined for any configuration of the ulna and the radius, they remain unchanged. They are obtained as ${}^{h}_{u}R_f = {}^{t}_{h}R_f{}^{T}\,{}^{t}_{u}R_f$ and ${}^{u}_{r}R_f = {}^{t}_{u}R_f{}^{T}\,{}^{t}_{r}R_f$, where the right-hand side rotation matrices are defined using Eq. 2.1 and Eq. 2.2 for an arbitrary configuration of the shoulder and the elbow. The rotation matrices for

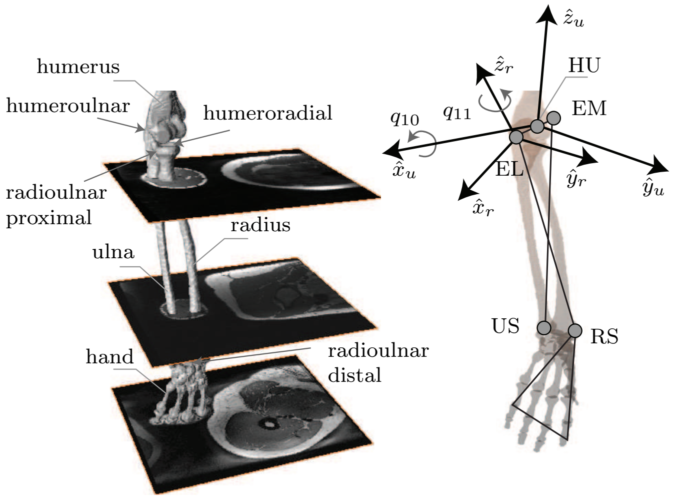

(a) (b)

Figure 2.1: Modeling the elbow kinematics. (a) MRI scans of the forearm from the same subject are used to define the surface boundaries of the ulna and the radius. The hand is assumed to be rigidly tied to the radius. The elbow consists of 4 anatomical joints including humeroulnar, radioulnar proximal/distal, and humeroradial joints. (b) Two non-perpendicular hinge joints are considered to replicate the elbow motion. To construct the bone-fixed frames, 3 landmarks namely EM, HU, and EL are borrowed from the humerus. Two landmarks namely US and RS are also used from ulna and radius, respectively. $\{\boldsymbol{HU}, \hat{x}_u, \hat{y}_u, \hat{z}_u\}$ and $\{\boldsymbol{EL}, \hat{x}_r, \hat{y}_r, \hat{z}_r\}$ are the ulna and the radius frames, respectively. The joint coordinates are considered to be coincide with the bone-fixed frames. Two generalized coordinate q_{10} and q_{11} are used to uniquely define elbow flexion/extension and pronation/supination, respectively.

flexion/extension and pronation/supination ($R_{\hat{x}_u}$ and $R_{\hat{z}_r}$) are defined in Eq. 2.4.

$$\begin{aligned} R_{\hat{x}_u} &= \begin{bmatrix} 1 & 0 & 0 \\ 0 & \cos q_{10} & -\sin q_{10} \\ 0 & \sin q_{10} & \cos q_{10} \end{bmatrix} \\ R_{\hat{z}_r} &= \begin{bmatrix} \cos q_{11} & -\sin q_{11} & 0 \\ \sin q_{11} & \cos q_{11} & 0 \\ 0 & 0 & 1 \end{bmatrix} \end{aligned} \tag{2.4}$$

It is worth mentioning that, introduction of ${}^{h}_{u}R_f$ and ${}^{u}_{r}R_f$ deviates from the ISB recommendations [201]. Because, the ISB requires inherent alignment of the ulna and the radius frames relative to their proximal bones. The inherent alignment however results in non-physiological configurations of the forearm relative to humerus [202].

The following forward kinematics map (ξ_{elbow}) is obtained using equations 2.1 to 2.4. It defines ${}_{t}\boldsymbol{US}$ and ${}_{t}\boldsymbol{RS}$ for given q_{10}, q_{11}, ${}_{t}\boldsymbol{EL}$, and ${}_{t}\boldsymbol{EM}$ (Eq. 2.5). It is incorporated in the previously developed forward kinematic map of the shoulder model to provide a complete representation of the upper extremity kinematics.

$$\begin{aligned} &\xi_{\text{elbow}} : C_s \subset R^2 \mapsto W_s \subset R^3 \\ &\xi_{\text{elbow}}(q_{10}(t),\ q_{11}(t)) = \boldsymbol{x}_j(t), \quad j = \{\text{US},\ \text{RS}\} \end{aligned} \tag{2.5}$$

Where, C_s and W_s denote the elbow's coordinate and work spaces [11], and $\boldsymbol{x}_{\text{US}}(t) \equiv {}_t\boldsymbol{US}$, and $\boldsymbol{x}_{\text{RS}}(t) \equiv {}_t\boldsymbol{RS}$.

2.2.2 Elbow dynamics

Mass and inertial properties are attributed to the ulna and the radius according to [14]. The mass and inertia of the hand are also added to radius using parallel axis theorem [11]. The centers of mass ($\boldsymbol{CG}$) of the ulna and the radius are defined as

$$\begin{aligned} \boldsymbol{CG}_u &= \tfrac{1}{2}\ {}^t_u R\ {}_u\boldsymbol{US} + {}_t\boldsymbol{HU} \\ \boldsymbol{CG}_r &= \tfrac{1}{2}\ {}^t_r R\ {}_r\boldsymbol{RS} + {}_t\boldsymbol{EL} \end{aligned} \tag{2.6}$$

Where, the left-hand side subscripts u and r specify that the landmarks are expressed in the ulna and the radius frames, respectively.

The angular velocities of the ulna ($\boldsymbol{\omega}_u$) and the radius ($\boldsymbol{\omega}_r$) in their bone-fixed frames are given by

$$\begin{aligned} \boldsymbol{\omega}_u &= R^T_{\hat{x}_u}\ {}^h_u R^T_f\ \boldsymbol{\omega}_h + [\dot{q}_{10}\ 0\ 0]^T \\ \boldsymbol{\omega}_r &= R^T_{\hat{z}_r}\ {}^u_r R^T_f\ \boldsymbol{\omega}_u\ + [0\ 0\ \dot{q}_{11}]^T \end{aligned} \tag{2.7}$$

Where $\boldsymbol{\omega}_h$ is the humerus angular velocity.

The Lagrangians of the ulna ($\mathcal{L}_u$) and the radius ($\mathcal{L}_r$) are defined in terms of their kinetic and potential energies (Eq. 2.8).

$$\begin{aligned} \mathcal{L}_u &= \tfrac{1}{2}(m_u \dot{\boldsymbol{CG}}_u^T \dot{\boldsymbol{CG}}_u + \boldsymbol{\omega}_u^T I_u \boldsymbol{\omega}_u) - m_u g[0\ 0\ 1]\boldsymbol{CG}_u \\ \mathcal{L}_r &= \tfrac{1}{2}(m_r \dot{\boldsymbol{CG}}_r^T \dot{\boldsymbol{CG}}_r + \boldsymbol{\omega}_r^T I_r \boldsymbol{\omega}_r)\ - m_r g[0\ 0\ 1]\boldsymbol{CG}_r \end{aligned} \tag{2.8}$$

Where m_u and m_r are the mass, and I_u and I_r are the inertias of the ulna and the radius in their bone-fixed frames, respectively.

2.2.3 Integration of the elbow model into the shoulder model

The Lagrangians $\mathcal{L}_u$ and $\mathcal{L}_r$ are added to the Lagrangian of the shoulder model (Eq. 2.9). It includes the Lagrangians of the clavicle ($\mathcal{L}_c$), the scapula ($\mathcal{L}_s$), and the humerus ($\mathcal{L}_h$).

$$\mathcal{L} = \mathcal{L}_c + \mathcal{L}_s + \mathcal{L}_h + \mathcal{L}_u + \mathcal{L}_r \tag{2.9}$$

Where $\mathcal{L}$ is the augmented Lagrangian of the shoulder and elbow model.

Two constraints are also used in the shoulder kinematic model. They force trigonum scapulae (TS) and angulus acromialis (AI) points on the scapula medial boarder to always lie on two ellipsoids. The ellipsoids approximate the ribcage and the underlying soft tissues of each one of TS and AI. The constraints are written as

$$\begin{aligned} \Phi_{\mathrm{TS}}(\boldsymbol{q}(t)) &= ({}_t\boldsymbol{TS}(t) - \boldsymbol{e}_0)^T E_{\mathrm{TS}}({}_t\boldsymbol{TS}(t) - \boldsymbol{e}_0) - 1 = 0 \\ \Phi_{\mathrm{AI}}(\boldsymbol{q}(t)) &= ({}_t\boldsymbol{AI}(t) - \boldsymbol{e}_0)^T E_{\mathrm{AI}}({}_t\boldsymbol{AI}(t) - \boldsymbol{e}_0) - 1 = 0 \end{aligned} \tag{2.10}$$

Where, $\boldsymbol{e}_0$ is the center of the ellipsoids in the thorax frame, and E_{TS} and E_{AI} are the matrices corresponding to each of the ellipsoids.

The equations of motion are obtained using the Lagrange's equations (Eq. 2.11).

$$\frac{d}{dt}\left(\frac{\partial \mathcal{L}}{\partial \dot{\boldsymbol{q}}}\right) - \frac{\partial \mathcal{L}}{\partial \boldsymbol{q}} = \frac{\partial \Omega}{\partial \dot{\boldsymbol{q}}} M + \lambda_{\mathrm{TS}} \frac{\Phi_{\mathrm{TS}}}{\partial \boldsymbol{q}} + \lambda_{\mathrm{AI}} \frac{\Phi_{\mathrm{AI}}}{\partial \boldsymbol{q}} \tag{2.11}$$

Where, $\boldsymbol{q}$ is the generalized coordinate vector of the shoulder and elbow model, and Ω is a horizontal matrix consisting of the angular velocities of all the 5 bone segments. The vertical matrix M includes the muscle resultant moments around each one of the 5 joints. The first term on the right-hand side is the generalized force vector defined as the multiplication of the partial angular velocity matrix ($\frac{\partial \Omega}{\partial \dot{\boldsymbol{q}}}$) and M. The resultant moment matrix M can be expressed as $M = W\boldsymbol{f}$, where W is the moment arm matrix and $\boldsymbol{f}$ is a vector including the magnitudes of all the muscle forces. The Lagrange multipliers λ_{TS} and λ_{AI} are proportional to the magnitudes of the forces applied on the scapula due to the ribcage constraints. The jacobians of the constraints ($\frac{\Phi_{\mathrm{TS}}}{\partial \boldsymbol{q}}$ and $\frac{\Phi_{\mathrm{AI}}}{\partial \boldsymbol{q}}$) define the generalized moment arms of the constraints.

The moment arm matrix W can be obtained using its well-known geometric definition or the tendon excursion method [112]. In either ways, the paths taken by the muscles approximated as massless elastic strings are required. To this end, the obstacle set

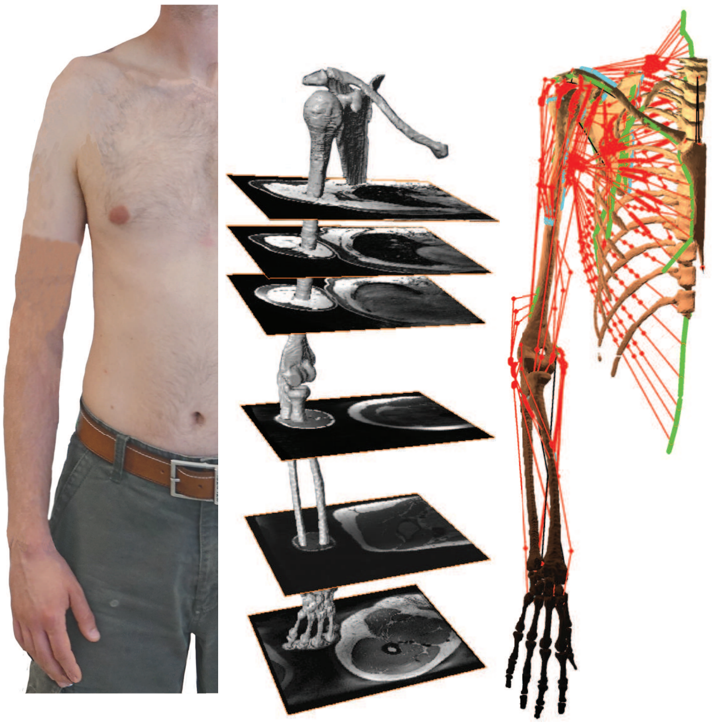
(a) (b) (c)

Figure 2.2: The developed shoulder and elbow model. (a) The anthropometric data of a healthy male subject is used to develop the model. (b) The bone morphologies and muscles origins/insertions are deduced from MRI scans of the same subject. (c) The model consists of thorax, clavicle, scapula, humerus, ulna, radius, and a hand tied to the radius. It has nine DOF represented by eleven generalized coordinates and two holonomic constraints. The model includes 42 muscles that can be represented by up to 20 massless elastic strings. Muscle origins and insertions are denoted by green and blue areas, respectively.

method is used [111]. The origins/insertions and the associated via points of 14 muscles spanning the elbow are defined based on the MRI scans and the help of a professional radiologist. Their associated wrapping objects are set by modifying recommendations of [14] for the type, center, axis, and radius of the objects to best fit the MRI scans. They include triceps brachii long/medial/lateral, biceps brachii short/long, brachialis, brachioradialis, supinator, pronator Teres, flexor carpi radialis/ulnaris, and extensor carpi radiali long/radialis bervis/ulnaris. Therefore, the shoulder and elbow model consists of 42 muscle groups that each one of them can be represented by up to 20 strings (Fig. 2.2).

The equations of motion (Eq. 2.11) are solved for unknown muscle forces $\boldsymbol{f}$ using inverse dynamics for a given $\boldsymbol{q}$. The shoulder and elbow model is over-actuated, i.e. there are more muscles (42 times the number of strings used for each muscle) than the number of equations (11 equations, one per generalized coordinate). Therefore, the following so-called standard load-sharing is casted to solve the over-actuation problem using static optimization [52].

$$\begin{aligned} \min_{\tilde{\boldsymbol{f}}} \quad & \tilde{\boldsymbol{f}}^T P \tilde{\boldsymbol{f}} \\ \text{s.t.} \quad & \frac{d}{dt}\left(\frac{\partial \mathcal{L}}{\partial \dot{\boldsymbol{q}}}\right) - \frac{\partial \mathcal{L}}{\partial \boldsymbol{q}} = \left[\frac{\partial \Omega}{\partial \dot{\boldsymbol{q}}} W \;\; \frac{\Phi_{\text{TS}}}{\partial \boldsymbol{q}} \;\; \frac{\Phi_{\text{AI}}}{\partial \boldsymbol{q}}\right] \tilde{\boldsymbol{f}} \\ & \mathbf{0} \le \tilde{\boldsymbol{f}} \le \tilde{\boldsymbol{f}}_{\max} \\ & \boldsymbol{\psi}(\boldsymbol{q},\ \dot{\boldsymbol{q}},\ \ddot{\boldsymbol{q}}, \tilde{\boldsymbol{f}}) \le \mathbf{0} \end{aligned} \tag{2.12}$$

Where, $\tilde{\boldsymbol{f}} \equiv [\boldsymbol{f}^T \ \lambda_{\text{TS}} \ \lambda_{\text{AI}}]^T$, and P is a diagonal matrix including the inverse squared of muscles PCSAs. The numerical values for PCSAs are set according to [203]. The constraint $\boldsymbol{\psi}$ forces the JRF to always point toward inside of a cone that replicates the glenoid fossa. It is commonly called the GH joint stability constraint. The optimization is a quadratic programming problem that can be solved using `quadprog` of Matlab. It defines $\tilde{\boldsymbol{f}}$ such that the sum of squared muscle stresses are minimized, while the constraints are satisfied.

2.2.4 Model scaling

Scaling BSIP: The model BSIP are scaled based on the subject's gender, weight (m_B), and height (l_H) using the 3D predictive equations of [95]. More specifically, the mass and the length of each bone segment is defined as portions of m_B and l_H, respectively (Table 2.1). The portions slightly vary for male and female subjects. The resulting bone segment masses and lengths are used to define their inertias in the transverse and the lateral directions of the bone-fixed frames.

Scaling skeletal morphologies: The skeletal morphologies are scaled using an anisotropic scaling matrix S. It is defined according to l_H and the subject's shoulder width l_W (Eq. 2.13). The l_W is defined as the distance between the two angulus acromialis landmarks on the left and the right shoulder.

$$S = \begin{bmatrix} \frac{l_W}{l_{W_g}} & 0 & 0 \\ 0 & \frac{l_W}{l_{W_g}} & 0 \\ 0 & 0 & \frac{l_H}{l_{H_g}} \end{bmatrix} \tag{2.13}$$

Where, l_{H_g} and l_{W_g} are the height and shoulder width of the generic model.

The two ribcage ellipsoids are scaled by dilating a base ellipsoid. The base ellipsoid is obtained during the construction of the generic model by fitting it to the ribcage. It is

Table 2.1: Scaling BSIP based on subject's gender, weight (m_B), and height (l_H) using the 3D predictive equations of [95]. Clavicle, scapula, humerus, ulna, and radius masses are denoted by m_c, m_s, m_h, m_u, and m_r, respectively. The segments lengths of humerus, ulna, and radius are l_h, l_u, and l_r. Their inertias in transverse and lateral directions of their bone-fixed frames are denoted by I_{h_t}, I_{u_t}, I_{r_t}, I_{h_l}, I_{u_l}, and I_{r_l}, respectively. The m_u and m_r are defined as 62% and 38% of the forearm weight. The m_B and l_H are expressed in centigram and centimeter, respectively.

	BSIP	male	female
clavicle	m_c	$0.18m_B$	$0.18m_B$
scapula	m_s	$0.82m_B$	$0.82m_B$
humerus	m_h	$2.4m_B$	$2.2m_B$
	l_h	$\frac{27}{177}l_H$	$\frac{24.3}{161}l_H$
	I_{h_t}	$(0.315l_h)^2m_h$	$(0.33l_h)^2m_h$
	I_{h_l}	$(0.14l_h)^2m_h$	$(0.17l_h)^2m_h$
ulna	m_u	$(0.62)(1.7)m_B$	$(0.62)(1.3)m_B$
	l_u	$\frac{28.3}{177}l_H$	$\frac{24.7}{161}l_H$
	I_{u_t}	$(0.275l_u)^2m_u$	$(0.255l_u)^2m_u$
	I_{u_l}	$(0.11l_u)^2m_u$	$(0.14l_u)^2m_u$
radius	m_r	$(0.38)(1.7)m_B$	$(0.38)(1.3)m_B$
	l_r	$\frac{28.3}{177}l_H$	$\frac{24.7}{161}l_H$
	I_{r_t}	$(0.275l_r)^2m_r$	$(0.255l_r)^2m_r$
	I_{r_l}	$(0.11l_r)^2m_r$	$(0.14l_r)^2m_r$

centered at $\boldsymbol{e}_0$ with axes equal to e_{BE_x}, e_{BE_y}, and e_{BE_z}. The centers of the two dilated ellipsoids are obtained by scaling $\boldsymbol{e}_0$ with S. Then, their axes are obtained by an isotropic dilation of the base ellipsoid so that they include their associated scaled landmark TS or AI. The dilation factors (δ_{TS} and δ_{AI}) are calculated by using the scaled TS and AI in the equations of their respective ellipsoids and solving the resulting 6th degree polynomial equations for δ_{TS} and δ_{AI} (Eq. 2.14).

$$
\begin{gathered}
(S_t\boldsymbol{TS} - S\boldsymbol{e}_0)^T \begin{bmatrix} \frac{1}{(e_{\mathrm{BE}_x}+\delta_{\mathrm{TS}})^2} & 0 & 0 \\ 0 & \frac{1}{(e_{\mathrm{BE}_y}+\delta_{\mathrm{TS}})^2} & 0 \\ 0 & 0 & \frac{1}{(e_{\mathrm{BE}_z}+\delta_{\mathrm{TS}})^2} \end{bmatrix} (S_t\boldsymbol{TS} - S\boldsymbol{e}_0) - 1 = 0 \\
(S_t\boldsymbol{AI} - S\boldsymbol{e}_0)^T \begin{bmatrix} \frac{1}{(e_{\mathrm{BE}_x}+\ \delta_{\mathrm{AI}})^2} & 0 & 0 \\ 0 & \frac{1}{(e_{\mathrm{BE}_y}+\ \delta_{\mathrm{AI}})^2} & 0 \\ 0 & 0 & \frac{1}{(e_{\mathrm{BE}_z}+\delta_{\mathrm{AI}})^2} \end{bmatrix} (S_t\boldsymbol{AI} - S\boldsymbol{e}_0) - 1 = 0
\end{gathered}
\tag{2.14}
$$

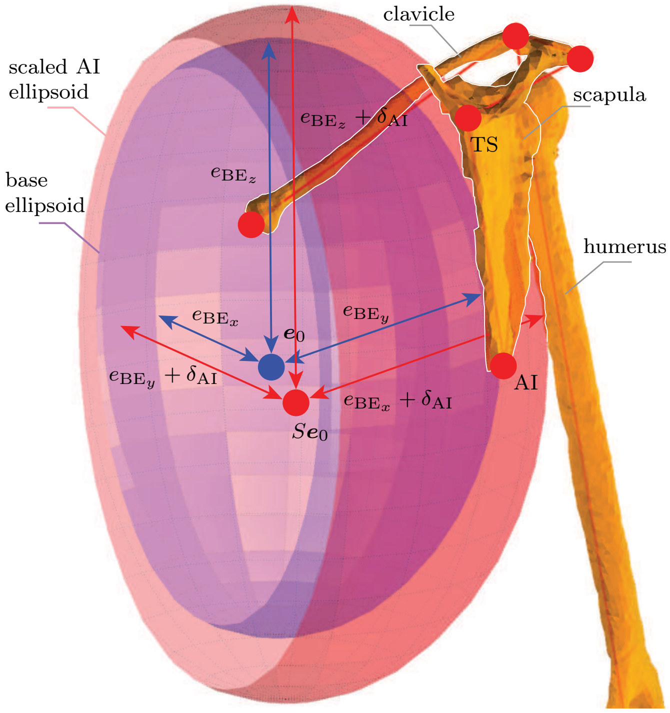

Figure 2.3: Scaling the ribcage ellipsoid containing AI. A base ellipsoid (blue) is dilated by δ_{AI} to obtain the ribcage ellipsoid AI (red). The base ellipsoid is centered at $\boldsymbol{e}_0$ with axes equal to e_{BE_x}, e_{BE_y}, and e_{BE_z}. The center of the scaled AI ellipsoid is also obtained by scaling $\boldsymbol{e}_0$ with S. Scaling the TS ribcage ellipsoid follows the same procedure and results in an ellipsoid centered at $S\boldsymbol{e}_0$ and dilated by δ_{TS}.

Eq. 2.14 is solved numerically for instance using `roots` of Matlab. It has only two positive roots that are considered as δ_{TS} and δ_{AI} (Fig. 2.3).

In a case where videogrammetry measurement data are available for a subject, the scaling matrix S is defined for each bone segment. The landmarks on each bone segment are used to define its length. The resulting length is used to define a scaling factor by comparing it to an associated length from the generic model. The scaling of the ribcage ellipsoids follows the same approach as Eq. 2.14, except that the measured positions of TS and AI are used instead of their scaled positions.

The glenoid inclination(α_{GI}) and version (α_{GV}) are determined according to a definition provided in [64, 200]. A bone-fixed frame attached to the spino-glenoid notch (SN) defines scapula configurations (Eq. 2.15 and Fig. 2.4).

- Scapula bone-fixed frame: $\{\boldsymbol{O}_s, \hat{x}_s, \hat{y}_s, \hat{z}_s\}$

$$\begin{aligned}
&\boldsymbol{O}_s \equiv {}_t\boldsymbol{SN} \\
&\hat{x}_u = \hat{y}_s \times \hat{z}_s \\
&\hat{y}_s = ({}_t\boldsymbol{SN} - {}_t\boldsymbol{AI}) \times ({}_t\boldsymbol{SN} - {}_t\boldsymbol{TS}) \implies \hat{y}_s = \hat{y}_s/|\hat{y}_s| \\
&\hat{z}_s = ({}_t\boldsymbol{SN} - {}_t\boldsymbol{TS}) \times \hat{y}_s, \implies \hat{z}_s = \hat{z}_s/|\hat{z}_s| \\
&{}^t_sR = [\hat{x}_s \ \hat{y}_s \ \hat{z}_s]
\end{aligned} \tag{2.15}$$

The α_{GI} is the angle between the $\hat{z}_s$ and a vector connecting the inferior glenoid (IG) and the superior glenoid (SG) points projected on $\hat{x}_s\hat{z}_s$ plane. The α_{GV} is the angle between the $\hat{y}_s$ and a vector connecting the posterior glenoid (PG) and the anterior glenoid (AG) points projected on $\hat{x}_s\hat{y}_s$ plane. Provided subject specific values for α_{GI} and α_{GV}, their associated angles can be adapted in the generic model. To this end, first $\Delta\alpha_{\mathrm{GI}} = \alpha_{\mathrm{GI}} - \alpha_{\mathrm{GI}_g}$ and $\Delta\alpha_{\mathrm{GV}} = \alpha_{\mathrm{GV}} - \alpha_{\mathrm{GV}_g}$ are defined, where subindex g denotes the values of the generic model. The rotation operators R_{GI} and R_{GV} are used according to Eq. 2.16 to rotate the glenoid center (GC) around $\hat{y}_s$ and $\hat{z}_s$ by $\Delta\alpha_{\mathrm{GI}}$ and $\Delta\alpha_{\mathrm{GV}}$, respectively. The resulting GC is used to construct a cone frame that defines the GH joint stability constraint (Eq. 2.12).

$$\begin{aligned}
R_{\mathrm{GI}} &= \hat{y}_s\hat{y}_s^T + \cos\Delta\alpha_{\mathrm{GI}}(I - \hat{y}_s\hat{y}_s^T) + \sin\Delta\alpha_{\mathrm{GI}}[\hat{y}_s] \\
R_{\mathrm{GV}} &= \hat{z}_s\hat{z}_s^T + \cos\Delta\alpha_{\mathrm{GV}}(I - \hat{z}_s\hat{z}_s^T) + \sin\Delta\alpha_{\mathrm{GV}}[\hat{z}_s]
\end{aligned} \tag{2.16}$$

Where, the cross product matrices corresponding to $\hat{y}_s$ and $\hat{z}_s$ are denoted by $[\hat{y}_s]$ and $[\hat{z}_s]$, respectively.

Scaling muscles architectures: The muscles insertion/origins, via points, and wrapping objects' radii and centers are all scaled using the matrix S.

The muscle PCSAs are scaled based on the subject's gender and body muscle-percentage (r_m). Predictive equations [117] are used that provide an estimation of r_m based on subject's BMI defined as BMI $\equiv \frac{m}{l^2}$ (Eq. 2.17). The ratio of the subject's r_m to that of the generic model is used to scale PCSAs. Furthermore, the model allows neglecting the scaled PCSAs in case subject specific values are provided.

$$r_m = \begin{cases} 1.09 - 0.0149\mathrm{BMI} + 0.00009\mathrm{BMI}^2 & \text{male} \\ 1.08 - 0.0203\mathrm{BMI} + 0.000156\mathrm{BMI}^2 & \text{female} \end{cases} \tag{2.17}$$

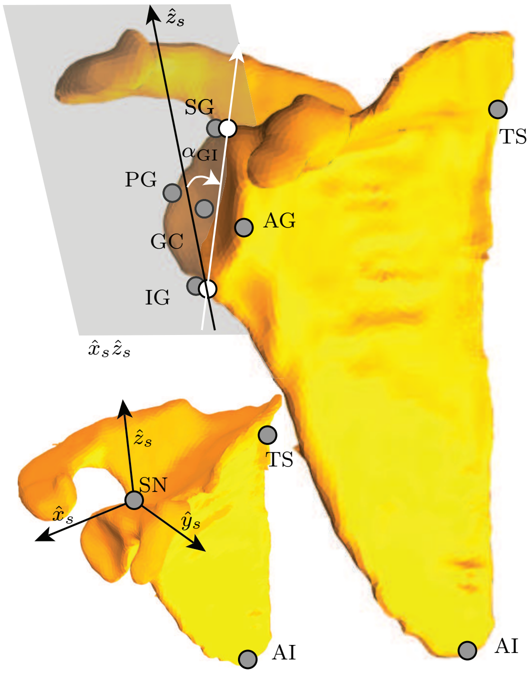

Figure 2.4: Scaling and definition of the glenoid inclination/version (α_{GI} and α_{GV}). The scapula frame $\{\hat{x}_s\ \hat{y}_s\ \hat{z}_s\}$ is attached to SN and is defined according to Eq. 2.15. The α_{GI} is defined in $\hat{x}_s\hat{z}_s$ plane where the two points IG and SG are projected (white circles). It is defined as the angle between the $\hat{z}_s$ and a vector passes through the two projected points of IG and SG. The α_{GV} has a similar definition, but in the $\hat{x}_s\hat{y}_s$ plane and through projections of PG and AG. The adaptation of α_{GI} and α_{GV} results in a scaled GC point that modifies the cone of the stability constraint (Eq. 2.12).

2.2.5 Shoulder and elbow Matlab toolbox

The developed shoulder and elbow model provides predictions of muscles and joints reaction forces for a measured motion. It is developed on open-source principles in Matlab. It has a graphical user interface (GUI) that facilitates its applications. It has 5 main sub-tool windows that are briefly described below (Fig. 2.6).

1. Subject specific tool

   It allows scaling or adapting the BSIP, skeletal morphologies, and muscles architectures of the generic model using subject's gender, height, shoulder width, and weight. The scaled model can be compared visually to the generic model (Fig. 2.7).

2. Muscle wrapping tool

   It allows visual verifications of the muscles paths during different joint configurations. The muscles insertions/origins, wrapping objects' centers and radii, and via points can be verified (Fig. 2.8).

3. Kinematics tool

   It allows reconstructing a motion of the upper extremity with or without videogrammetry measurement data (Fig. 2.9). Its first sub-tool window calculate joints angles evolutions in the lack of measurement data for a desired initial and final configuration of the upper extremity [100]. The second sub-tool can construct a measured motion using multi-segment optimization method and provide joints angles evolutions.

4. Moment arms tool

   For the joint angles evolutions obtained from the kinematics tool, it provides muscles moment arms (Fig. 2.11). The muscles moment arms are calculated using both the geometrical and the tendon excursion methods and can be compared.

5. Force prediction tool

   It provides predictions of muscles forces and JRF using inverse-dynamics and optimal load-sharing (Fig. 2.12). It also allows inclusion of electromyography (EMG) data and force predictions with or without the GH joint stability constraint.

2.2.6 Parameter study

Subject's gender, height, weight, glenoid inclination, and PCSAs of RC muscles are independently varied to evaluate their effects on the JRF predictions. Two variations are considered for the height, 1.60 m and 1.95 m. The weight variations are 60 kg and 100 kg. The glenoid inclination is varied from its generic value of 7^{o} to -7^{o} and 15^{o}, according to the variations observed in healthy subjects [204]. The PCSAs of RC muscles are reduced by 50% [205]. The resulting PCSAs are 10.42 cm^2, 16.66 cm^2, 17.84 cm^2, and 3.40 cm^2 for supraspinatus (Ss), infraspinatus (Is), subscapularis (Sc), and teres minor (Tm), respectively. The generic model is scaled for each one of the variations. An abduction motion in the scapula plane is simulated using the kinematics tool of the developed toolbox. The results are presented in terms of the JRF predictions along the arm abduction angle.

2.3 Results

The change of subject's gender to female resulted in an almost -95 N shift in the JRF with respect to the male subject of the generic model (Fig. 2.5a). The JRF predictions for the male generic model increased from 276 N at 20^{o} abduction to 585 N (69.80 % body weight) at 122^{o} abduction and decreased afterward.

The reduction of subject's weight to 60 kg considerably reduced (almost 30%) the maximum predicted JRF comparing to the generic model (Fig. 2.5b). The JRF increased to 684 N (almost 17%) due to increase in the subject's weight to 100 kg.

The variations of subject's height had almost zero effect on the JRF predictions (Fig. 2.5c).

The variations of the α_{GI} had negligible effects on the peak of JRF predictions (Fig. 2.5d). However, its reduction to -7° resulted in almost 10% less JRF until 60° abduction. The JRF reduction continued again after 125° abduction for $\alpha_{\mathrm{GI}} = -7^{\mathrm{o}}$. For $\alpha_{\mathrm{GI}} = 15^{\mathrm{o}}$, the JRF at 60° abduction increased from 422 N of the generic model to 456 N (almost 8%).

The 50% reduction of PCSAs of RC muscles had negligible effects (less than 3%) on the JRF until 60° abduction (Fig. 2.5e). But, it caused the JRF to increase afterward. The maximum JRF increased to 682 N (less than 17%) and occurred at slightly higher abduction angles (130°) comparing to the generic model.

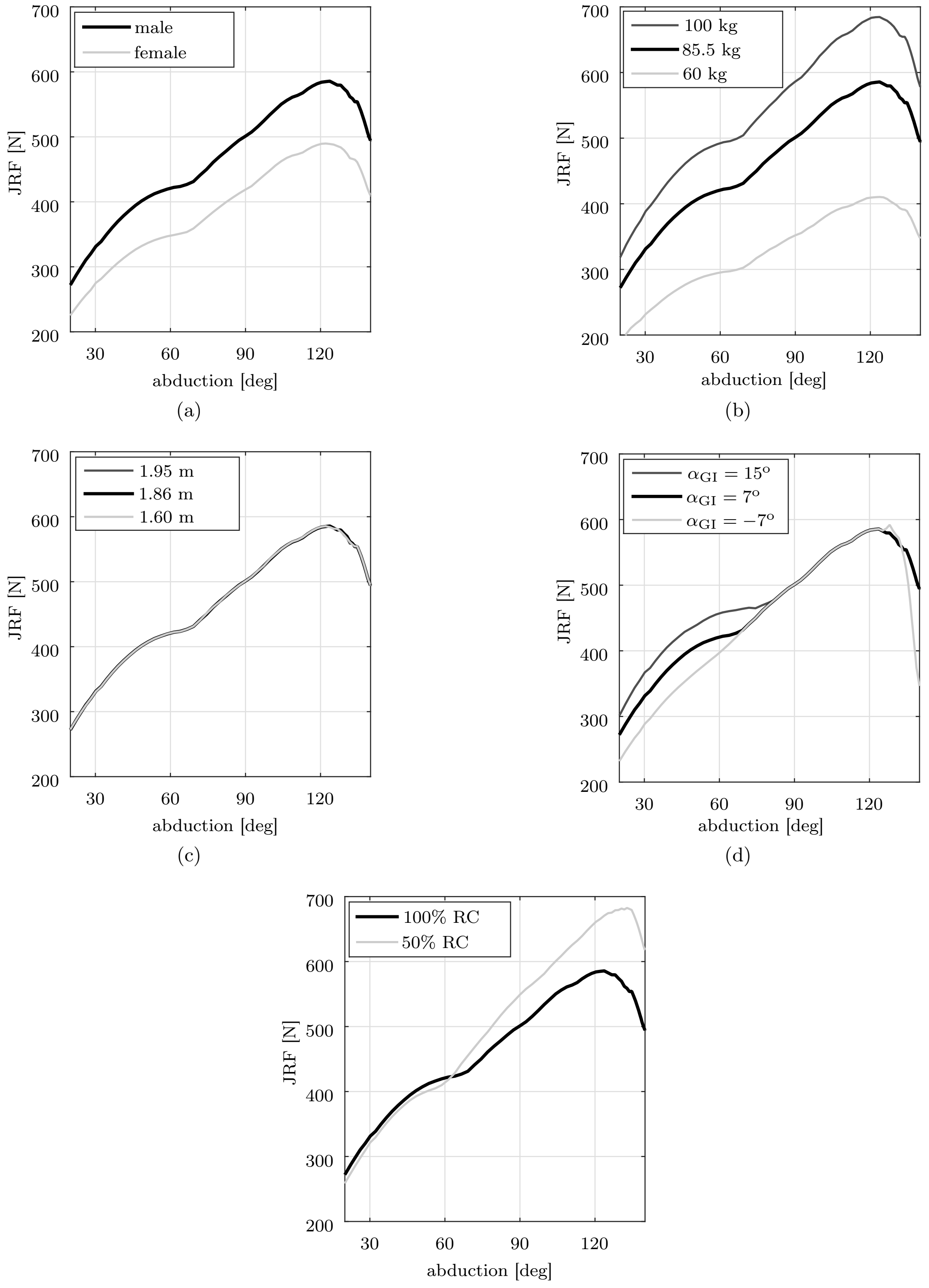

(a) (b)

(c) (d)

(e)

Figure 2.5: Evaluations of the effects of subject specific parameters on the JRF predictions during abduction motion in the scapula plane. (a) Gender, (b) weight, (c) height, (d) glenoid inclination, and (e) 50% reduction in PCSAs of RC muscles.

2.4 Discussion

The aim of this study was to develop a scaled-generic musculoskeletal model of shoulder and elbow. The elbow was incorporated into our previously developed shoulder model using two non-perpendicular hinge joints. Fourteen muscles spanning the elbow and shoulder were included in the model. Scaling routines were developed to scale the model's BSIP, skeletal morphologies, and muscles architectures to a specific subject. The model was developed on open-source principles as a Matlab toolbox. We specifically evaluated the effects of subject's gender, weight, height, glenoid inclination, and reductions in PCSAs of RC muscles on the JRF predictions during an abduction motion. The JRF prediction of the generic model was consistent with the *in vivo* measurements of the instrumented prosthesis [199] and other numerical studies [13, 17, 18].

The predicted JRF at 60°, 90°, and 120° were at most only 13% less than those of the instrumented prosthesis.

The reduction in JRF due to changing the subject's gender to female was expected. Because, it scaled down the arm weight (from almost 3.51 kg to 2.99 kg by around 15%). It also resulted in a slightly lower r_m (from 77.67 % to 67.36%) that reduced the PCSAs.

The weight had the most significant effect among the other parameters. Each extra Kilogram of subject's weight scaled up the arm weight by almost 1.17%. Therefore, the increase/decrease of the JRF due to increase/decrease of subject's weight was predictable. This effect would be faded away however, if the JRF was presented in body weight percentage. For instance, both variations of subject's weight together with the generic model resulted in JRF almost equal to 70% of body weight at 90° abduction.

The height had almost no effect on the JRF. The increase of the subject's height linearly increased the arm weight moment arm. The muscle moment arms were also equivalently increased due to scaling up the wrapping objects. Therefore, these two effects would cancel out each other, given that the changes in the inertial properties and the joint kinematics due to height were negligible.

The more downward the glenoid inclination was, the lower JRF was predicted until 60° abduction. This was consistent with the previous studies regarding the glenoid inclination [64, 101, 200]. Given that the GH joint was less stable for the beginning of abduction [31], the downward inclinations of the glenoid fossa could stabilize the joint by centering the JRF within the stability cone. Therefore, lower JRF was predicted. After 60° the joint was inherently more stable, provided by the scapula upward rotation. Therefore, the downward inclination of the fossa had negligible effects. The joint became less stable at the end of the abduction [58, 67], where the downward inclination could again play its stabilizing role.

We intuitively expected that the 50% reduction of the RC muscles PCSAs would increase the JRF until 60° abduction. Because, the impaired RC muscles supposedly could not perform their stabilizing task, and instead other muscle groups would carry out the task, but with less efficiency. However, the results predicted a slight decrease in JRF until 60° abduction. This could be explained by the fact that 50% reduction would not avoid RC muscles from performing their stabilizing task. It has been shown by several studies that the contributions of RC muscles during an abduction motion were limited to less than 50 N [13, 52, 188]. Therefore, according to the Fick law [206], they roughly required less than 2 cm^2 PCSAs to carry out their stabilizing task.

A parameter study typically required participants with different anthropometric parameters [88]. For instance, to evaluate the effect of height, several participants with different heights but ideally same weights were required [86]. To predict effects of kinematics on JRF predictions, kinematics of several subjects during a motion were required to be recorded [92, 207]. However, a strength of the developed toolbox was that it allowed performing the parameter study, while no participants was required. Because, the toolbox could numerically produce the kinematics associated to each virtual subject considered [100]. Provided by the model GUI, it also exempted the user from cumbersome programming.

One limitation of this study was that a fix carrying angle was considered for the elbow. The elbow carrying angle is the angle between the forearm and the humerus longitudinal axes. It was shown to vary during forearm motion [69]. A fixed carrying angle would therefore compromise the elbow kinematics during its task oriented motions [69, 208]. However, given that our model mainly focused on shoulder studies, this simplification could be justified. Another limitation referred to the fact that the model only included ideal joints with no translations. However, the GH joint translations play a crucial role in the joint functions and its stability mechanism [119]. Therefore, future developments would allow the model to predict GH joint translations by taking advantage of a framework that has been developed in our group [193]. Furthermore, we investigated the effects of each parameter separately. More thorough sensitivity analyses could be used to also show compound effects of parameters. A compromise of three factors namely sensitivity, variability, and measurability could then be used to decide whether a parameter must be personalized in a model [209]. For instance a highly sensitive parameter with very little variability which is also difficult to measure could be excluded from subject specific parameters. Finally, this study mainly dealt with presenting the toolbox and the underlying methodologies of its development. Indeed, further investigations were required to evaluate its predictions. It would also be interesting to compare its predictions with other existing free [210] or commercial [211] shoulder musculoskeletal packages.

In conclusion, we enhanced the realism and facilitated applications of an existing shoulder model by three main improvements. First, the elbow and the muscle groups spanning it were included in the model. Second, scaled-generic attributes were added to the resulting shoulder and elbow model. The model was finally developed as a Matlab toolbox with a GUI that facilitated its applications. We showed the effects of subject specific parameters on the JRF predictions. Given their considerable effects, it was concluded that their adaptation to each subject could enhance the realism of the model predictions. This work was a step toward subject specific modeling of shoulder and elbow. In a next step the toolbox would be populated with data from pre and post operative patients for clinical applications related to treatments of the GH joint osteoarthritis with total shoulder arthroplasty.

Appendix: Matlab toolbox

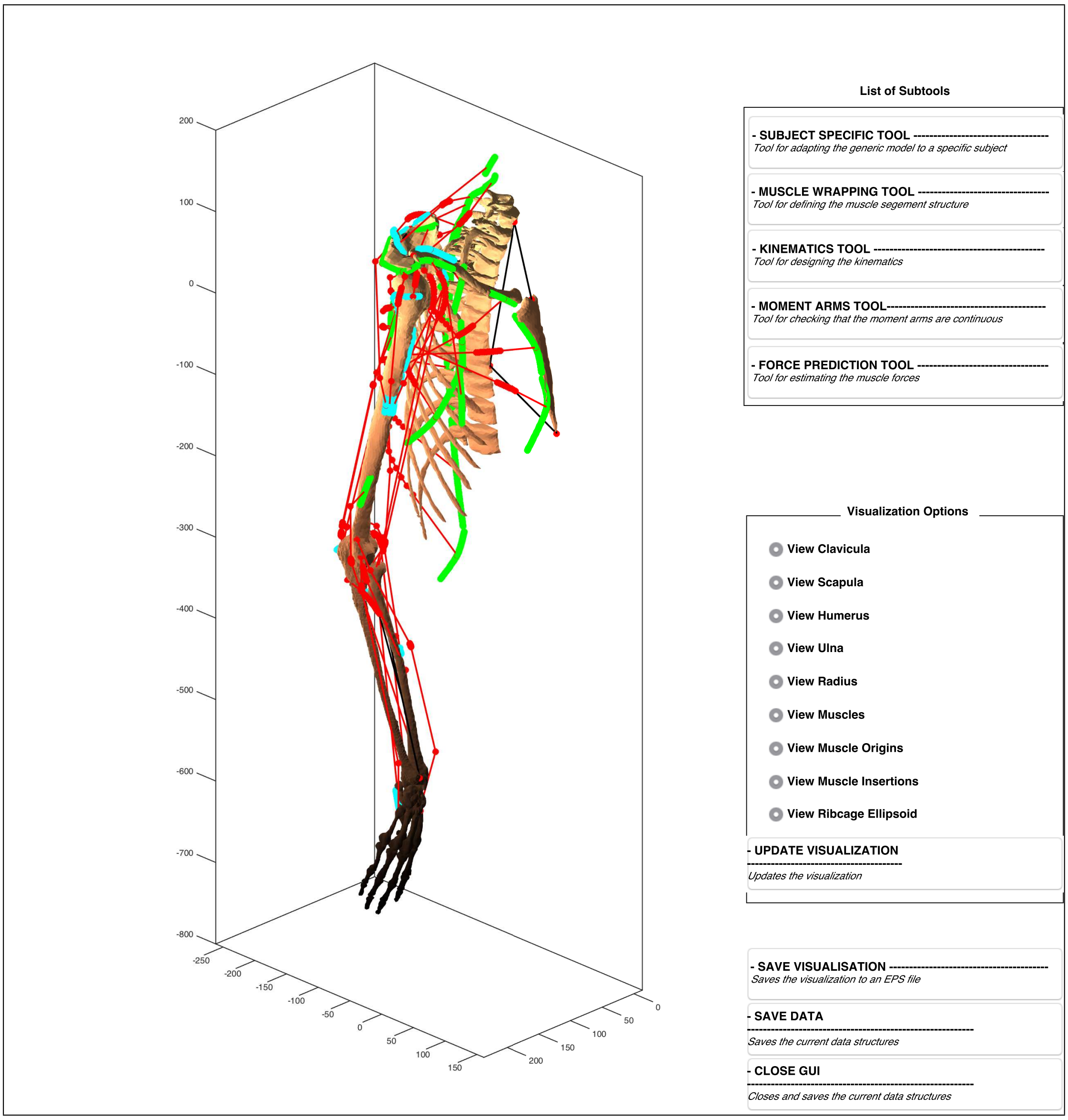

List of Subtools

- SUBJECT SPECIFIC TOOL ------------------------------------
Tool for adapting the generic model to a specific subject

- MUSCLE WRAPPING TOOL ------------------------------------
Tool for defining the muscle segement structure

- KINEMATICS TOOL --
Tool for designing the kinematics

- MOMENT ARMS TOOL--
Tool for checking that the moment arms are continuous

- FORCE PREDICTION TOOL -----------------------------------
Tool for estimating the muscle forces

Visualization Options

- ● View Clavicula
- ● View Scapula
- ● View Humerus
- ● View Ulna
- ● View Radius
- ● View Muscles
- ● View Muscle Origins
- ● View Muscle Insertions
- ● View Ribcage Ellipsoid

- UPDATE VISUALIZATION ------------------------------------
Updates the visualization

- SAVE VISUALISATION ---
Saves the visualization to an EPS file

- SAVE DATA --
Saves the current data structures

- CLOSE GUI --
Closes and saves the current data structures

Figure 2.6: Illustration of the main window of the developed shoulder and elbow Matlab toolbox. This window provides access to the 5 main sub-tools. It also allows customizing the visualization. Each window is equipped with a save and close push bottoms.

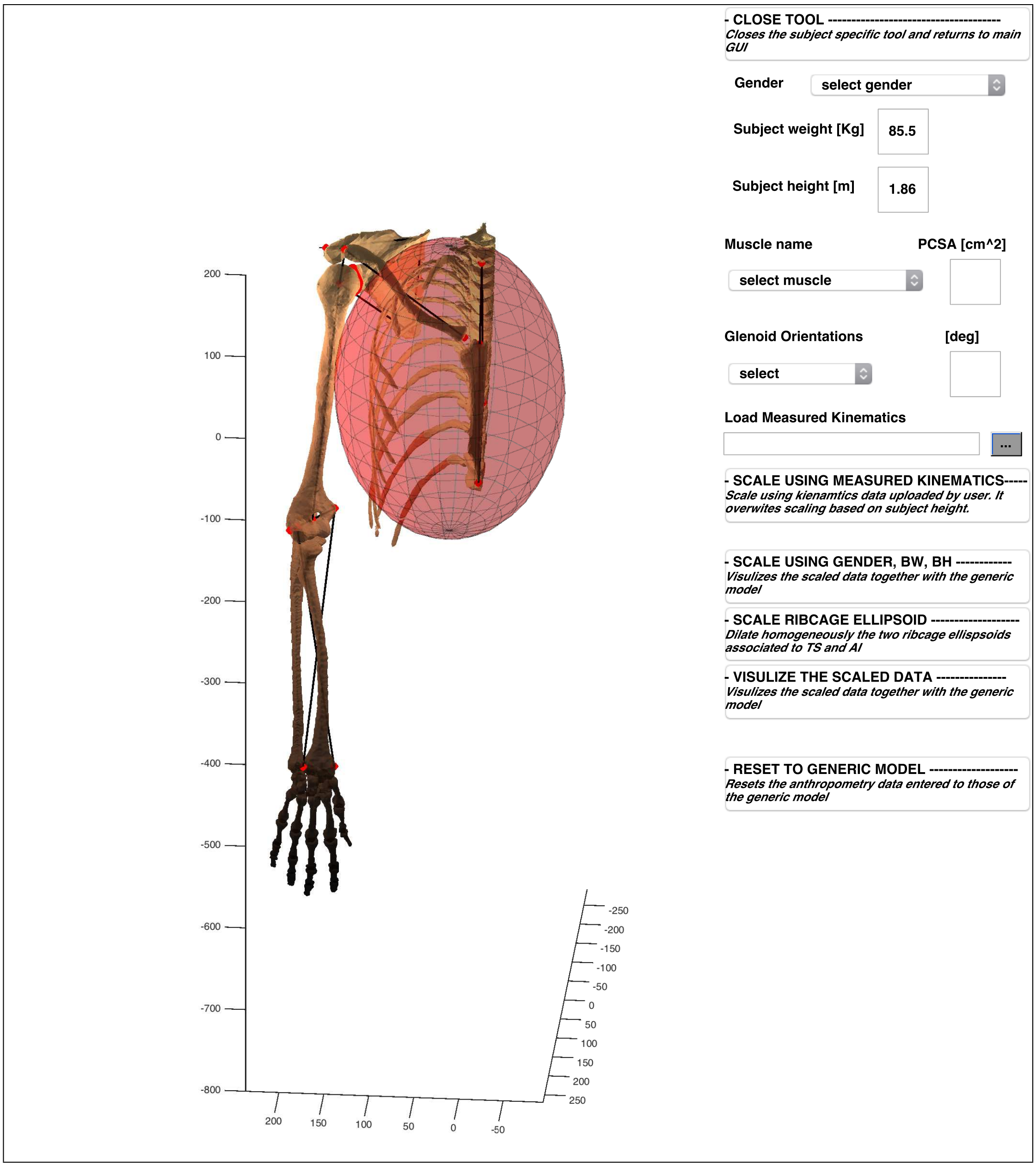

- CLOSE TOOL ------------------------------------
Closes the subject specific tool and returns to main GUI

Gender: select gender

Subject weight [Kg]: 85.5

Subject height [m]: 1.86

Muscle name: select muscle

PCSA [cm^2]:

Glenoid Orientations: select

[deg]:

Load Measured Kinematics:

- SCALE USING MEASURED KINEMATICS-----
Scale using kienamtics data uploaded by user. It overwites scaling based on subject height.

- SCALE USING GENDER, BW, BH ------------
Visulizes the scaled data together with the generic model

- SCALE RIBCAGE ELLIPSOID -------------------
Dilate homogeneously the two ribcage ellispsoids associated to TS and AI

- VISULIZE THE SCALED DATA ---------------
Visulizes the scaled data together with the generic model

- RESET TO GENERIC MODEL -------------------
Resets the anthropometry data entered to those of the generic model

Figure 2.7: The subject specific toolbox allows the user to scale the generic model through adapting subject's gender, height, weight, muscles PCSAs, and glenoid orientations (inclination and version). It also allows importing and scaling the model using kinematic measurement data in terms of trajectories of palpated landmarks. The model's BSIP, skeletal morphologies, and muscles architectures are scaled here. The scaled model can be visually compared to the generic model. The option for discarding the changes is indeed provided to set back the generic model.

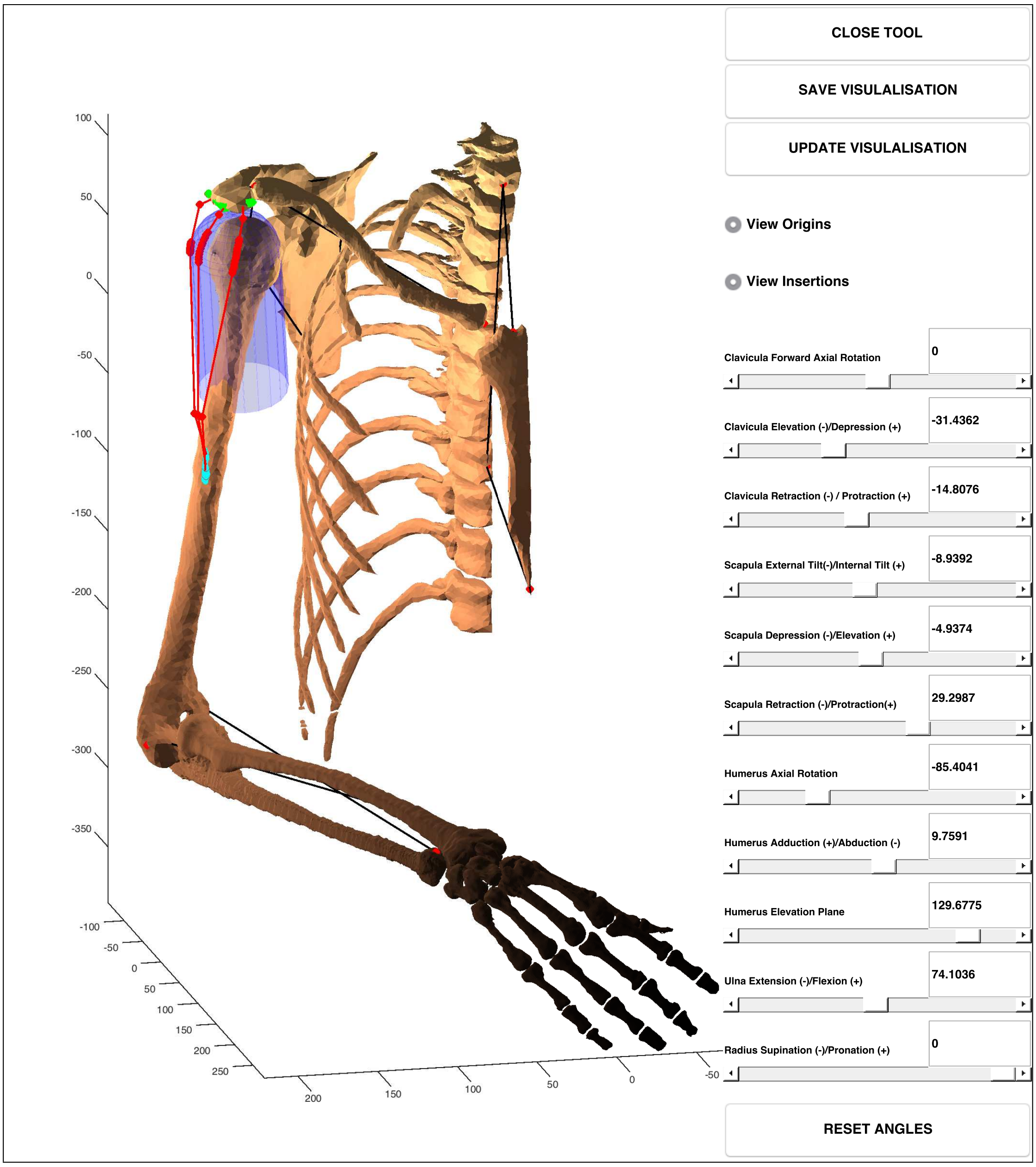

Clavicula Forward Axial Rotation 0

Clavicula Elevation (-)/Depression (+) -31.4362

Clavicula Retraction (-) / Protraction (+) -14.8076

Scapula External Tilt(-)/Internal Tilt (+) -8.9392

Scapula Depression (-)/Elevation (+) -4.9374

Scapula Retraction (-)/Protraction(+) 29.2987

Humerus Axial Rotation -85.4041

Humerus Adduction (+)/Abduction (-) 9.7591

Humerus Elevation Plane 129.6775

Ulna Extension (-)/Flexion (+) 74.1036

Radius Supination (-)/Pronation (+) 0

Figure 2.8: The muscle wrapping tool provides an interactive environment for visual verification of the muscle paths. The wrapping obstacles, via points, the origin (green), and the insertion (blue) can be checked. Different joint angles can be also imposed to perform the verification in different configurations.

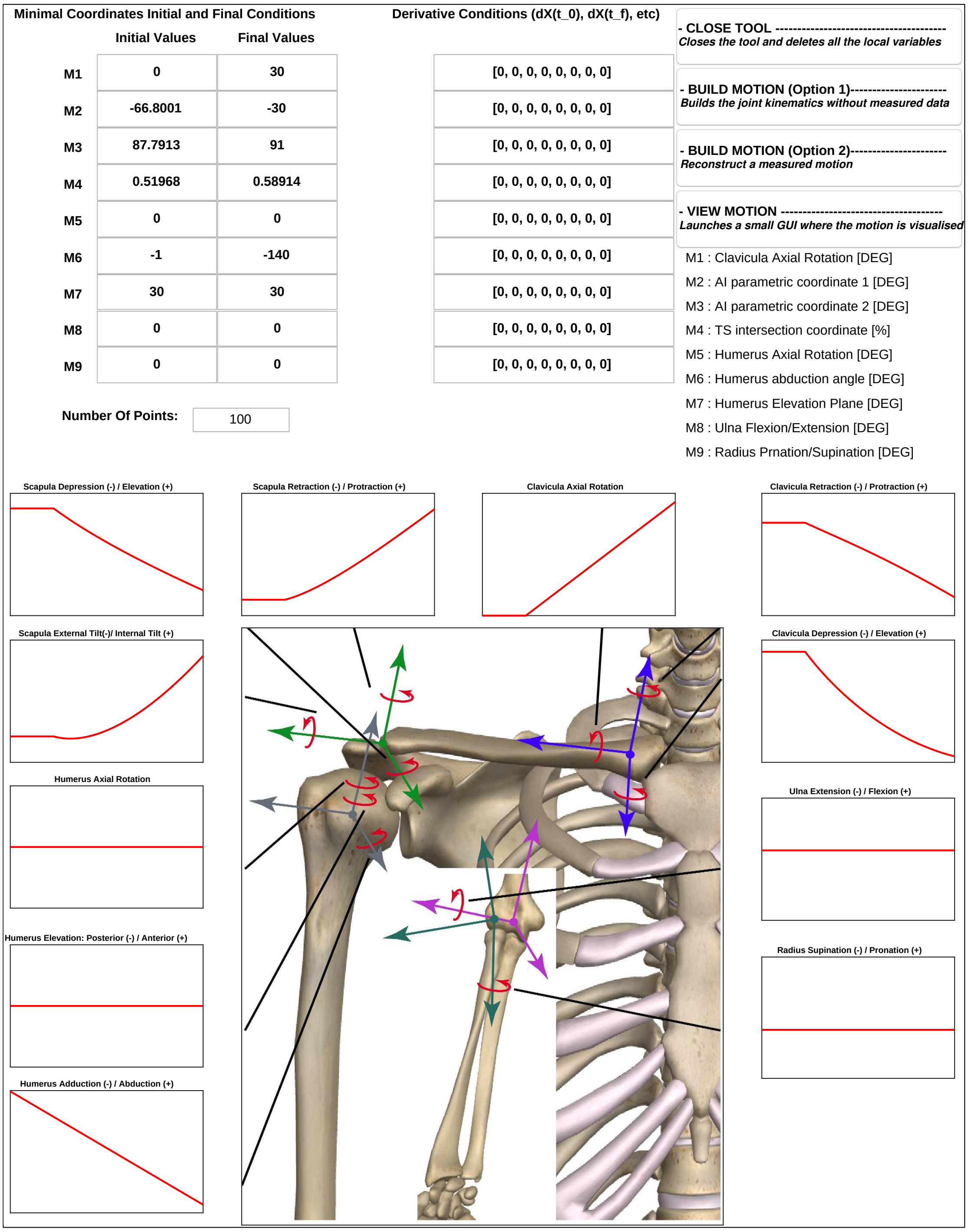

Minimal Coordinates Initial and Final Conditions

	Initial Values	Final Values	Derivative Conditions (dX(t_0), dX(t_f), etc)
M1	0	30	[0, 0, 0, 0, 0, 0, 0, 0]
M2	-66.8001	-30	[0, 0, 0, 0, 0, 0, 0, 0]
M3	87.7913	91	[0, 0, 0, 0, 0, 0, 0, 0]
M4	0.51968	0.58914	[0, 0, 0, 0, 0, 0, 0, 0]
M5	0	0	[0, 0, 0, 0, 0, 0, 0, 0]
M6	-1	-140	[0, 0, 0, 0, 0, 0, 0, 0]
M7	30	30	[0, 0, 0, 0, 0, 0, 0, 0]
M8	0	0	[0, 0, 0, 0, 0, 0, 0, 0]
M9	0	0	[0, 0, 0, 0, 0, 0, 0, 0]

Number Of Points: 100

- CLOSE TOOL --
Closes the tool and deletes all the local variables

- BUILD MOTION (Option 1)----------------------
Builds the joint kinematics without measured data

- BUILD MOTION (Option 2)----------------------
Reconstruct a measured motion

- VIEW MOTION -------------------------------------
Launches a small GUI where the motion is visualised

M1 : Clavicula Axial Rotation [DEG]
M2 : AI parametric coordinate 1 [DEG]
M3 : AI parametric coordinate 2 [DEG]
M4 : TS intersection coordinate [%]
M5 : Humerus Axial Rotation [DEG]
M6 : Humerus abduction angle [DEG]
M7 : Humerus Elevation Plane [DEG]
M8 : Ulna Flexion/Extension [DEG]
M9 : Radius Prnation/Supination [DEG]

Figure 2.9: The kinematics tool allows producing a motion for the shoulder and elbow through two different options. The first option does not require measurement data and is useful for conceptual studies such as parameter studies. The second option allows reconstruction of a measured motion using videogrammetry systems in terms of trajectories of palpated landmarks (Fig. 2.10).

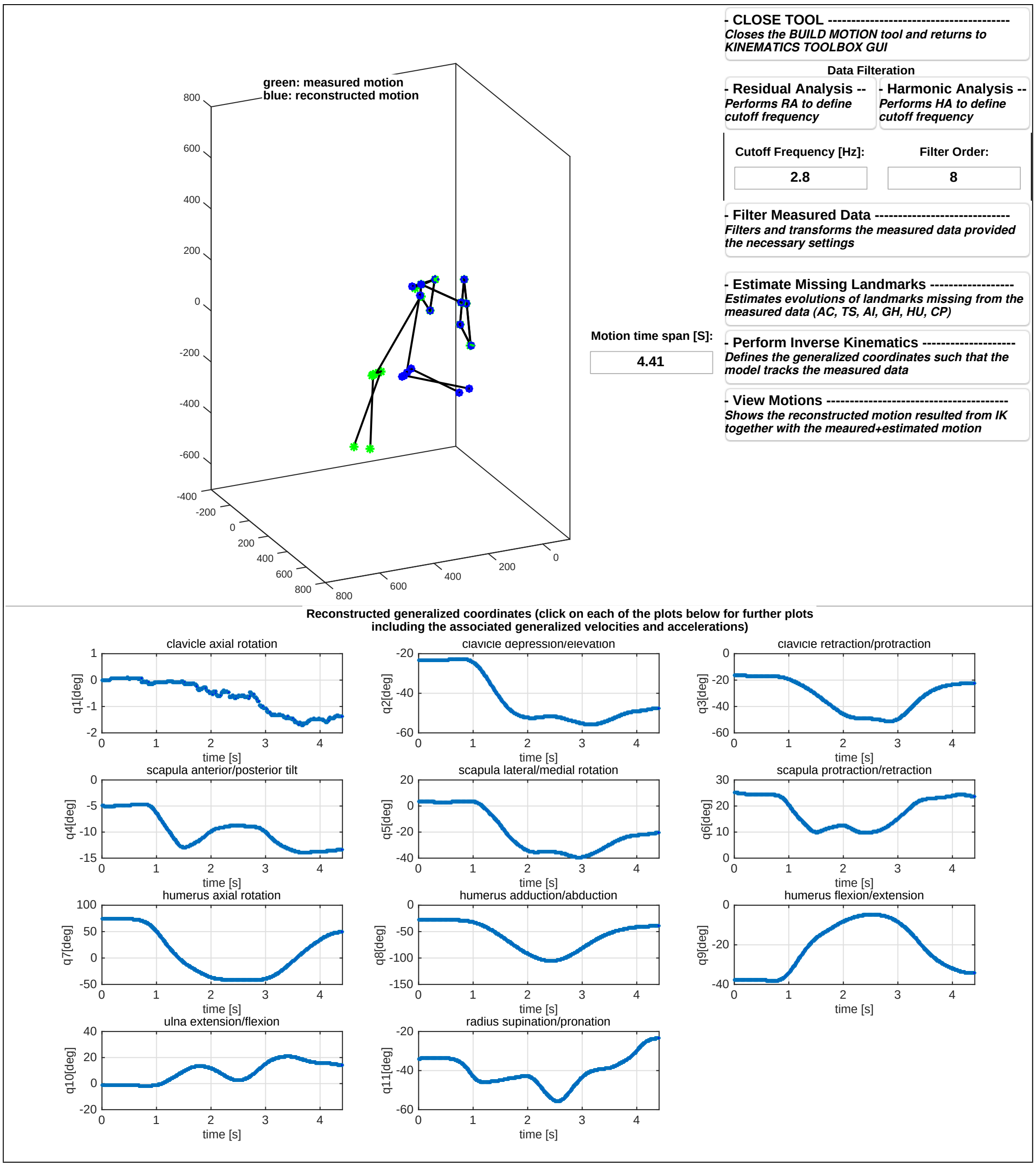

- CLOSE TOOL ---------------------------------------
Closes the BUILD MOTION tool and returns to KINEMATICS TOOLBOX GUI

Data Filteration

- Residual Analysis --
Performs RA to define cutoff frequency

- Harmonic Analysis --
Performs HA to define cutoff frequency

Cutoff Frequency [Hz]: 2.8

Filter Order: 8

- Filter Measured Data -----------------------------
Filters and transforms the measured data provided the necessary settings

- Estimate Missing Landmarks ------------------
Estimates evolutions of landmarks missing from the measured data (AC, TS, AI, GH, HU, CP)

Motion time span [S]: 4.41

- Perform Inverse Kinematics --------------------
Defines the generalized coordinates such that the model tracks the measured data

- View Motions ---------------------------------------
Shows the reconstructed motion resulted from IK together with the meaured+estimated motion

Reconstructed generalized coordinates (click on each of the plots below for further plots including the associated generalized velocities and accelerations)

Figure 2.10: The second option of the kinematics tool uses the imported measurements from the subject specific tool. It analyzes and filters the measured data. It provides estimations of the missing landmarks and scapula kinematics, even if it is not measured explicitly using scapula kinematic measurement devices. It reconstructs the motion in terms of the joint angles using multi-segment optimization (inverse kinematics). The reconstructed motion can be animated and saved.

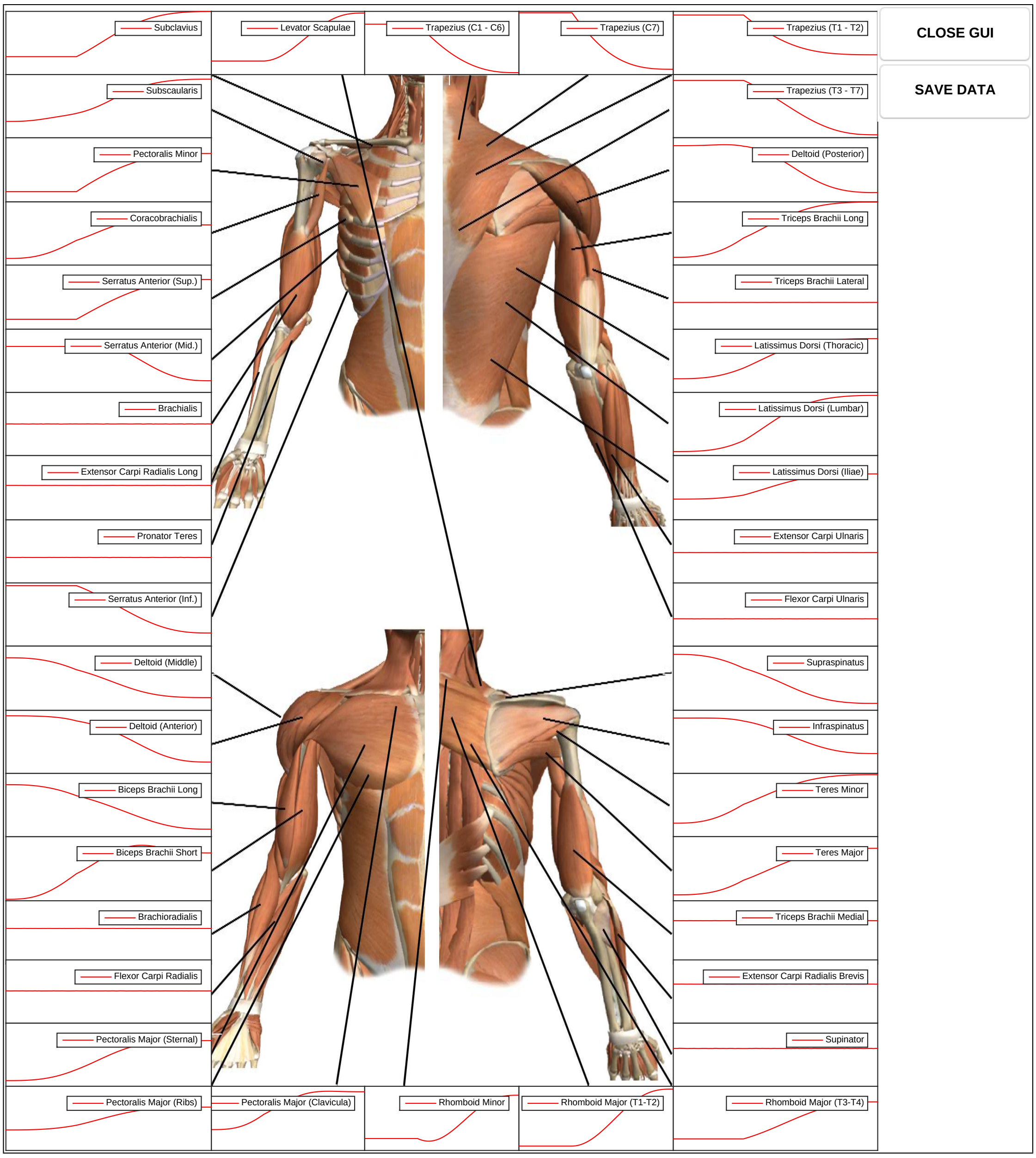

Figure 2.11: The moment arms tool calculates the moment arms of the muscles for the simulated motion. The interactive design of this tool allows the user to obtain further details regarding the moment arms of each muscle by a single click. The moment arms around different joints and the muscle length are included for each muscle.

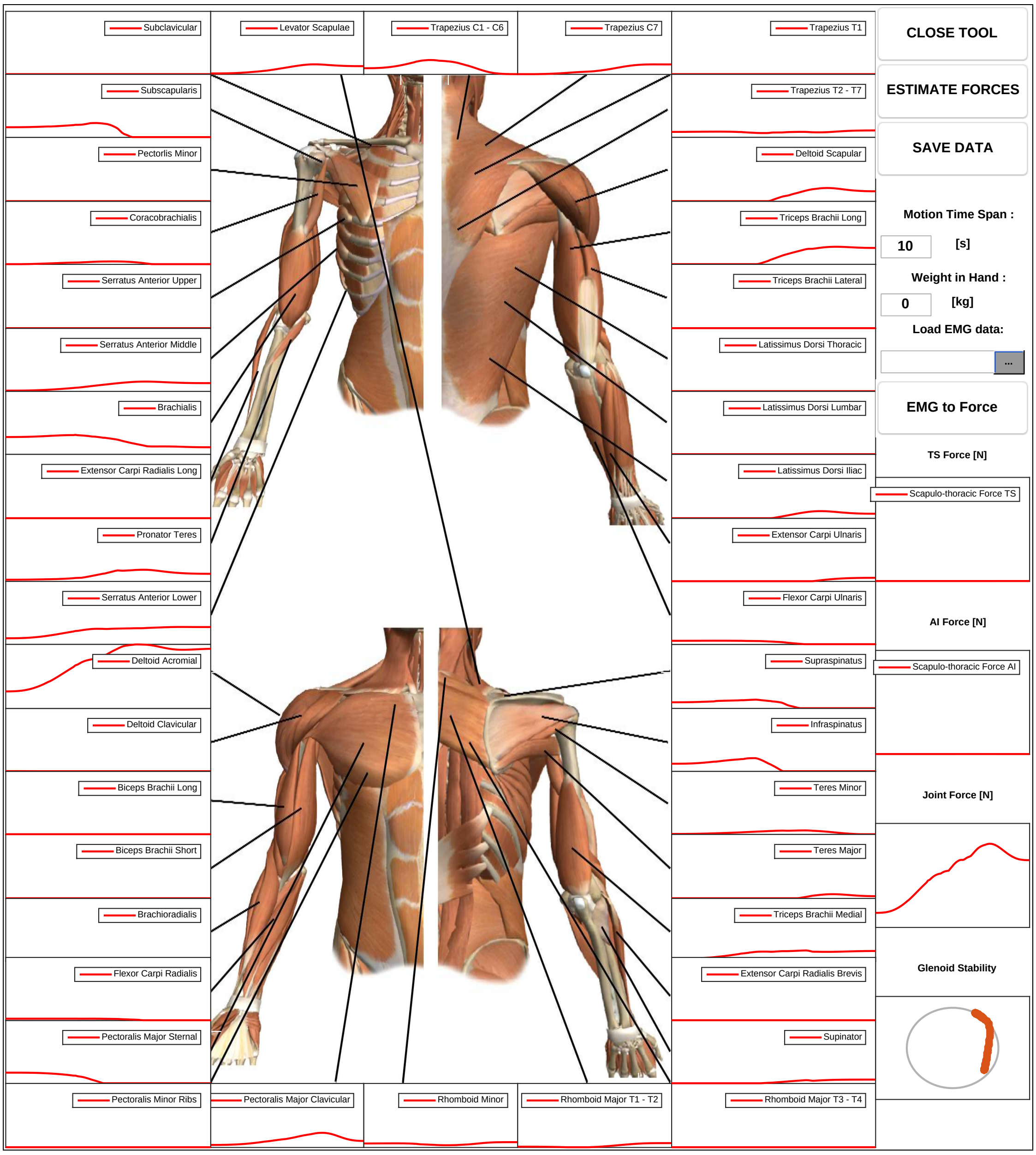

Motion Time Span : 10 [s]

Weight in Hand : 0 [kg]

Figure 2.12: Finally, the force prediction tool provides predictions of the muscle forces and JRF for the simulated motion. The subject can alternate the speed of the motion and also the weight that the subject carries during the motion. It also includes EMG-assisted load-sharing approach of the model that is not discussed in this study [212].

3 A Simulation Framework for Humeral Head Translations

This chapter is a preprint version of the following self-authored article that has been published in Journal of Medical Engineering and Physics.

Ehsan Sarshari, Alain Farron, Alexandre Terrier, Dominique Pioletti, Philippe Mullhaupt, “A simulation framework for humeral head translations”, Medical Engineering and Physics 49 (2017) 140-147.

Abstract

Humeral head translations (HHT) play a crucial role in the glenohumeral (GH) joint function. The available shoulder musculoskeletal models developed based on inverse dynamics however fall short of predicting the HHT. This study aims at developing a framework that allows forward-dynamics simulation of a shoulder musculoskeletal model with a six DOF GH joint. It provides a straightforward solution to the HHT problem. We show that even within a forward-dynamics simulation addressing the HHT requires further information about the contact. To that end, a deformable articular contact is included in the framework defining the GH joint contact force in terms of the joint kinematics. An abduction motion in the scapula plane is simulated. The results are given in terms of HHT, GH joint contact force, contact areas, contact pressure, and cartilage strain. It predicts a superior-posterior translation of the humeral head followed by an inferior migration.

3.1 Introduction

Several musculoskeletal models are available for the human shoulder that provide predictions of both the muscle and joint reaction forces e.g. [14, 28]. A vast majority of these models have been developed based on inverse dynamics, e.g. [13, 14, 16, 44, 45, 100]. In inverse dynamics the muscle forces are defined for a given (measured) joints kinematics. However, with the available measurement techniques, it is not straightforward to measure the translational DOFs of the GH joint [8]. Therefore, it is often approximated as an ideal ball-and-socket joint in the musculoskeletal models, neglecting its translations [119]. Nonetheless, the GH joint translations has a key impact on the GH joint function, specially its stability mechanism [28, 120]. Furthermore, predictions of the GH joint translations, the contact pressure, and the contact areas are required in designing shoulder prostheses [121, 122].

Indeed, few studies have investigated the HHT using biomechanical models. To this end, they tailored either available musculoskeletal models [122, 123] or developed finite element models [119, 121, 124, 125]. Other studies mainly used cadaveric [126, 127] or clinical [8, 128–133] approaches to address the GH joint translations. However, there are limitations associated to each of these studies.

The Anybody shoulder model [44] was tailored using the force dependent kinematic method, introduced in [134], to address the HHT after total shoulder arthroplasty (TSA) [122]. The dynamic effects of motion were neglected although their influence on the HHT has been already highlighted [128]. The Portuguese shoulder model [17] was adapted in [123] to address the HHT using a novel inverse-dynamics framework. The HHT was considered as an extra design variable in an optimization scheme within this framework. Despite [122], the dynamic effects of motion were partially considered. However, the articular contact was approximated by an elastic potential function. This deviates from the nonlinear and viscoelastic behavior of the cartilage [135] and does not account for the moment applied on the humerus due to the articular contact. The different 3D finite element models developed in [119, 121, 124, 125] share the same attributes. They include more realistic estimation for the articular contact although they were simulated under a sequence of static conditions, neglecting the dynamics of motion. Furthermore, they all lack a physiological muscle force load-sharing. The 3D finite element model developed in [119] was used in [120, 136, 137] to further study the HHT after the TSA.

The *in vivo* or *in vitro* measurement of the HHT remains a challenging task [8]. Specifically, *in vitro* studies could not accurately simulate the *in vivo* conditions in terms of the muscle and joint contact forces. The *in vivo* studies were also either limited to 2D analysis [128, 129] or otherwise their accuracy was limited by the 3D reconstruction of the bones [8, 132, 133]. Furthermore, they were not developed to assess the GH joint translations during dynamic activities [130, 131].

The aim of this study is to develop a framework for forward-dynamics simulation of a shoulder musculoskeletal model that allows estimation of the HHT. It has three main strengths: 1) the dynamic effects of motion is naturally considered, 2) a nonlinear viscoelastic approximation for the articular contact is used, and 3) it provides an integrated solution that deals simultaneously with the GH joint kinematics and kinetics. To the best of our knowledge this has not been addressed elsewhere. This framework provides addressing the GH joint translations either in its physiological form or after the TSA.

3.2 Methods

A musculoskeletal model of the GH joint with six DOFs is developed. The six DOFs correspond to three rotational and three translational (HHT) generalized coordinates. We show that the equations of motion of the GH joint with six DOFs is indeterminate, i.e. there are fewer equations than the number of unknown forces and moments and unknown generalized coordinates (subsection 3.2.1). Therefore, defining the HHT requires solving the indeterminate equations of motion of the GH joint. In order to resolve the indeterminacy, we develop a framework that maps the unknown forces and moments to the unknown generalized coordinates and velocities (subsections 3.2.3 and 3.2.3). This leads to a set of transformed equations of motion that no longer is indeterminate. We then simulate an arm motion in the scapula plane. The resulted HHT, GH joint contact force, contact areas, contact pressure, and cartilage strain are compared to those from the *in vitro*, *in vivo*, and numerical studies.

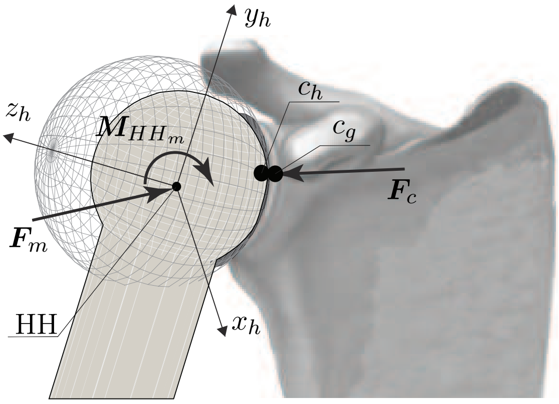

Figure 3.1: A schematic view of the GH joint. The surfaces of humeral head and the glenoid fossa are both approximated as spheres. $x_h y_h z_h$ is the humerus body-fixed frame attached to the humeral head center HH. $\boldsymbol{F}_m$ and $\boldsymbol{M}_{HH_m}$ are resultant force and moment due to the muscles, and $\boldsymbol{F}_c$ is the contact force. The contact points on the humeral head and the glenoid fossa are denoted by C_h and C_g, respectively.

3.2.1 Indeterminacy in HHT

The surfaces of humeral head and glenoid fossa are both approximated as spheres with radii r_h and r_g equal to 30 mm and 32 mm, respectively [213] (Fig. 3.1). The arm weight is 35.7 N that corresponds to 5% of the bodyweight. All the 11 major muscles spanning the GH joint are included, and their forces applied on the humerus are replicated by a resultant force $\boldsymbol{F}_m$ and a resultant moment $\boldsymbol{M}_{HH_m}$ acting on the humeral head center. Muscle paths are defined using the algorithm introduced in [16]. $\boldsymbol{F}_c$ represents the GH joint contact force applied on the humerus. The contact point on the humeral head and its associate point on the glenoid fossa are denoted by C_h and C_g, with velocities of $\boldsymbol{V}_{C_h}$ and $\boldsymbol{V}_{C_g}$, respectively. A body-fixed frame ($x_h y_h z_h$) is attached to the humerus at the humeral head center (HH). The scapula motion is included by the scapulohumeral rhythm [52].

The GH joint equations of motion are derived using the Lagrange's equations. A compact form of these equations is

$$\frac{d}{dt}\left(\frac{\partial L}{\partial \dot{\boldsymbol{q}}}\right) - \frac{\partial L}{\partial \boldsymbol{q}} = \boldsymbol{\tau}(\boldsymbol{F}_m, \boldsymbol{M}_{HH_m}, \boldsymbol{F}_c) \tag{3.1}$$

The generalized coordinate vector $\boldsymbol{q}$ consists of three rotational DOFs (ψ, θ, and ϕ) and three translational DOFs (x, y, and z). The generalized force vector $\boldsymbol{\tau}$ is a function of applied external forces and moments ($\boldsymbol{F}_m$, $\boldsymbol{M}_{HH_m}$, and $\boldsymbol{F}_c$) [11]. A holonomic constraint is also considered to account for the contact between the surfaces of humeral head and glenoid fossa

$$(\boldsymbol{V}_{C_h} - \boldsymbol{V}_{C_g})\,.\,\hat{\boldsymbol{n}} = 0 \tag{3.2}$$

The unit vector $\hat{\boldsymbol{n}}$ is perpendicular to the plane of contact that is tangential to the contact point. The constraint equation assures no relative velocity between C_h and C_g in the direction of $\hat{\boldsymbol{n}}$ [214].

There are fifteen unknowns in Eq. 3.1 and Eq. 3.2, including the six generalized coordinates (ψ, θ, ϕ, x, y, and z), the three components of the contact force ($\boldsymbol{F}_c$), the three components of the resultant muscle force ($\boldsymbol{F}_m$), and the three components of the resultant muscle moments ($\boldsymbol{M}_{HH_m}$). However, Eq. 3.1 and Eq. 3.2 respectively provide six and one equations (seven in total) that are not sufficient to uniquely determine the fifteen unknowns. Therefore, the equations of motion of the GH joint with six DOFs is indeterminate.

3.2.2 Resolving the indeterminacy: deformable articular contact

Our approach to resolve the indeterminacy is to define the unknown muscle and contact forces and their associated moments as smooth function mappings of the generalized coordinate and velocity vectors. This leads to a set of transformed equations of motion that is no longer indeterminate.

Using the definition of virtual work [11], the generalized force vector ($\boldsymbol{\tau}$) on the right-hand side of Eq. 3.1 can be expressed as

$$\boldsymbol{\tau} = \frac{\partial \boldsymbol{V}_{HH}^T}{\partial \dot{\boldsymbol{q}}}(\boldsymbol{F}_m + \boldsymbol{F}_c) + \frac{\partial \boldsymbol{\omega}^T}{\partial \dot{\boldsymbol{q}}}(\boldsymbol{M}_{HH_m} + \boldsymbol{M}_{HH_c}) \tag{3.3}$$

Where $\boldsymbol{V}_{HH}$ is the velocity of the humeral head center, and $\boldsymbol{\omega}$ is the angular velocity of the humerus, and T is the matrix transpose operator. $\boldsymbol{M}_{HH_m}$ and $\boldsymbol{M}_{HH_c}$ denote the resultant moments about the humeral head center due to the muscle and the contact forces, respectively.

Substituting $\boldsymbol{F}_c$, $\boldsymbol{F}_m$, $\boldsymbol{M}_{HH_c}$, and $\boldsymbol{M}_{HH_m}$ in Eq. 3.3 with smooth function mappings (to be defined) of $\boldsymbol{q}$ and $\dot{\boldsymbol{q}}$ and introducing the resulting generalized force vector into Eq.

3.1, we obtain

$$\begin{aligned}\frac{d}{dt}\left(\frac{\partial L}{\partial \dot{\boldsymbol{q}}}\right)-\frac{\partial L}{\partial \boldsymbol{q}} &= \frac{\partial \boldsymbol{V}_{HH}^{T}}{\partial \dot{\boldsymbol{q}}}\mathscr{F}_{c}(\boldsymbol{q},\dot{\boldsymbol{q}})+\frac{\partial \boldsymbol{\omega}^{T}}{\partial \dot{\boldsymbol{q}}}\mathscr{M}_{HH_c}(\boldsymbol{q},\dot{\boldsymbol{q}}) \\ &+\frac{\partial \boldsymbol{V}_{HH}^{T}}{\partial \dot{\boldsymbol{q}}}\mathscr{F}_{m}(\boldsymbol{q},\dot{\boldsymbol{q}})+\frac{\partial \boldsymbol{\omega}^{T}}{\partial \dot{\boldsymbol{q}}}\mathscr{M}_{HH_m}(\boldsymbol{q},\dot{\boldsymbol{q}})\end{aligned} \tag{3.4}$$

Where $\mathscr{F}_c$, $\mathscr{F}_m$, $\mathscr{M}_{HH_c}$, and $\mathscr{M}_{HH_m}$ are the smooth function mappings from $\boldsymbol{q}$ and $\dot{\boldsymbol{q}}$ to $\boldsymbol{F}_c$, $\boldsymbol{F}_m$, and their associated moments. Once these function mappings are defined, solving the transformed equations of motion Eq. 3.4 is trivial.

To define $\mathscr{F}_c$, a deformable articular contact between the humeral head and the glenoid fossa is assumed. This contradicts our previous contact constraint in Eq. 3.2 where a rigid contact was assumed. However, the assumption of a deformable articular contact is more physiologically consistent [28, 215] and allows us to define $\mathscr{F}_c$. The deformable contact model used here is adapted from [216] approximating the cartilage as a nonlinear elastic material. A viscous damping term is also incorporated to this contact model according to [215]. The humeral head is considered to be rigid while a deformable layer covers the glenoid fossa (Fig. 3.2). The thickness of this deformable layer accounts for the cartilage of both humeral head and glenoid fossa. The vector $\boldsymbol{r}_{HH}$ defines the position of the humeral head center in the scapula frame $(x_s y_s z_s)$. We denote respectively by ${}_s\boldsymbol{h}_i$ and $\boldsymbol{h}_i$ the center point of an infinitesimal surface on the humeral head in the scapula and humerus frames and by $\boldsymbol{f}_{c_i}$ its associated contact force. According to [216] and [215], the contact force applied on $\boldsymbol{h}_i$ can be express as

$$\boldsymbol{f}_{c_i}=\begin{cases}\left(a_i\, s\, \mathrm{Ln}\left(1-\dfrac{u_i}{b}\right)+c\,\dot{u}_i\right)\dfrac{{}_s\boldsymbol{h}_i}{|{}_s\boldsymbol{h}_i|} & , \quad u_i>0 \\ \mathbf{0} & , \quad u_i<0\end{cases} \tag{3.5}$$

Where a_i, s, b, and c are the infinitesimal surface area, the aggregate module, the cartilage thickness, and the damping coefficient, respectively. We denote by u_i the amount that $\boldsymbol{h}_i$ penetrates the sphere approximating the glenoid fossa. Therefore, u_i is defined as $(|{}_s\boldsymbol{h}_i|-r_g)$ where ${}_s\boldsymbol{h}_i$ is $(\boldsymbol{r}_{HH}+{}^{S}_{H}R\ \boldsymbol{h}_i)$ with ${}^{S}_{H}R$ being the rotation matrix from the humerus frame to the scapula frame. The numerical values for the constants are adapted from the literature [119, 135, 217].

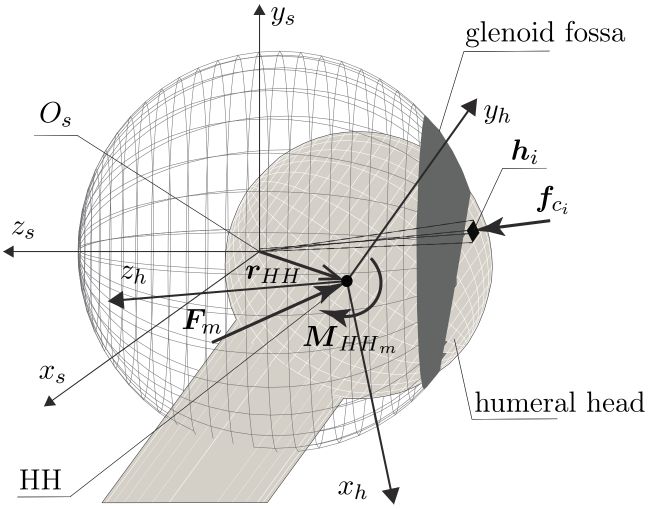

Figure 3.2: The GH joint with deformable articular contact (the dimensions are exaggerated for illustrations purposes). $\boldsymbol{r}_{HH}$ defines the spatial position of the HH in the scapula frame $(x_s y_s z_s)$. The center point of an infinitesimal surface on the humeral head in the humerus frames is denoted by $\boldsymbol{h}_i$, and $\boldsymbol{f}_{c_i}$ denotes its associated contact force.

3.2.3 Resolving the indeterminacy: forward-dynamics simulation

Having defined the function mapping $\mathscr{F}_c$, we here develop a forward-dynamics framework to define $\mathscr{M}_{HH_m}$. The forward-dynamics framework is a continuation of our previous work [218]. We define $\mathscr{M}_{HH_m}$ and accordingly $\boldsymbol{M}_{HH_m}$ such that the rotational generalized coordinates and velocities ($\boldsymbol{q}_r$ and $\dot{\boldsymbol{q}}_r$) follow their associated desired trajectory ($\boldsymbol{q}_{r_d}$ and $\dot{\boldsymbol{q}}_{r_d}$). To that end, we expand the transformed equations of motion Eq. 3.4 and split it into rotational and translational subspaces ($\boldsymbol{q}_r$ and $\boldsymbol{q}_t$):

$$\begin{aligned}\begin{bmatrix} M_{11} & M_{12} \\ M_{12} & M_{22} \end{bmatrix}\begin{bmatrix} \ddot{\boldsymbol{q}}_r \\ \ddot{\boldsymbol{q}}_t \end{bmatrix} + \boldsymbol{c}(\boldsymbol{q},\dot{\boldsymbol{q}}) + \boldsymbol{g}(\boldsymbol{q}) - \frac{\partial \boldsymbol{V}_{HH}^T}{\partial \dot{\boldsymbol{q}}}\mathscr{F}_c - \frac{\partial \boldsymbol{\omega}^T}{\partial \dot{\boldsymbol{q}}}\mathscr{M}_{HH_c} \\ = \frac{\partial \boldsymbol{V}_{HH}^T}{\partial \dot{\boldsymbol{q}}}\mathscr{F}_m + \frac{\partial \boldsymbol{\omega}^T}{\partial \dot{\boldsymbol{q}}}\mathscr{M}_{HH_m}\end{aligned} \tag{3.6}$$

Where $[M]$, $\boldsymbol{c}$, and $\boldsymbol{g}$ are the inertia matrix, centrifugal and Coriolis torques vector, and gravitational torques vector, respectively. $\mathscr{F}_c$ and consequently $\mathscr{M}_{HH_c}$ are already defined in subsection 3.2.2.

We denote by $\{f_m\}$ a vector that consists of the magnitudes of the forces applied by different muscles. Two matrices B and W are also defined mapping $\{f_m\}$ to $\boldsymbol{F}_m$ and $\boldsymbol{M}_{HH_m}$, respectively. B is the matrix composed of the muscle force directions, and W is the moment arm matrix. Making these substitutions and denoting by $\boldsymbol{L}$ the four last terms on the left-hand side of Eq. 3.6, we obtain

$$\begin{bmatrix} M_{11} & [0] \\ [0] & M_{22} \end{bmatrix} \begin{bmatrix} \ddot{\boldsymbol{q}}_r \\ \ddot{\boldsymbol{q}}_t \end{bmatrix} + \begin{bmatrix} \boldsymbol{L}_r(\boldsymbol{q}, \dot{\boldsymbol{q}}) \\ \boldsymbol{L}_t(\boldsymbol{q}, \dot{\boldsymbol{q}}) \end{bmatrix} = \frac{\partial \boldsymbol{V}_{HH}^T}{\partial \dot{\boldsymbol{q}}} B\{f_m\} + \frac{\partial \boldsymbol{\omega}^T}{\partial \dot{\boldsymbol{q}}} W\{f_m\} \tag{3.7}$$

Substituting $\frac{\partial \boldsymbol{V}_{HH}^T}{\partial \dot{\boldsymbol{q}}} B$ and $\frac{\partial \boldsymbol{\omega}^T}{\partial \dot{\boldsymbol{q}}} W$ by B_g and W_g, and eliminating their zero raws accordingly, yields

$$\begin{bmatrix} M_{11} & [0] \\ [0] & M_{22} \end{bmatrix} \begin{bmatrix} \ddot{\boldsymbol{q}}_r \\ \ddot{\boldsymbol{q}}_t \end{bmatrix} + \begin{bmatrix} \boldsymbol{L}_r(\boldsymbol{q}, \dot{\boldsymbol{q}}) \\ \boldsymbol{L}_t(\boldsymbol{q}, \dot{\boldsymbol{q}}) \end{bmatrix} = \begin{bmatrix} W_g\{f_m\} \\ B_g\{f_m\} \end{bmatrix} \tag{3.8}$$

Equation Eq. 3.8 allows us to define the magnitudes of the muscle forces such that the humerus follows a desired rotational trajectory. The rotational subspace of the transformed equations of motion Eq. 3.8 is

$$M_{11}\ddot{\boldsymbol{q}}_r + \boldsymbol{L}_r(\boldsymbol{q}, \dot{\boldsymbol{q}}) = W_g\{f_m\} \tag{3.9}$$

Where it can be solved for $\ddot{\boldsymbol{q}}_r$

$$\ddot{\boldsymbol{q}}_r = {M_{11}}^{-1}(W_g\{f_m\} - \boldsymbol{L}_r(\boldsymbol{q}, \dot{\boldsymbol{q}})) \tag{3.10}$$

The right-hand side of Eq. 3.10 is considered as a new intermediate control input $\boldsymbol{v}$ [219]. This results in an equivalent linear system

$$\ddot{\boldsymbol{q}}_r = \boldsymbol{v} \tag{3.11}$$

We define the tracking error as $\widetilde{\boldsymbol{q}}_r = \boldsymbol{q}_r - \boldsymbol{q}_{r_d}$. Letting

$$\boldsymbol{v} = \ddot{\boldsymbol{q}}_{r_d} - 2\lambda\dot{\widetilde{\boldsymbol{q}}}_r - \lambda^2\widetilde{\boldsymbol{q}}_r \quad , \quad \lambda > 0 \tag{3.12}$$

results in an exponentially stable closed-loop dynamics for Eq. 3.11. Having defined $\boldsymbol{v}$, the function mapping $\mathscr{M}_{HH_m}$ and accordingly $W_g\{f_m\}$ can be achieved by substituting $\ddot{\boldsymbol{q}}_r$ from Eq. 3.11 into Eq. 3.9. Given that the raw size of $\{f_m\}$ is larger than the rank of W_g, a static optimization is used to arrive at a set of nontrivial muscle force magnitudes ($\{f_m\}$):

$$\begin{array}{ll} \text{min.} & \{f_m\}^T \; E \; \{f_m\} \\ \text{s.t.} & M_{11}\boldsymbol{v} + \boldsymbol{L}_r(\boldsymbol{q}, \dot{\boldsymbol{q}}) = W_g\{f_m\} \\ & \{f_m\}^{min} \leq \{f_m\} \leq \{f_m\}^{max} \end{array} \tag{3.13}$$

Where E is a weighting matrix consisting of the physiological cross section areas of the muscles, and $\{f_m\}^{min}$ and $\{f_m\}^{max}$ are the lower and upper bounds on the muscle force magnitudes, respectively [52]. The cost function is the sum of squares of the muscle stresses [14].

3.2.4 Simulation of the framework

For a given desired rotational trajectory ($\boldsymbol{q}_{r_d}$), the developed framework allows forward-dynamics simulation of the GH joint model with six DOFs (Fig. 3.3). The muscle force magnitudes ($\{f_m\}$) are defined by the forward-dynamics framework such that the rotational generalized coordinates and velocities ($\boldsymbol{q}_r$ and $\dot{\boldsymbol{q}}_r$) of the GH joint follow their associated desired trajectories ($\boldsymbol{q}_{r_d}$ and $\dot{\boldsymbol{q}}_{r_d}$). The forward-dynamics framework consists of a feedforward and a feedback controller. The feedforward controller defines the gross control input based on Eq. 3.10, and the feedback controller has a fine action to compensate for the tracking errors Eq. 3.12. The rotational motions of the joint together with the muscle forces that are applied to generate these rotational motions may lead to GH joint translations. The evolutions of these translations are captured through the three translational DOFs ($\boldsymbol{q}_t$) of the GH joint model.

The deformable articular contact model defines the contact forces ($\boldsymbol{F}_c$). At each time step of the simulation, the contact force ($\boldsymbol{F}_c$) is defined as the resultant force of all the $\boldsymbol{f}_{c_i}$ forces. For the sake of computational efficiency of the simulation, a point search algorithm is developed using the techniques defining the intersection of two quadric surfaces [220]. Among all the $\boldsymbol{h}_i$ points constructing the humeral head surface, it provides at each time step a subset for which the penetration occurs. The contact model of Eq. 3.5 is smoothened using a continuous approximation of the heaviside function.

A smooth motion representing 150° abduction in the scapula plane is simulated. The motion is performed in 7.2 s. The Runge-Kutta-Fehlberg method [221], which combines a fourth and a fifth order Runge-Kutta scheme for error control is used to solve the

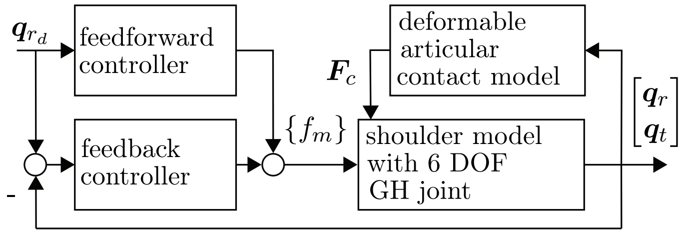

Figure 3.3: A block diagram representation of the developed framework. The contact force ($\boldsymbol{F}_c$) is defined by the deformable articular contact model. The muscle force magnitudes ($\{f_m\}$) are defined by the feedforward and the feedback controller such that the three rotational DOFs ($\boldsymbol{q}_r$) of the GH joint follow a given desired rotational trajectory ($\boldsymbol{q}_{r_d}$). The HHT is captured through the three translational DOFs ($\boldsymbol{q}_t$).

equations of motion.

The GH joint model with six DOFs is evaluated for the simulated motion within the developed framework. The results are presented in terms of the HHT relative to the glenoid, the GH joint contact force, the contact area, the contact pressure on the glenoid cartilage, and the maximum normal strain of the glenoid cartilage. They are also compared with the associated results from the literature wherever it is possible. The evolution of the HHT is resolved along with the arm abduction in three directions of a frame attached to the glenoid fossa, including inferior-superior, posterior-anterior, and lateral-medial. The glenoid frame is constructed from the scapula frame (Fig. 3.2) by two transformations. First, the scapula frame is shifted by $(r_g - r_h)$ in the negative direction of z_s to the origin of the glenoid frame. It is then rotated along y_s and x_s to account for the glenoid fossa orientation according to [119]. A similar GH joint model but with 3 DOF (ideal ball-and socket) is also simulated and its associated contact force is presented.

3.3 Results

The humeral head center translated relative to the glenoid frame from an inferior position superiorly until 90° abduction and then translated inferiorly (Fig. 3.4a). The range of inferior-superior HHT was around 2.5 mm. The humeral head center translated posteriorly from a central position and lied posteriorly throughout the simulated motion, whereas it translated anteriorly from 60° to 100° abduction (Fig. 3.4b). The range of posterior-anterior HHT was less than 0.5 mm. The humeral head center translated in the medial direction till 90° abduction and translated laterally afterward (Fig. 3.4c). The maximum HHT in the medial direction was less than 1.2 mm.

The GH joint contact force increased to 660 N (87% of the bodyweight) at 90° abduction and decreased afterward (Fig. 3.5). The difference between the contact forces predicted by the three DOF and the six DOF GH joint model was less than 6%.

The contact area increased initially by the abduction and decreased afterward (Fig. 3.6). The distribution of the contact pressure applied on the glenoid cartilage varied by the arm abduction (Fig. 3.6). The maximum contact pressure increased from 0.50 MPa at 30^o abduction by 130% at 90^o abduction and decreased thereafter to almost its initial amount by the end of the motion. Positions on the glenoid fossa where the maximum contact pressure was applied (center of pressure) from 30^o to 145^o of the arm abduction lied in the superior-posterior quarter of the fossa.

The maximum normal strain of the glenoid cartilage increased from 0% at 0^o abduction to almost 31% at 90^o abduction that was around 1.1 mm of the thickness of the deformable layer covering the glenoid fossa (Fig. 3.7). It decreased afterward to almost 24% until the end of arm abduction.

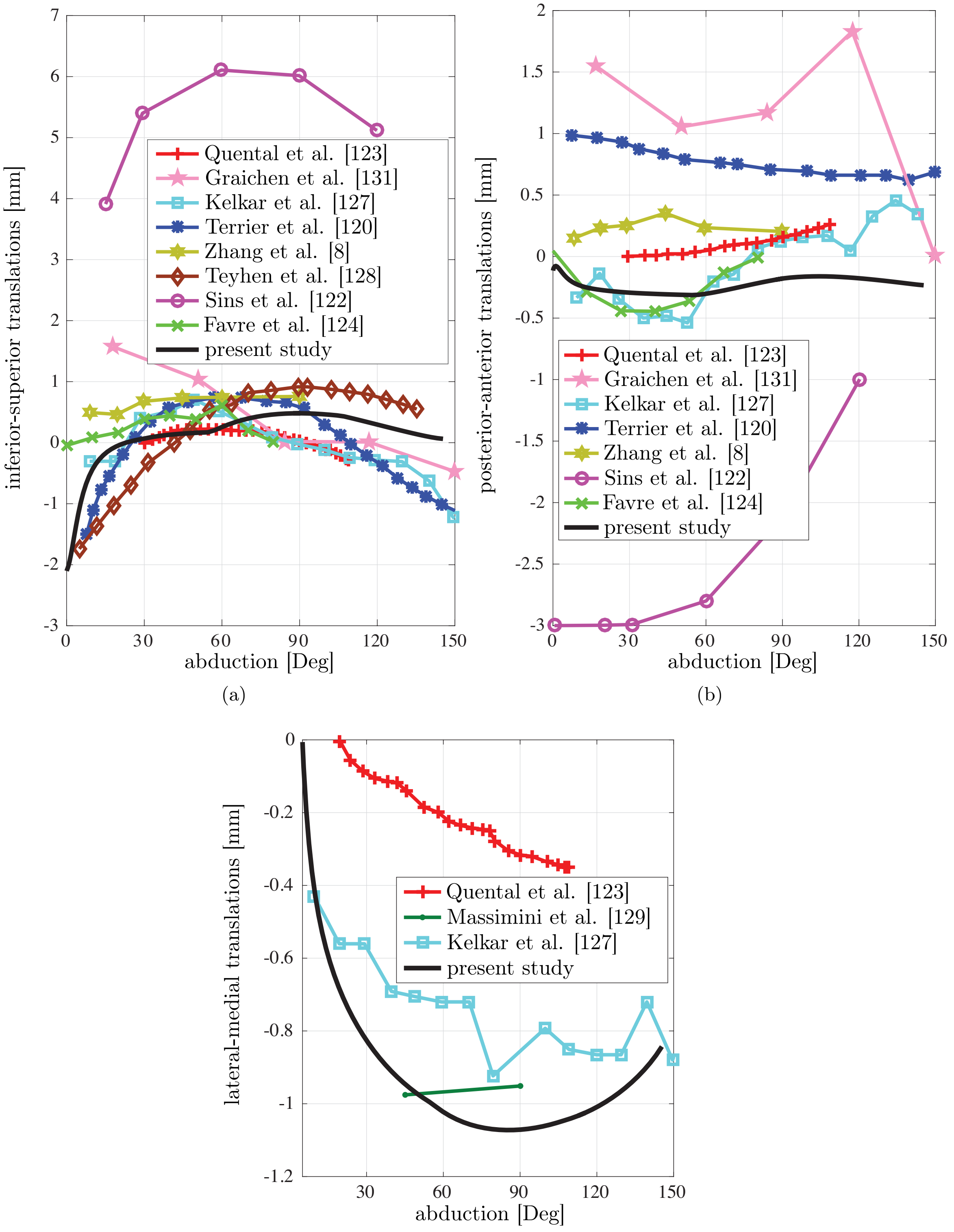

(a)

(b)

(c)

Figure 3.4: The HHT was resolved in three directions of the glenoid frame, namely inferior-superior (a), posterior-anterior (b), and lateral-medial (c). The associated results from the *in vitro* [127], *in vivo* [8, 128, 129, 131], and numerical [120, 122–124] studies were also shown.

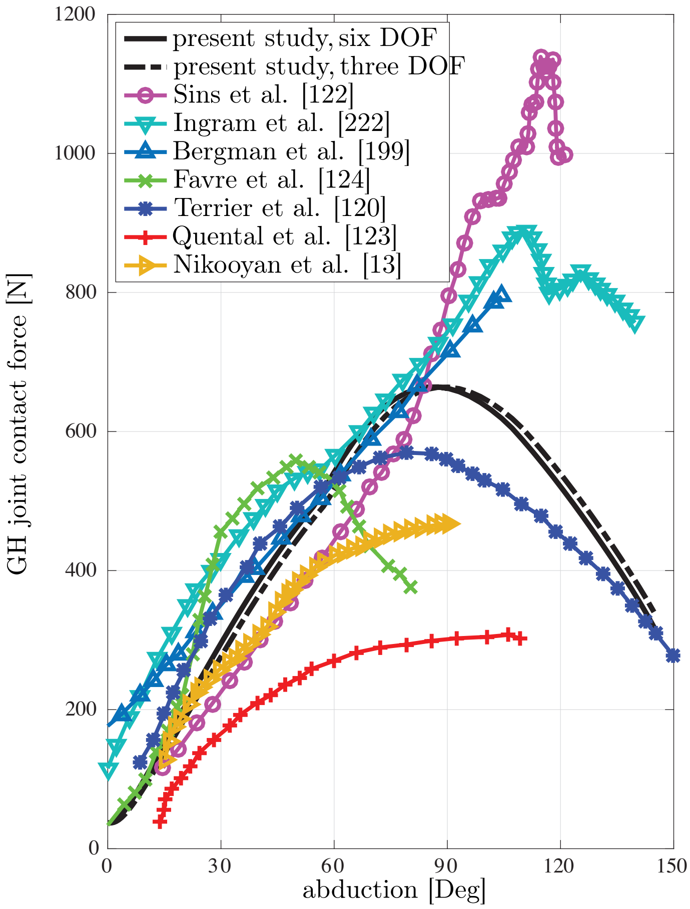

Figure 3.5: The GH joint contact force predicted by the present study and the associated results from numerical [13, 120, 122–124, 222] and *in vivo* studies [199]. The results predicted by a similar GH joint model but with three DOFs (ideal ball-and-socket) was also shown.

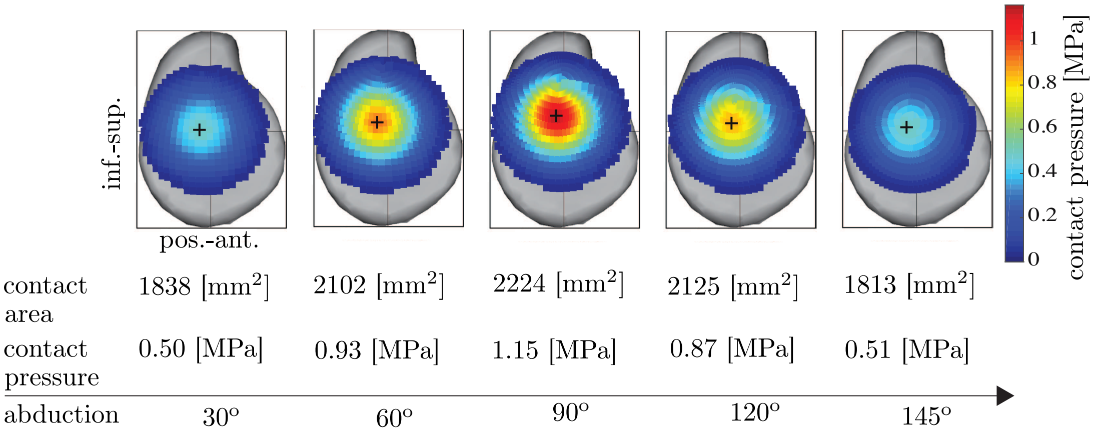

Figure 3.6: The distribution of the contact pressure applied on the glenoid cartilage and the contact area during the arm abduction. The results were shown for every 30° abduction. Positions on the glenoid fossa where the maximum contact pressure was applied (center of pressure) during the abduction were illustrated by black crosses.

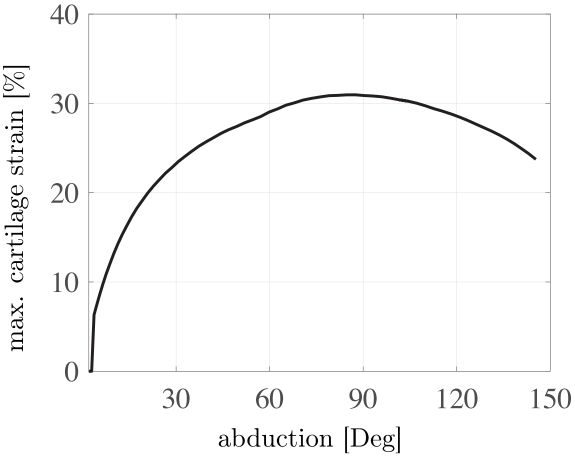

Figure 3.7: The maximum normal strain of the glenoid cartilage varied with the arm abduction.

3.4 Discussion

The aim of this study was to develop a framework that allowed forward-dynamics simulation of a shoulder model consisting of a GH joint with six DOFs associated to rotations and translations of the humerus in the glenoid fossa. The model thus provided the HHT during controlled elevation of the arm. We showed that a forward-dynamics framework addressing HHT required extra information about the glenohumeral contact. To that end, a deformable articular cartilage layer was included, providing a mapping from the generalized coordinates and velocities to the contact forces. The musculoskeletal model (framework) was tested and verified during a movement of abduction in the scapula plane. We specifically analyzed the HHT, the GH joint contact force, the contact area, the contact pressure, and the cartilage strain. These results were indirectly validated by comparison with *in vivo*, *in vitro*, and other numerical studies.

The initial inferior position of the humeral head center could be explained by the fact that the passive structures (ligaments, capsule, and labrum) surrounding the GH joint were lax when the joint was in its neutral configuration. Then until 30° abduction, the humeral head center experienced a superior translations that placed it in a rather central position. This was due to an upward pull by the muscles that has been already reported in [58, 67]. The upward pull was compensated by the contact force, producing a cartilage deformation (about 22% strain). After this first phase, the humeral head center remained in the superior-posterior quarter of the glenoid fossa.

A large variability of HHT was reported in the literature. Therefore, a rigorous validation of the HHT estimated by our framework was not possible. However, the trend of predicted inferior-superior HHT was consistent with the most commonly reported pattern ([120, 122, 123, 127, 128]). The range of translation also corresponded well with the literature ([128], [8], and [127]).

The predicted GH joint contact force was consistent with *in vivo* measurements [199] and the other numerical predictions [13, 120, 122, 222], at least up to 90° abduction. There was indeed less than 8% difference between our estimation of the contact force at 90° abduction than with measuremens of instrumented prostheses [199]. However, there was no clear consensus after 90° between the contact force estimated by the different studies mentioned. We indeed observed that contact pressure decreased after 90° abduction. Therefore, the contact force could be expected to exhibit the same descending behavior after 90° abduction.

The difference between the contact force predicted by the framework while considering a three DOF and a six DOF GH joint model was negligible for the simulated slow abduction motion. This supported the ideal ball-and-socket approximation of the GH joint for the force prediction applications. However, it should be noted that this difference could be more noticeable in case of simulation of a more dynamic motion. More specifically, this difference was caused by neglecting the linear acceleration of the humeral head center in the three DOF joint model. These linear accelerations resulted from the translational motion of the GH joint. Therefore, the faster these neglected translations were, the greater the difference between the contact force predicted by the three DOF and the six DOF GH joint model would be. The muscle force prediction of the three DOF model was already validated against EMG measurements in our previous work [223].

A discrepancy existed between the predicted contact area and *in vitro* measurements ([224, 225]). For instance, the predicted contact area was on average almost 2.8 and 4 times larger than the experimental measurements reported in [224] and [225], respectively. However, given the practical differences in the definition of contact between our approach and the *in vitro* studies, the observed discrepancy was expected. In our model, any infinitesimal surface on the humeral head with an infinitesimal penetration in the glenoid fossa was considered to be in contact. On the other hand, in the *in vitro* studies the definition of contact was subjected to the measurement precision. In a real joint, we could reasonably assume a full contact between the two deformable cartilage layers.

The predicted contact pressure was consistent with the literature, e.g. [124, 225]. For example, the maximum contact contact pressure predicted by our framework and the *in vitro* study in [225] at 60° was 0.93 MPa and 0.91 MPa, respectively. The predicted center of pressure in the superior-posterior quarter of the glenoid fossa was also consistent with the literature [122, 124, 128].

The application of forward-dynamics simulation together with the deformable articular contact model allowed us to solve the differential equations of motion of the GH joint with 6 DOF. Therefore, the dynamic effects of motion were naturally included in the translations predicted by our framework. Indeed, the first and second derivatives of the translational degrees of freedom were neglected in the previous studies (e.g. [119, 122, 124]) in order to transform the differential equations of motion to a set of algebraic equations.

The indeterminacy associated with the unknown contact force was resolved by incorporating a function mapping that defined the unknown contact force in terms of the joint kinematics. The function mapping was defined using a viscoelastic contact model. However, the necessity of incorporating a function mapping to resolve the indeterminacy should be distinguished from the methodology used to find this function mapping. In other words, a function mapping that defines the unknown contact force in terms of the joint kinematics is necessary to resolve the indeterminacy. However, there are several methodologies to define such a function mapping. For instance, given the viscoelastic characteristic of the *in vivo* GH joint, we used a viscoelastic contact model to define the associated function mapping. Whereas, one can consider an elastic contact model or a friction model to find an associated function mapping.

The developed framework included a multibody musculoskeletal model together with a representation of the cartilage contact mechanics. It therefore provided an integrated solution to study the relationship between joint kinematics, muscle forces, and cartilage stress. Indeed, the common approach in the literature consists of two steps. First a musculoskeletal model is used to define the rotational joint kinematics as well as the muscle forces. Then, a finite element analysis is performed to define the translational joint kinematics and the cartilage stress based on the results provided from the first step.

One of the limitations of the present study was that we focussed on the GH joint itself without considering the effect of the adjacent bones. Future development should therefore incorporate a large-scale model of the shoulder into the framework. The second limitation referred to the spherical approximation of the humeral head. However, it is straightforward to integrate more realistic anatomical geometries in the developed framework. The third limitation was associated with neglecting the GH joint passive structures (ligaments, capsule, and labrum) in the evaluated shoulder model. However, given that they are lax except for the extreme positions of the joint [67], their contribution for the simulated motion was expected to be negligible. Furthermore, to simulate motions involving the joint extreme positions, inclusion of these passive structures in the framework is necessary. To that end, a model of the passive structures defining their associated force as a function of joint kinematics (e.g. see [226]), would be integrated in the framework in our future developments. Another limitation was related to the fact that the articular contact was approximated as a rigid-to-deformable contact (rigid humeral head in contact with the deformable glenoid fossa). It simplified the formulation of the contact problem provided that the deformation of one contacting component was only involved. However, this deviated from the more complex deformable-to-deformable contact of the *in vivo* GH joint.

In conclusion, we developed a framework based on a joint application of a forward-dynamics simulation and a deformable articular contact to simulate a human shoulder model including a six DOF GH joint model. It not only provided estimations of muscle and joint reaction forces (similar to three DOF GH joint models) but also allowed estimations of HHT, contact areas, and contact pressure. The latter is required to broaden our understanding of the GH joint stability and more crucially to design shoulder prostheses. This novel framework had three main advantages. First, given that the dynamic equations of motion were solved forward in time, the dynamic effects of motion were naturally considered despite the previous numerical [119, 121, 122, 124, 125] and *in vivo* [8, 129, 131] studies. Second, a nonlinear viscoelastic approximation was used for the articular contact. Third, it provided an integrated solution for the study of the GH joint function that dealt simultaneously with the joint kinematics and mechanics. The results were in a good agreement with the ones from the literature. In a next step, the proposed framework could be populated with subject-specific morphological data to account for effects of inter-individual anatomical variabilities on GH joint functions during ADL. The proposed methodology could also be translated for clinical applications related to the treatment of osteoarthritis by TSA. Furthermore, outcomes of the proposed simulation framework could be applied for biomechanical analysis and design of available and forthcoming shoulder prostheses.

4 Motion reconstruction in upper extremity in the absence of scapula kinematics measurement-devices

This chapter is a preprint version of the following self-authored article that has been submitted to Journal of Biomechanics.

Ehsan Sarshari, Matteo Mancuso, Alexandre Terrier, Alain Farron, Philippe Mullhaupt, Dominique Pioletti, "Motion reconstruction in upper extremity in the absence of scapula kinematics measurement-devices", BM-D-18-00419, 2018.

Abstract

Videogrammetry systems are commonly used for recording upper extremity motions. They measure trajectories of skin-fixed markers that are placed on their associated palpable bony landmarks. The glenohumeral joint center (GH) is not a palpable bony landmark. Therefore, it cannot be tracked by videogrammetry systems. But, the GH is required for reconstructing the motions. Hence, it is commonly estimated by separately measuring scapula motions using scapula kinematics measurement-devices (SKMD). Applications of SKMD are neither straightforward nor always noninvasive. Therefore, this study aims at reconstructing videogrammetry-based measured motions of the upper extremity in the absence of SKMD. To this end, a method is proposed estimating the GH using trajectories of few markers and an MRI scan of an understudy subject's glenohumeral joint. Two scenarios are considered to evaluate the method. In scenario 1, a numerical method is used to conceptually generate markers trajectories including the GH, during an arm flexion. The generated GH is considered as the actual GH and is intentionally excluded from the trajectories. The method is then used to estimate it. In scenario 2, an arm abduction is measured using a videogrammetry system. It is reconstructed using multi-segment optimization after estimating GH. The results are presented for the scenario 1 in terms of the distance and normalized root mean square errors (NRMSE) of the estimated GH with respect to the actual GH, and for the scenario 2 as the reconstructed joints angles and their NRMSE with respect to *in vivo* studies. The estimated GH stays within 5 mm distance to the actual GH. Also, the reconstructed joint angles have excellent agreements with the *in vivo* studies (e.g. NRMSE of scapular posterior/anterior tilt$>$ 0.91).

4.1 Introduction

Accurate estimations of upper extremity kinematics are essential. Because, they are correlated to upper extremity pathologies [138, 139]. They can also alter force predictions obtained using inverse dynamics [49].

Videogrammetry systems are extensively used for noninvasive measurements of upper extremity kinematics [91]. They track trajectories of skin-fixed markers. These markers are placed on palpable bony landmarks used to define configurations of each bone segment in a kinematic model. The markers trajectories are subject to relative movements of the skin with respect to their underlying bony landmarks (soft tissue artifacts) [140]. For instance, up to 48% of the humeral axial rotation was shown to be influenced by soft tissue artifacts [141]. Therefore, a so-called multi-segment optimization is used to exclude the effects of soft tissue artifacts [74, 142]. It reconstructs a measured motion by minimizing the overall distance between all the measured markers and the model bony landmarks [50]. The evaluation of the overall distance requires a one-to-one association between the bony landmarks and the measured markers. However, it is not possible to palpate and measure the GH. Because, the GH is a conceptual bony landmark defined as the center of a sphere approximating the humeral head [143].

Several methods have been developed to estimate the GH. They can be broadly divided into two categories, namely formal methods [144–149] and predictive methods [150–153]. The formal methods estimate the GH by finding either the closet point to all the instantaneous helical axes of the humerus [144–147] or the center of a sphere passing through humerus markers [148, 149]. The predictive methods provide estimations of the GH either through regressive equations between scapula markers and the GH [150–152] or generic offsets from one of scapula markers [152, 153]. The formal methods provide more accurate GH estimations and are preferred over predictive methods whose accuracy drops significantly during arm motions [147, 152]. Given that the predictive methods are based on anthropometry studies, they fall short of replicating inter-individual differences [152]. The main limitation of the formal methods is their dependency on SKMD. A majority of the predictive methods also require SKMD, otherwise their estimations are impractical (±5 cm error) [153].

Scapula motions cannot be adequately measured by videogrammetry systems [154]. Because, among its four palpable bony landmarks, trigonum scapulae (TS) and angulus inferior (AI) are heavily masked by soft tissues [155, 156], and only angulus acromialis (AA) and acromioclavicular (AC) can be practically tracked. Hence, SKMD are alternatively used to measure its motions. An intracortical bone-fixed pin drilled into scapula was introduced [157]. It was invasive and compromised the motion by causing pain. Regressive equations were also derived providing estimations of scapula kinematics based on the thoracohumeral joint angles [45, 46, 158–161]. But, information of the thoracohumeral joint angles required *a priori* knowledge of the GH. Their accuracy was also limited to small ranges of motion. Manual palpation of the scapula surface and application of a so-called scapula locator fixture were proposed in [162, 163] and [164, 165], respectively. But, they are neither time efficient nor practical during arm motions [166]. A marker tree including three markers was fixed to the acromion to track the scapula [167]. However, this so-called acromion marker cluster tended to move medially with the skin during abduction [168] and was very sensitive to its initial placements [169].

Therefore, the aim of this study is to reconstruct a videogrammetry-based measured motion of the upper extremity including scapula in the absence of SKMD. To this end, a method for estimating the GH and consequently TS and AI is developed. The method is evaluated through two scenarios. Scenario 1 is purely numerical with no measurements involved. The accuracy of the method estimations for the GH are evaluated by their distance and NRMSE relative to conceptually generated GH. In scenario 2, the method is used to estimate the missing GH, TS, and AI for a measured motion by a VICON videogrammetry system. Multi-segment optimization is then used to reconstruct the motion in terms of joints angles. Given the importance of the scapula kinematics [49], the estimated acromiclavicular joint angles are presented together with their *in vivo* measurements from [138, 139].

4.2 Methods

A kinematic model is developed for the upper extremity based on 14 bony landmarks (Section 4.2.1). The VICON videogrammetry system is used to measure trajectories of 11 skin-fixed markers during an abduction motion (Section 4.2.2). No SKMD is used, and instead a method is developed to estimate GH, TS, and AI (Section 4.2.3). An optimization routine is included in the method to compensate the effects of soft tissue artifacts on GH estimations. Multi-segment optimization is used to reconstruct the measured motion that is completed by the estimated landmarks (Section 4.2.4). Finally, two scenarios are presented for evaluating the method (Section 4.2.5). In scenario 1, no measurement is involved. A numerical method from [100] is adapted to conceptually generate markers trajectories for an arm flexion. Soft tissue artifacts are numerically replicated and added to the data. Our method is used to estimate the GH, while it is excluded from the data and is kept for evaluating the estimations. A predictive method from [152] is also used to estimate the GH for the same trajectories. In scenario 2, the measured motion of Section 4.2.2 is reconstructed in terms of joint angles. A first order approximation [227] is used to approximate sensitivities of the estimated joint angles to variations in the measured data caused by soft tissue artifacts.

4.2.1 Kinematic model

A kinematic model of the upper extremity is developed from MRI scans of the right shoulder of a healthy male subject (29 year, 186 cm, and 85.5 kg) (Fig. 4.1a). It consists of six rigid bodies including thorax, clavicle, scapula, humerus, ulna, and radius that is rigidly tied with hand. It has nine DOFs attributing to three ball-and-socket joints including sternoclavicular (SC), acromioclavicular (AC), and glenohumeral (GH) joints and two hinge joints associating with humeroulnar (HU) and radioulnar (RU) joints and two holonomic constraints (Fig. 4.1b,c). The constraints restrict TS and AI on the scapula medial boarder to glide over the ribcage. At least three non-collinear points (bony landmarks) are considered to define configurations of each bone segment, except for the clavicle that only two bony landmarks can be discerned. Three bony landmarks on the humerus including medial epicondyle (EM), lateral epicondyle (EL), and their middle point are borrowed for the ulna and the radius. Six bone-fixed frames are considered for each of the bone segments following the ISB recommendations [201], with the thorax being the inertial frame. However, the ISB recommendation results in non-physiological configurations of forearm relative to humerus [202]. Therefore, reference configurations are introduced based on the MRI scans that despite the ISB recommendations do not require alignments of the ulna and radius frames with respect to their proximal bones. The joints coordinates are also considered according to ISB recommendations. An Euler angle sequence of $X-Y-Z$ is considered for the SC and AC joints, whereas $Z-Y-Z$ is used for the GH joint. Eleven generalized coordinates ($\boldsymbol{q} = [q_1 \ \dots \ q_{11}]^T$) are considered to uniquely define each joint configuration. The forward kinematics map (ξ) associated to the developed kinematics model defines the coordinate of the j^{th} bony landmark ($\boldsymbol{x}_j$) for a given joint configuration (Eq. 4.1).

$$\begin{aligned}
&\xi : C_s \subset R^{11} \mapsto W_s \subset R^3 \\
&\xi(\boldsymbol{q}(t)) = \boldsymbol{x}_j(t), \quad j = \{\text{C7},\ \ldots,\ \text{RS}\}_{1\times 14} \\
&\Phi_{\text{TS}}(\boldsymbol{q}(t)) = 0 \\
&\Phi_{\text{AI}}(\boldsymbol{q}(t)) = 0
\end{aligned} \tag{4.1}$$

Where, C_s and W_s are the coordinate space and work space of the upper extremity [228]. Two holonomic constraints ($\Phi_{\text{TS}} = 0$ and $\Phi_{\text{AI}} = 0$) are also considered to account for the kinematic relationships between the scapula and the thorax (Eq. 4.2). They constrain TS and AI to lie on ellipsoids approximating the ribcage and their underlying soft tissues.

$$\begin{aligned}
\Phi_{\text{TS}}(\boldsymbol{q}(t)) &= ({}_t\boldsymbol{TS}(t) - {}_t\boldsymbol{e}_0)^T E_{\text{TS}}({}_t\boldsymbol{TS}(t) - {}_t\boldsymbol{e}_0) - 1 = 0 \\
\Phi_{\text{AI}}(\boldsymbol{q}(t)) &= ({}_t\boldsymbol{AI}(t) - {}_t\boldsymbol{e}_0)^T E_{\text{AI}}({}_t\boldsymbol{AI}(t) - {}_t\boldsymbol{e}_0) - 1 = 0
\end{aligned} \tag{4.2}$$

Where, the left-hand side subscript t denotes that the landmarks are in the thorax frame. The ellipsoids center is ${}_t\boldsymbol{e}_0$, and E_{TS} and E_{AI} are the matrices corresponding to each of the ellipsoids [229].

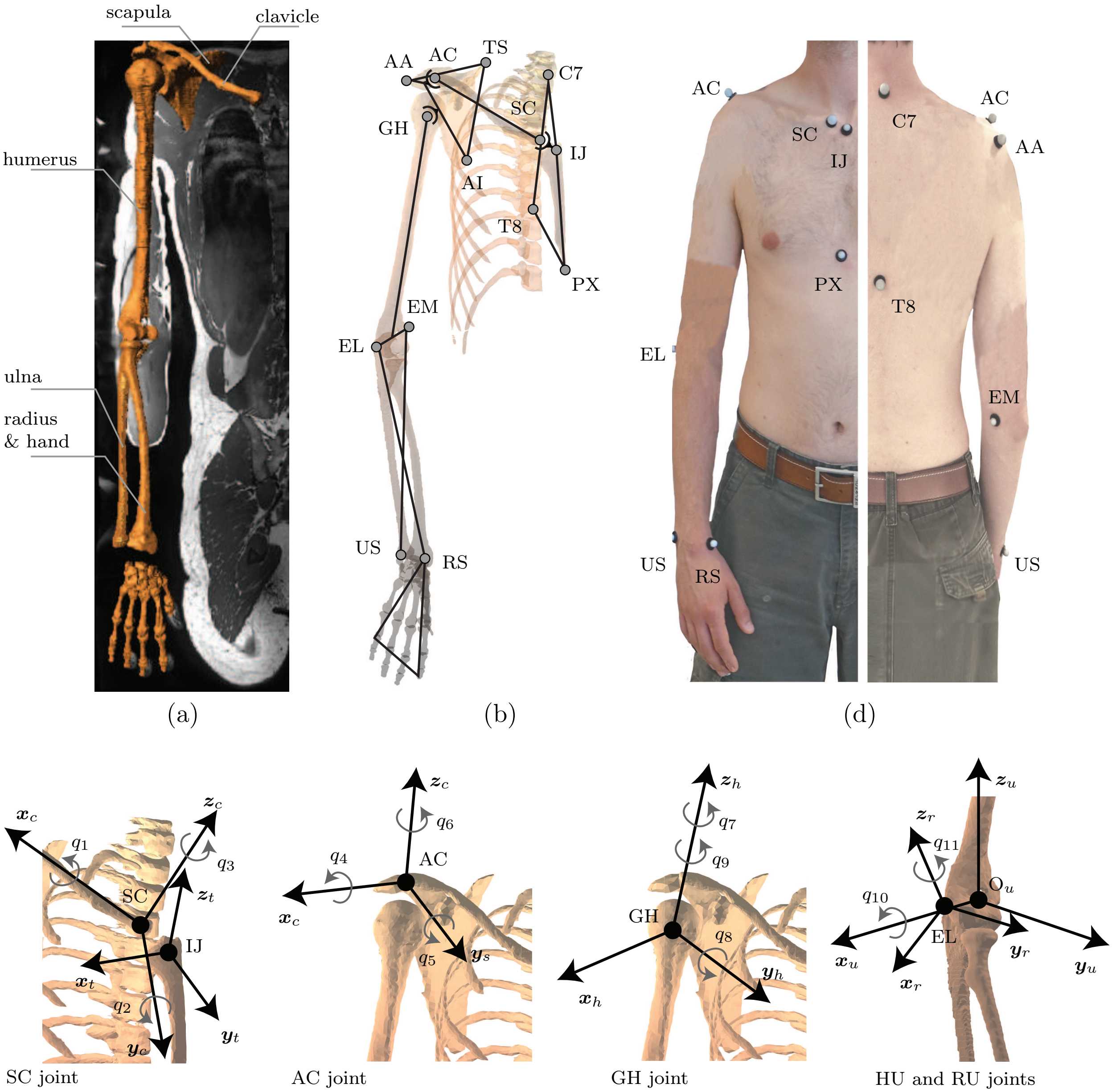

(a) (b) (d)

SC joint
q_1: axial rotation
q_2: depression/elevation
q_3: protraction/retroaction

AC joint
q_4: posterior/anterior tilt
q_5: downward/upward rotation
q_6: protraction/retroaction

GH joint
q_7: axial rotation
q_8: addcuction/abduction
q_9: flexion/extension

HU and RU joints
q_{10}: extension/flexion
q_{11}: pronation/supination
$O_u = {}^{EL + EM}/_{2}$

(c)

Figure 4.1: (a) An MRI scan of a healthy male subject is used to developed a kinematic model of the upper-extremity. It consists of six rigid bodies, including thorax, clavicle, scapula, humerus, ulna, and radius together with hand. (b) At least three bony landmarks are considered in the kinematics model for each bone segments (14 bony landmarks in total), except for clavicle that only 2 bony landmarks (SC and AC) can be discerned. Bony landmarks from the proximal bone segments are used for both ulna and radius. (c) The nine DOFs of the model attribute to 11 joint angles of SC, AC, GH, HU, and RU joints and 2 constraints associated with relative movements of scapula with respect to thorax. Eleven generalized coordinates are therefore considered ($\boldsymbol{q} = [q1 \ \ldots \ q_{11}]^T$) to span the joint space of the model. (d) The bony landmarks TS, AI, and GH are not practically palpable. VICON videogrammetry system is used to track the trajectories of the skin-fixed markers placed on their associated palpable bony landmarks.

4.2.2 Measurements

Eleven palpable bony landmarks are palpated using skin-fixed markers on the same subject, including incisura jugularis (IJ), processus xiphoideus (PX), 7th cervical vertebra (C7), 8th thoracic vertebra (T8), SC, AC, AA, EM, EL, radial styloid (RS), and ulnar styloid (US) (Fig. 4.1d). The markers trajectories are recorded using an 8-camera VICON videogrammetry system (VICON, UK) at 100 Hz sampling frequency. They are captured while the subject performs an abduction motion in the scapula plane with a fully extended forearm. The abduction motion is repeated for 10 trials with an average speed of 2.4 s/trial (0.42 Hz).

The recorded data is partitioned for each trial and is low-passed filtered using an 8 order zero-phase Butterworth filter. The cut-off frequency of the filter is obtained through residual analysis of the data and is cross checked with associated values from harmonic analysis [91]. Then, the means and standard deviations (σ) of the filtered trajectories corresponding to the 10 trials are obtained.

4.2.3 Estimation of GH, TS, and AI

The overall distance of the multi-segment optimization cannot be evaluated, except estimations of the missing landmarks GH, TS, and AI are provided. This section presents our method to estimate the GH for given trajectories of AC, AA, EM, and EL. Build on the resulting estimations for the GH, estimations for TS and AI are also obtained.

The ball-and-socket approximation of the glenohumeral joint implies that the GH is a point shared between the scapula and the humerus (Fig. 4.2). Therefore, its positions as a point either on the scapula or on the humerus should result in the same point in the thorax frame. This can be concisely written as

$$ {}^{t}_{h}R(\alpha)\ {}_{h}\mathbf{GH} + {}_{t}\mathbf{EM} = {}^{t}_{s}R(\beta)\ {}_{s}\mathbf{GH} + {}_{t}\mathbf{AC} \tag{4.3} $$

Where, ${}^{t}_{h}R(\alpha)$ and ${}^{t}_{s}R(\beta)$ are rotation matrices from the humerus and the scapula frames to the thorax frame. They are defined in Eq. 4.4 using Rodrigues' rotation formula [11]. The left-hand side subscripts h and s specify that the landmarks are in the humerus and the scapula frames, respectively. The ${}_{h}\mathbf{GH}$ and ${}_{s}\mathbf{GH}$ are constant quantities and are obtained from an MRI scan of the understudy subject's glenohumeral joint.

$$ \begin{aligned} {}^{t}_{h}R(\alpha) &= \boldsymbol{d}_h\boldsymbol{d}_h{}^{T} + \cos\alpha(I - \boldsymbol{d}_h\boldsymbol{d}_h{}^{T}) + \sin\alpha[\boldsymbol{d}_h] \\ {}^{t}_{s}R(\beta) &= \boldsymbol{d}_s\boldsymbol{d}_s{}^{T} + \cos\beta(I - \boldsymbol{d}_s\boldsymbol{d}_s{}^{T}) + \sin\beta[\boldsymbol{d}_s] \end{aligned} \tag{4.4} $$

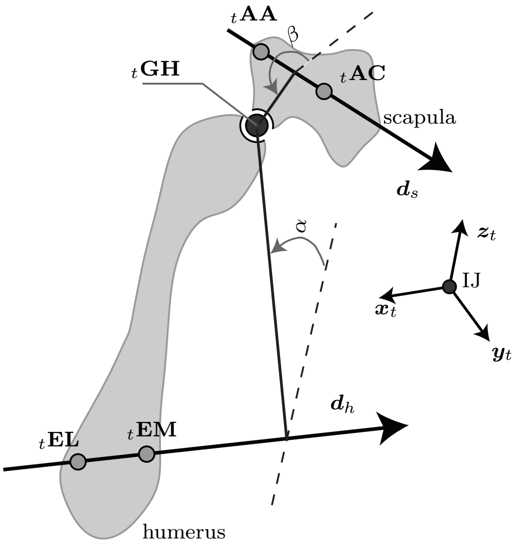

Figure 4.2: Given that the bone segments are assumed to be rigid, the ball-and-socket approximation of the glenohumeral joint implies that GH belongs to both humerus and scapula. The proposed method provides estimations of the GH in the thorax frame ($_t\mathbf{GH}$) for given positions of AC, AA, EM, and EL markers ($_t\mathbf{AC}$, $_t\mathbf{AA}$, $_t\mathbf{EM}$, and $_t\mathbf{EL}$). The left hand-side subscripts t denotes that the landmarks are expressed in the thorax frame. The estimated $_t\mathbf{GH}$ lies on the intersection of two line segments in planes perpendicular to $\boldsymbol{d}_h$ and $\boldsymbol{d}_s$. These two line segments form two angles (α and β) with respect to reference axes in their associated planes. The resulting angles can be found by solving Eq. 4.3.

Where, $\boldsymbol{d}_h = {}_t\mathbf{EM} - {}_t\mathbf{EL}$ and $\boldsymbol{d}_s = {}_t\mathbf{AC} - {}_t\mathbf{AA}$, and α and β are the unknown rotation angles of the humerus and the scapula around $\boldsymbol{d}_h$ and $\boldsymbol{d}_s$. The cross product matrices corresponding to $\boldsymbol{d}_h$ and $\boldsymbol{d}_s$ are denoted by $[\boldsymbol{d}_h]$ and $[\boldsymbol{d}_s]$, respectively.

Equation 4.3 can be solved for α and β for each frame of measurement data using a nonlinear root search method (for instance `fminsearch` of Matlab). Each of the resulting α and β provides an estimation for the GH in the thorax frame ($_t\mathbf{GH}$). The resulting two estimations are coincide within the accuracy of the root search method, if the relative positions of the AA with respect to AC and EM with respect to EL do not change. However, given that the measured positions of AC, AA, EM, and EL are subject to soft tissue artifacts, the resulting two estimations of $_t\mathbf{GH}$ will come apart. More specifically, the tangential movements of EM and EL along the longitudinal axis of humerus due to soft tissue artifacts [168] can split up the resulting two estimations. Therefore, the following optimization is casted to minimize the distance between the resulting two estimations by compensating the effects of soft tissue artifacts on EM and EL positions.

$$\begin{aligned} \min_{\boldsymbol{\mu}}. \quad & \left({}_t\mathbf{GH}_{e_h}(\alpha, \boldsymbol{\mu}) - {}_t\mathbf{GH}_{e_s}(\beta)\right)^2 \\ \text{s.t.} \quad & |\boldsymbol{\mu}| \leq C \end{aligned} \tag{4.5}$$

Where, ${}_t\mathbf{GH}_{e_h}$ and ${}_t\mathbf{GH}_{e_s}$ are the resulting estimations obtained through the humerus and the scapula frames, respectively. The decision variable $\boldsymbol{\mu}$ is a 3×1 vector that adds to $\boldsymbol{d}_h$ in order to compensate soft tissue artifacts on EM and EL. It is bounded also by C to vary in accordance with the reported values for EM and EL soft tissue artifacts ($C = 3$ cm is used here according to [168]).

The estimated GH together with the measured AC and AA provide three points on the scapula. Therefore, the TS and the AI are readily estimated, given that they also belong to the same bone segment.

It is worth noting that Eq. 4.3 has an intuitive geometrical interpretation. In fact, it estimates GH by intersecting four spheres centered at AC, AA, EM, and EL. Their radii can be defined from a single MRI scan of the glenohumeral joint of the understudy subject. This intersection can be defined using the intersection theory of quadric surfaces [229].

4.2.4 Multi-segment optimization

The multi-segment optimization defines the joint angles ($\boldsymbol{q}_i$) for each frame of the measured data (i) such that the overall distance between the measured markers ($\boldsymbol{x}_{e_j}$) and their associating bony landmarks ($\boldsymbol{x}_{m_j}$) is minimized, while satisfying the forward kinematics map (Eq. 4.6). For GH, TS, and AI their estimations are considered on behalf of their missing measured trajectories.

$$\begin{aligned}
\min_{\boldsymbol{q}_i} . \quad & \textstyle\sum_j (\boldsymbol{x}_{m_{j,i}}(\boldsymbol{q}_i) - \boldsymbol{x}_{e_{j,i}})^T W (\boldsymbol{x}_{m_{j,i}}(\boldsymbol{q}_i) - \boldsymbol{x}_{e_{j,i}}) \\
\text{s.t.} \quad & \Phi_{\mathrm{TS}}(\boldsymbol{q}_i) = 0 \\
& \Phi_{\mathrm{AI}}(\boldsymbol{q}_i) = 0
\end{aligned} \tag{4.6}$$

Where, $j = \{\mathrm{C7}, \ \ldots, \ \mathrm{RS}\}_{1\times 14}$, and W is a positive definite weighting matrix. This optimization is a nonlinear programming problem [230] that can be solved using iterative numerical methods for each i upon providing a viable initial guess for the $\boldsymbol{q}_i$. The function `fmincon` of Matlab is used in this study, while $\boldsymbol{q}_{i=1} = \mathbf{0}$ is considered for the first data frame and the resulting $\boldsymbol{q}_{i-1}$ is used as an initial guess for finding $\boldsymbol{q}_i$.

4.2.5 Evaluation scenarios

Two scenarios are considered to evaluate the method. The scenario 1 is purely numerical with no measurements involved. The scenario 2 uses the measured trajectories of Section 4.2.2.

Scenario 1: A numerical method from [100] is used to conceptually generate trajectories. They are associated to all the 14 bony landmarks during an arm forward flexion. The GH is excluded from them and considered as the actual GH (${}_t\boldsymbol{GH}_a$). Soft tissue artifacts are numerically generated according to [231, 232] and added to the resulting trajectories. They are defined as $a \sin \omega t + \phi$, where a lies between 1 cm to 3 cm, and ω and ϕ are set to be smaller than 4 Hz and 2π, respectively. The resulting trajectories are considered as pseudo-measurement data. The method is used to estimate the GH from AC, AA, EM, and EL of the pseudo-measurement data.

Furthermore, a predictive method introduced in [152] is also used to estimate the GH from the same pseudo-measurement data. It does not require SKMD either and estimates the GH based on offset equations in terms of AC, AA, IJ, and C7.

The results are presented in terms of the distance between the estimated GH positions (${}_t\boldsymbol{GH}_e$) and ${}_t\boldsymbol{GH}_a$, i.e. $|{}_t\boldsymbol{GH}_a - {}_t\boldsymbol{GH}_e|$. NRMSE of the ${}_t\boldsymbol{GH}_e$ with respect to ${}_t\boldsymbol{GH}_a$ is also calculated (Eq. 4.7) and presented.

$$\mathrm{NRMSE}_k = 1 - \frac{|{}_t\boldsymbol{GH}_{a_k} - {}_t\boldsymbol{GH}_{e_k}|}{|{}_t\boldsymbol{GH}_{a_k} - \mathrm{mean}({}_t\boldsymbol{GH}_{a_k})|} \tag{4.7}$$

Where, the index k denotes each data frame of the pseudo-measurement data. NRMSE varies from $-\infty$ to 1, and NRMSE$=1$ denotes a perfect estimation.

Scenario 2: Our proposed method is used to estimate GH, TS, and AI from the measured abduction motion. Then, multi-segment optimization is used to reconstruct the motion in terms of joints angles.

Sensitivities of the resulting joint angles ($\boldsymbol{q}(\Delta\boldsymbol{x})$) to variations in the measured trajectories around their means ($\Delta\boldsymbol{x}$) are also approximated. To this end, a first order approximation is used (Eq. 4.8) [227].

$$\boldsymbol{q}(\Delta\boldsymbol{x}) = \boldsymbol{q}^\star + M^{-1}N\Delta\boldsymbol{x} + O(|\Delta\boldsymbol{x}|) \tag{4.8}$$

Where, $\boldsymbol{q}^\star$ is the solution of the multi-segment optimization associated with the means of the measurements. The matrices M and N are defined as follows.

$$M = \begin{bmatrix} \nabla^2 L & \nabla\Phi_{\mathrm{TS}} & \nabla\Phi_{\mathrm{AI}} \\ \nabla\Phi_{\mathrm{TS}} & 0 & 0 \\ \nabla\Phi_{\mathrm{AI}} & 0 & 0 \end{bmatrix} \quad , \quad N = \begin{bmatrix} -\frac{\partial}{\partial\Delta\boldsymbol{x}}(\nabla L) & -\frac{\partial\Phi_{\mathrm{TS}}}{\partial\Delta\boldsymbol{x}} & -\frac{\partial\Phi_{\mathrm{AI}}}{\partial\Delta\boldsymbol{x}} \end{bmatrix}^T \tag{4.9}$$

Where, L is the Lagrangian of multi-segment optimization (Eq. 4.6).

The results are presented in terms of the 11 joints angles. They consist of SC joint angles including axial rotation, depression/elevation, and protraction/retraction, AC joint angles including posterior/anterior tilt, downward/upward rotation, and protraction/retroaction, GH joint angles including axial rotation, adduction/abduction, and flexion/extension, HU joint extension/flexion, and RU joint pronation/supination. Given the importance of the scapula kinematics, the AC joint angles from *in vivo* measurements of [138, 139] are also presented. The angles sensitivities to $\pm 1\sigma$ variations of the markers trajectories around their means are also illustrated. The joints angles are presented with respect to the thorax frame, except for the HU and the RU angles that are given with respect to their proximal joints. All the joints angles are shown along the arm abduction angle.

4.3 Results

Scenario 1: The distance of ${}_t\boldsymbol{GH}_e$ to ${}_t\boldsymbol{GH}_a$ stayed at almost 0 mm until 20% of the arm flexion (Fig. 4.3a). It increased to 5 mm at the end of the motion. The NRMSE also showed a perfect estimation for the beginning of the motion (NRMSE ≈ 1). It dropped to around 0.96 at the end of the arm flexion (Fig. 4.3b).

Scenario 2: Nonzero angles were estimated for all the joint angles, except for the axial rotation of the SC joint (Fig. 4.4).

SC joint motion: The estimated motion of the SC joint was characterized by an increase of 16° and 26° in clavicular elevation and retraction from 28° to 45°, and 13° to 39° during the arm elevation, respectively. They were equally affected by variations in the landmarks trajectories (about 13°).

AC joint motion: The scapular posterior tilt increased by 5° from an anteriorly tilted configuration of -11° to -6°. The scapular upward rotation increased from a neutral position of 0° by 30°. The scapular protraction decreased by 7° from 26° to 19°. The sensitivity of scapular angles to variations in the landmarks trajectories were 5°, 13°, and 6° for posterior/anterior tilt, downward/upward rotation, and protraction/retraction angles, respectively.

GH joint motion: The humerus rotated externally by 49° from an internally orientated configuration of 19° to -30°. It abducted 68° from -30° to -98°. The humeral flexion angle increased by 30° from 1°. The humeral axial rotation and adduction/abduction angles were more sensitive to the variations in landmarks trajectories comparing to that of flexion/extension angle (equally 14° that is almost 250% more).

Elbow motion: The forearm flexed 6° from a fully extended configuration (0° flexion). The radioulnar supination increased by 9° from -51° (the palm of the hand faced

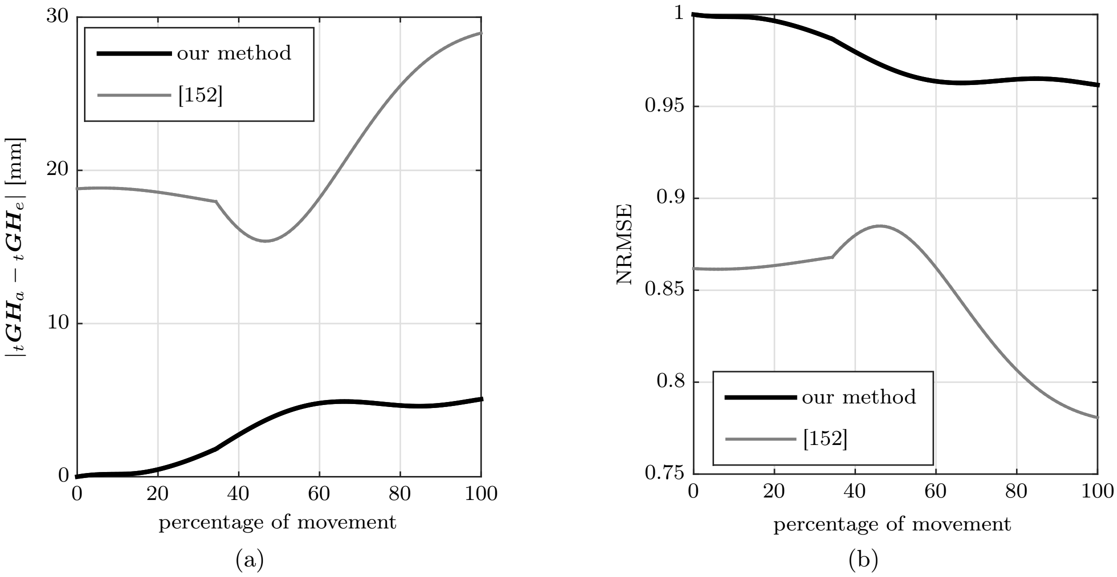

Figure 4.3: Scenario 1, (a) distance of the estimated GH to its actual position, (b) NRMSE of the estimated GH with respect to its actual position, during arm flexion. The GH estimations from predictive method of [152] were also presented.

anteriorly) to -60°. Forearm angles had the highest sensitivities to variations in the landmarks trajectories comparing to all the other joint angles (17° and 22° for HU and RU, respectively).

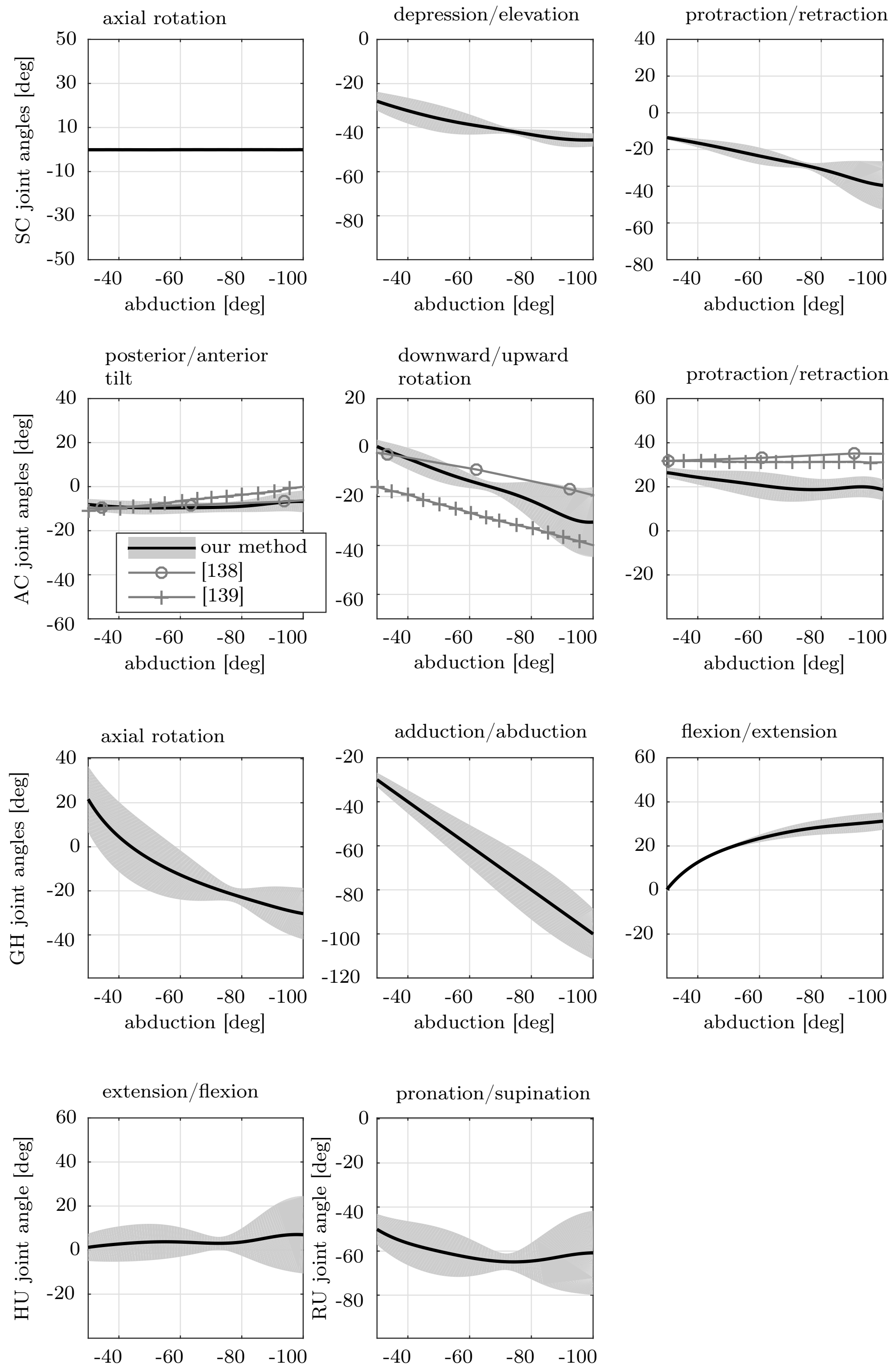

Figure 4.4: Scenario 2. The measured abduction motion in the scapula plane was reconstructed in terms of the 11 joint angles of the upper extremity. The angles sensitivities to ±1σ variations in the landmarks trajectories around their means were presented as the shaded area. The AC joint angles measured *in vivo* by [138, 139] were also presented, given the importance of the scapula kinematics.

4.4 Discussion

The aim of this study was to reconstruct a videogrammetry-based measured motion of the upper extremity in the absence of SKMD. To this end, a kinematic model of the upper extremity was developed. Trajectories of skin-fixed markers during an arm abduction were measured using VICON videogrammetry system. Trajectories of GH, TS, and AI were missing from the measured trajectories. Because, GH was not palpable. Both TS and AI were masked with thick layers of soft tissues and were not practically trackable. Therefore, a method was proposed to estimate GH, TS, and AI. It could compensate for the soft tissue artifacts. Two scenarios were considered to evaluate the method. In the scenario 1, our method was used to estimate the GH for pseudo-measurements data associated with an arm flexion. In the scenario 2, build on the resulting estimations for GH, TS, and AI, the multi-segment optimization was used to reconstruct the measured motion. We evaluated for the scenario 1 the accuracy of the GH estimations. For the scenario 2, we analyzed the upper extremity joints angles, including 11 joint angles of the SC, the AC, the GH, the HU, and the RU joints. The resulting AC joint angles were also compared to the *in vivo* measurements.

For the scenario 1, our method provided accurate estimations for the GH. They stayed within less than 5 mm distance to the actual GH throughout the motion. Their NRMSE decreased from 1 to almost 0.96, illustrating less accurate estimations toward the end of motion. This could be associated to the increase in the simulated soft tissue artifacts. The increasing trend considered for soft tissue artifacts was consistent with previous *in vivo* observations [231, 232].

The predictive method introduced in [152] was also used. Its GH estimations were at least 290% further apart comparing to our method. For the sake of a fair comparison, it is worth mentioning that our method required an MRI scan of the understudy subject. This is not the case for predictive methods developed for GH. However, their development relied on an extensive data set of cadaveric studies.

For the scenario 2, the reconstructed joints angles were consistent with the *in vivo* [138, 139] and previous numerical [49, 233] studies. However, the model overlooked the clavicular axial rotation. Several *in vivo* studies reported variations from 0^o to 30^o for the clavicular axial rotation during arm abduction [130, 139]. Given that only two landmarks could be discerned to define the clavicle configuration, this result was expected. Several approaches were used in the literature to enforce the clavicular axial rotation. For example, the AC joint rotations were minimized by constraining the elongation of the conoid ligament [162]. But, the conoid ligament could elongate independently of clavicular axial rotations [28]. Also, assuming minimal rotations for the AC joint was questionable [130]. The clavicular axial rotation could be enforced using an extra constraint for q_1 in Eq. 4.6. But, this required further tuning if the clavicular axial rotation was not *a priori* known for the reconstructed motion. Nevertheless, only few weak muscles are attached to the clavicle. Therefore, underestimating its axial rotation could be expected to have negligible effects on muscle and joint force predictions [28].

The estimated AC joint angles were in good agreements with the *in vivo* measurements [138, 139]. More specifically, NRMSE between the estimated scapular posterior/anterior tilt and the measurements of [138] and [139] were at least 0.99 and 0.91, respectively. The NRMSE between the estimated scapular downward/upward rotation and the measurements of [139] was very low (-0.39 in the beginning and above 0.51 afterward). But, it was consistent with the results of [138] (NRMSE above 0.77 throughout the motion). The zero downward rotation estimated by our model placed the scapula in a rest position for the beginning of motion and was commonly reported [49, 154]. But, the associated angle according to [139] was -16^{o}. The estimated scapular protraction/retraction was well consistent with both *in vivo* measurements (NRMSE above 0.81).

The forearm joints angles had the highest sensitivities to variations in the markers trajectories. This could be explained by the propagation of the errors introduced through proximal bone segments. However, a profound sensitivity analysis was required to study the effects of uncertainties in markers trajectories on the estimated joints angles. The sensitivity analysis could illustrate relative influences of different markers on the estimated joints angles. Provided this, special attention could be paid to more robustly capture the trajectories of the influential markers.

The multi-segment optimization was solved for joints angles in each frame of the measured data. Therefore, there was no guarantee that the resulting joints angles were continuous. Continuity of the resulting joints angles is an essential attribute if they are going to be used in inverse dynamics for muscle force predictions [193, 234]. Therefore, the resulting joints angles are commonly smoothened by fitting continuous curves (often polynomials) [50, 142]. The downside of this approach is that the resulting continuous curves might not satisfy the kinematic constraint of the forward kinematic map.

A major limitation of this study was that only one subject participated. More subjects could allow a better evaluation of the proposed method, specially its performance in dealing with inter-individual differences. Given that the method required an MRI scan of the subject's glenohumeral joint, it could be expected that the model inherently considered inter-individual differences. Another limitation referred to the dependency of the method on an MRI scan. The MRI scan is often performed during routine clinical examinations of subjects. Therefore, this dependency would not widely affect practical applications of the method. This dependency could be eliminated by incorporation of a predictive method. The predictive method would provide the required information expected from the MRI scan. Indeed, the accuracy of the resulting GH estimations might be compromised. But, their accuracy might still be higher comparing to a direct use of the predictive method. Because, the accuracy of the predictive methods drops significantly by arm movements [147, 152]. The proposed method performs more efficiently during arm movements, given that it compensates soft tissue artifacts.

In conclusion, we proposed a method to reconstruct a videogrammetry-based measured motion of upper extremity including the scapula in the absence of SKMD. It provided estimation of GH, TS, and AI build on which the multi-segment optimization could be used. Its main strengths were (1) its independency of the scapula kinematics and also (2) its compensation for soft tissue artifacts. The method was evaluated within a kinematic model of the upper extremity through two scenarios. It provided accurate GH estimations and resulted in joints angles having excellent agreements with *in vivo* measurements. In a next step, the proposed method and the kinematic model could be used to predict GH joint reaction forces during activities of daily living. The resulting joint reaction forces could be used for improving treatments of GH joint osteoarthritis with total shoulder arthroplasty.

5 An initialization technique for Hill-type musculotendon models

This chapter is a preprint version of the following self-authored article that has been submitted to ASME Journal of Biomechanical Engineering.

Ehsan Sarshari, Alexandre Terrier, Alain Farron, Philippe Mullhaupt, "An initialization technique for Hill-type musculotendon models", BIO-18-1186, 2018.

Abstract

A musculotendon model associates force production behaviors of a musculotendon to its macroscopic or microscopic biophysical properties. It is therefore a key component in simulations of coordinated movements. Hill-type musculotendon models are commonly used in simulations of coordinated movements mainly due to their computational efficiency. They in fact provide a single first order ordinary differential equation representing the contraction dynamics of the musculotendon. However, the initial state of this differential equations is not granted by the model. The process of defining this initial state is often referred to as the initialization. Nevertheless, the initialization can considerably disturb force predictions of the model, specially during its transient behavior. Therefore, the aim of this study is to develop an initialization technique for a Hill-type model that avoids artificial transient behaviors. To this end, it is shown that the contraction dynamic of a Hill-type model is a singular perturbed system. The singular perturbation analysis is therefore applied on the system in order to define an approximation of its central solution. The initial value of the approximated central solution is then used as an initial state for the contraction dynamics. Two cases are considered to evaluate the developed model. They include reproduction of the experimentally measured forces on maximally activated rat soleus as well as prediction of the human middle deltoid force during measured forward flexion movement. The results indeed illustrate that the proposed initialization within the developed Hill-type model provides force predictions that are in an excellent agreement with the experimental results (mean squared prediction error less than 0.009) and are devoid of artificial transients.

5.1 Introduction

Musculotendons are the interface between the central nervous system (CNS) and the articulated skeletal system [170]. They transform neural excitation received from the CNS to forces that are applied to the skeletal system in order to perform a motor task. Therefore, a musculotendon model that can reproduce musculotendon forces for given musculotendon properties is a key component in simulations of coordinated movements [170, 171].

There exist several musculotendon models that can be broadly divided into two categories based on their development approaches, including (1) Huxley-based [172–174] and (2) Hill-type [170, 175–178] models. The former is developed based on a reductionist approach that takes into account physiological microscopic properties of tissues. It provides a distributed-parameter model of musculotendon using either a single partial differential equation (PDE) [172, 173] or a set of ordinary differential equations (ODE) [174]. In contrast, Hill-type models are developed based on a black-box description of input-output behaviors of musculotendon and its phenomenological properties. It results in a lumped-parameter model represented by a single ODE [170, 178].

The type of the model utilized depends on the goal of the simulation [171]. Given that several musculotendons are typically involved in simulations of coordinated movements [43], applications of Huxley-based models immediately become computationally demanding. Furthermore, they require several number of musculotendon parameters that are not straightforward to identify [179]. Therefore, the use of Hill-type models in simulations associated with coordinated movements are justified [170, 171].

The resulting ODE from a Hill-type model typically associates the muscle fiber velocity to a function of muscle fiber length, musculotendon length, and neural excitation [170, 175]. However, the initial state (muscle fiber length at the initial time) required to solve this ODE is not granted by the model. The procedure of estimation an initial state corresponding to a given musculotendon length and neural excitation for a Hill-type model is called initialization [171, 180]. Although, Hill-type models were extensively used in simulations of coordinated movements [21, 43], a limited effort was made regarding their initialization techniques. Nevertheless, forces reproduced by a Hill-type model can be considerably disturbed by the initialization, specially their transient behaviors [171, 181–183].

There are indeed few studies that investigated initialization techniques for Hill-type models. Musculotendon velocity was acquired and apportioned between the muscle fiber and tendon according to their linearized compliances [180, 184]. An initial state was then estimated by using the resulted muscle fiber velocity in the kinematic model of the musculotendon. However, the initialization was subject to singularities of the relative stiffness of muscle fiber and tendon. Furthermore, the estimated initial state might lack biophysical correspondence.

Therefore, the aim of this study is to develop an initialization technique for a Hill-type model that (1) avoids artificial transient behaviors in the force reproduced by the model, (2) is devoid of numerical singularities, and (3) possesses biophysical correspondence. To this end, the singular perturbation theory [235] is used on a developed Hill-type model to achieve an asymptotic approximation of its solution. The model is used to reproduce experimentally measured forces on maximally excited rat soleus reported by [183]. It is also used to predict forces associated with submaximal EMG measurements of middle deltoid during arm forward flexion. It is expected that, the developed initialization technique improves the force reproduction of the model, specially in terms of its transient behaviors.

5.2 Methods

The overall structure of Hill-type musculotendon models are presented (Section 5.2.1). The activation and contraction dynamics are also detailed (Sections 5.2.1 and 5.2.2, respectively). Our initialization technique is explained (Section 5.2.3). Two cases are

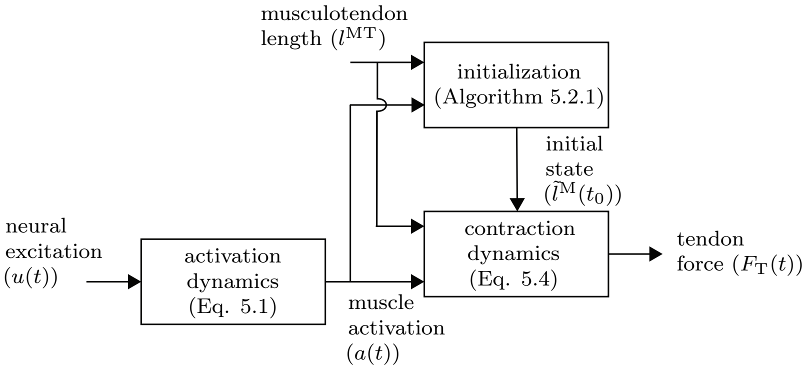

Figure 5.1: A block diagram representation of our developed initialization technique for a typical Hill-type model. In a Hill-type model, musculotendon dynamics are assumed to consist of two unidirectional coupled subsystems, namely activation and contraction dynamics. For given excitations ($a(t)$ and l^{MT}), the initialization technique defines an initial state $\tilde{l}^{\mathrm{M}}(t_0)$ for the contraction dynamics (Eq. 5.4) such that the resulting tendon force predictions are devoid of artificial transient behavior.

described to evaluate the proposed initialization within a developed Hill-type model (Section 5.2.4).

5.2.1 Hill-type musculotendon model

Given the biological complexity of musculotendons, several simplifying assumptions are commonly made in order to develop a Hill-type model [170]. They involve different aspects of musculotendons, including their functions, fibers geometries, and fibers physical properties. Musculotendons function is assumed to consist of two unidirectional coupled dynamics, namely activation dynamics and contraction dynamics (Fig. 5.1) [171]. The activation dynamics account for the musculotendon behavior from neural excitation ($u(t)$) to muscle activation ($a(t)$). The contraction dynamics replicate force reproductions for a given muscle activation and musculotendon length ($l^{\mathrm{MT}}(t)$). Fibers geometries are approximated by a set of straight parallel fibers with equal lengths that are furnished in a same plane (Fig. 5.2a). A musculotendon consists of a variety of fibers with different physical properties. However, it is approximated in terms of a scaled-up version of a single normalized fiber. A Hill-type model of a musculotendon deals merely with dynamics of a single normalized fiber. The behavior of the whole musculotendon can be therefore described as a scaled-up version of the behavior of this normalized fiber. The length, velocity, and force quantities are normalized with respect to their so-called optimum values (see section 5.2.2).

Activation dynamics

The activation dynamics associate $u(t)$ to $a(t)$. Muscle activation is a representation of the relative amount of calcium release to troponin in the muscle fiber. During muscle activation, calcium concentration increases by the sarcoplasmic reticulum, while muscle deactivation involves removal of the calcium [179]. The activation dynamics are described in Eq. 5.1. It is adapted from [170] as a simplification of the approach developed by [174].

$$\frac{da(t)}{dt} = \frac{u(t) - a(t)}{\tau(a(t), u(t))} \quad , \quad \tau(a(t), u(t)) = \begin{cases} \frac{\tau_{\text{act}}}{0.5+1.5a(t)} & u(t) \leq a(t) \\ \frac{\tau_{\text{dact}}}{0.5+1.5a(t)} & u(t) > a(t) \end{cases} \tag{5.1}$$

Where, τ_{act} and τ_{dact} are activation and deactivation time constants, respectively. Given that calcium dissociation is a less efficient process than its release, τ_{dact} is generally bigger than τ_{act}. Both $u(t)$ and $a(t)$ lie within [0 1].

The neural excitation is associated with electromyography (EMG) signal measured on a muculotendon. However, there exists no consensus in the literature on the transformation from EMG signals to $u(t)$ [236]. In the common approach in the literature, the high-passed, rectified, and low-pass filtered EMG signal is considered as $u(t)$. The cut-off frequency of the high-pass and low-pass filters can be achieved systematically for any measured EMG signal using either harmonic or residual analysis [91].

5.2.2 Contraction dynamics

The contraction dynamics consist of three different elements replicating the force production function of the musculotendon (Fig. 5.2a,b). More specifically, the active force production of the muscle fiber is modeled with a contractile element (CE). A passive elastic element is also attached in parallel to the CE in order to replicate the passive force generated by the muscle fiber during elongation. An elastic element is connected in series to the muscle fiber elements to replicate the tendon behavior associated to tendon elongations.

The force produced in each of these elements is defined by a number of normalized functions, including muscle force-length ($f^{\text{L}}(.)$), muscle force-velocity ($f^{\text{V}}(.)$), muscle passive force ($f^{\text{P}}(.)$), and tendon force-length ($f^{\text{T}}(.)$) relationships (Fig. 5.2b,c,d,e,f). We obtained these functions by fitting smooth curves (C^{∞}) to experimental data reported by [7, 170, 173, 178, 182, 183, 237–244]. The force values of these functions are normalized with respect to the maximum (optimum) muscle fiber force (F_{O}). The muscle length (l^{M}) and velocity (v^{M}) and tendon length (l^{T}) values are also normalized with respect to the optimum muscle fiber length (l^{M}_{O}) and velocity (v^{M}_{O}) and tendon slack length (l^{T}_{S}), respectively. The l^{M}_{O} and v^{M}_{O} correspond to the situations when the muscle force-length and muscle force-velocity relationships are at maximum and zero force, respectively.

The contraction dynamics of a Hill-type model are developed by considering force equilibrium between the muscle fiber and tendon (Eq. 5.2).

$$F_{\mathrm{O}}\left[a(t)f^{\mathrm{L}}(\tilde{l}^{\mathrm{M}})f^{\mathrm{V}}(\tilde{v}^{\mathrm{M}})+f^{\mathrm{P}}(\tilde{l}^{\mathrm{M}})\right]\cos\alpha = F_{\mathrm{O}}f^{\mathrm{T}}(\tilde{l}^{\mathrm{T}}) \tag{5.2}$$

Where, the tilde sign denotes the corresponding normalized values. The terms on the left hand side of Eq. 5.2 are the forces produced in CE and parallel passive element, respectively. The right hand side is the tendon force. The α is the pennation angle of the muscle fibers (Fig. 5.2a,b). Given that the muscle fiber volume remains constant in a vast majority of musculotendons [245], the height of the muscle fibers (h in Fig. 5.2a) is often assumed to remain unchanged. That is

$$l^{\mathrm{M}}\sin\alpha = l_{\mathrm{O}}^{\mathrm{M}}\sin\alpha_{\mathrm{O}} \tag{5.3}$$

where, α_{O} is the pennation angle at the optimum muscle fiber length.

Given that $l^{\mathrm{M}}\cos\alpha = l^{\mathrm{MT}} - l^{\mathrm{T}}$, the following implicit ODE in terms of $\dot{\tilde{l}}^{\mathrm{M}}$ can be derived for the contraction dynamics by substituting Eq. 5.3 in Eq. 5.2.

$$\begin{aligned}\left[a(t)f^{\mathrm{L}}(\tilde{l}^{\mathrm{M}})f^{\mathrm{V}}(\tfrac{l_{\mathrm{O}}^{\mathrm{M}}}{v_{\mathrm{O}}^{\mathrm{M}}}\dot{\tilde{l}}^{\mathrm{M}})+f^{\mathrm{P}}(\tilde{l}^{\mathrm{M}})\right]\sqrt{1-\left(\tfrac{\sin\alpha_{\mathrm{O}}}{\tilde{l}^{\mathrm{M}}}\right)^{2}}\\ = f^{\mathrm{T}}(\tfrac{l^{\mathrm{MT}}-l_{\mathrm{O}}^{\mathrm{M}}\sqrt{\tilde{l}^{\mathrm{M}2}-\sin{\alpha_{\mathrm{O}}}^{2}}}{l_{\mathrm{S}}^{\mathrm{T}}})\end{aligned} \tag{5.4}$$

Given that the implicit formulation of Eq. 5.4 is numerically better conditioned comparing to its explicit formulation (Eq. 5.6), it is preferred for numerical integration [246]. In order to avoid $\tilde{l}^{\mathrm{M}}$ reaching unrealistic short lengths, the unilateral conditioning of Eq. 5.5 is included in the numerical integration of contraction dynamics (Eq. 5.4). It also prevents Eq. 5.4 to become numerically stiff due to small forces produced by the force-length relationship for unrealistic short $\tilde{l}^{\mathrm{M}}$.

$$\dot{\tilde{l}}^{\mathrm{M}} = \begin{cases} 0 & \tilde{l}^{\mathrm{M}} < \max\left(f_{\mathrm{inv}}^{\mathrm{L}}(0),\sin\alpha_{\mathrm{o}}\right) \;\;\&\;\; \dot{\tilde{l}}^{\mathrm{M}} < 0 \\ \dot{\tilde{l}}^{\mathrm{M}} & else \end{cases} \tag{5.5}$$

Where, $f^{\mathrm{L}}_{\mathrm{inv}}(.)$ is the inverse function of muscle fiber force-length relationship defined over [0 1].

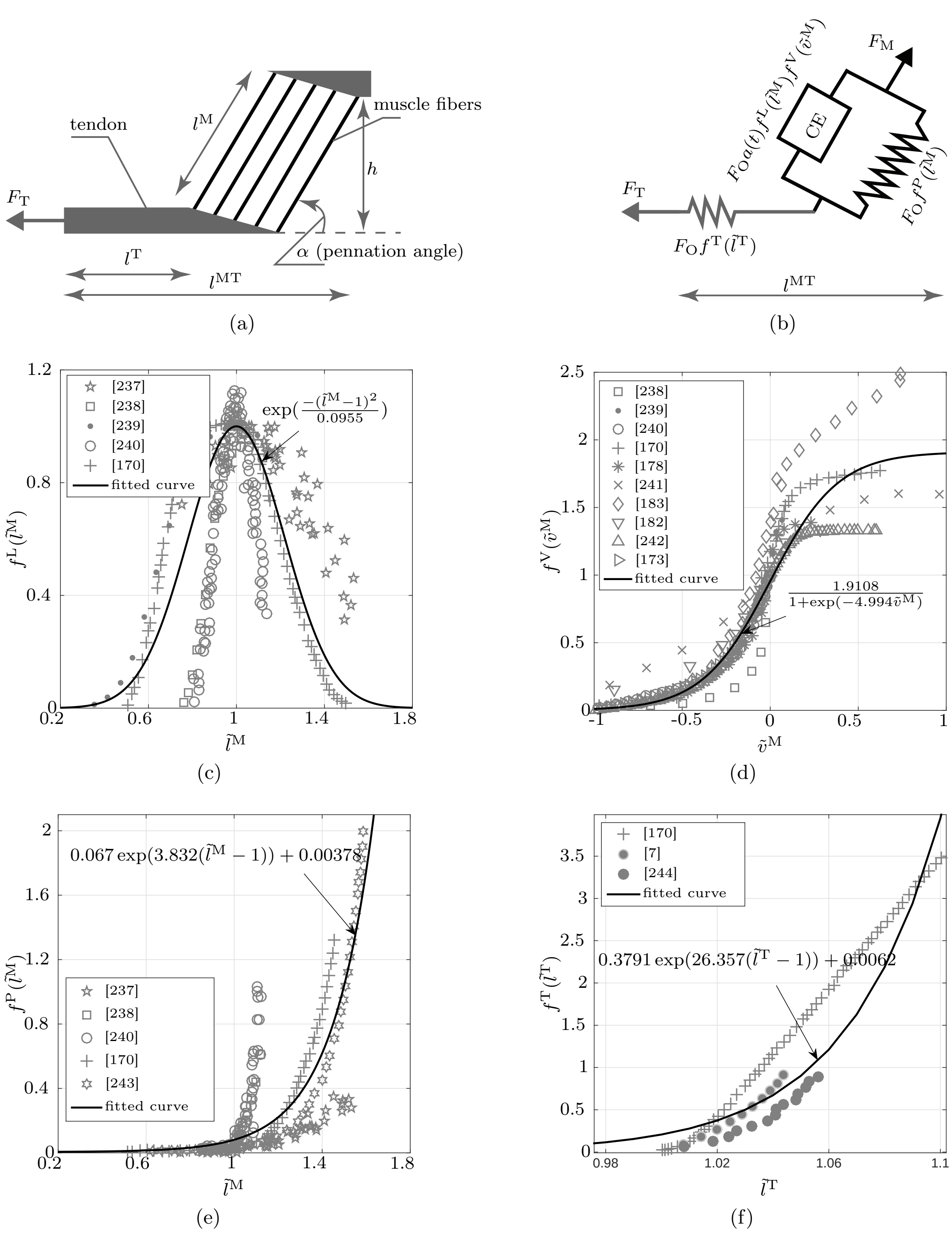

Figure 5.2: Musculotendon contraction dynamics, (a) musculotendon geometries are approximated by a set of straight parallel muscle fibers with equal lengths (l^{M}) that are furnished in a same plane together with the straight tendons of length l^{T}. (b) Mechanical correspondence of the Hill-type musculotendon model. The force produced by the muscle fiber (F_{M}) is the resultant of the force generated by the CE ($F_{\mathrm{O}}a(t)f^{\mathrm{L}}(\tilde{l}^{\mathrm{M}})f^{\mathrm{V}}(\tilde{v}^{\mathrm{M}})$) and the passive elastic element ($F_{\mathrm{O}}f^{\mathrm{P}}(\tilde{l}^{\mathrm{M}})$). The tendon force ($F_{\mathrm{T}}$) is equal to $F_{\mathrm{O}}f^{\mathrm{T}}(\tilde{l}^{\mathrm{T}})$.
The normalized functions are obtained by fitting smooth curves to the experimental data of [7, 170, 173, 178, 182, 183, 237–244]. (c) Contractile element force-length relationship, (d) contractile element force-velocity relationship, (e) passive parallel element force-length relationship, and (f) tendon force-length relationship.

5.2.3 Initialization

The solution of the developed Hill-type model is affected by the initial state ($\tilde{l}^{\mathrm{M}}(t_0)$) of the contraction dynamics (Eq. 5.4). An inappropriate initial state can disturb the resulted $\tilde{l}^{\mathrm{M}}(t)$ and consequently affect the force predicted by the model ($F_{\mathrm{T}}(t)$). In order to further elaborate on this argument a benchmark example is simulated using the developed musculotendon model.

An arbitrary musculotendon ($F_{\mathrm{O}} = 1$ N, $l_{\mathrm{O}}^{\mathrm{M}} = 2$ cm, $v_{\mathrm{O}}^{\mathrm{M}} = 11$ cms^{-1}, $\alpha_{\mathrm{O}} = 30^{\mathrm{o}}$, and $l_{\mathrm{S}}^{\mathrm{T}} = 10$ cm) is simulated for a constant neural excitation ($u(t) = 1$) and a sinusoidal musculotendon length excitation ($l^{\mathrm{MT}}(t) = l_{\mathrm{S}}^{\mathrm{T}} + l_{\mathrm{O}}^{\mathrm{M}} \cos\alpha_{\mathrm{O}} + l_{\mathrm{O}}^{\mathrm{M}} \sin 2\pi t$). The model response for different $\tilde{l}^{\mathrm{M}}(t_0)$ are presented in terms of $\tilde{l}^{\mathrm{M}}(t)$ and $F_{\mathrm{T}}(t)$. Several transient behaviors can be observed (Fig. 5.3). However, all the different branches of the response (perturbed responses) converge to a central solution. The transient behavior of $\tilde{l}^{\mathrm{M}}(t)$ due to an inappropriate $\tilde{l}^{\mathrm{M}}(t_0)$ considerably alters $F_{\mathrm{T}}(t)$. Therefore, the goal of our initialization technique is to find the initial state corresponding to a model response that always stays on the central solution. In other words, we will approximate the initial state associated to the central solution. This assures that the model transient response is sufficiently devoid of artificial transients. To this end, Tikhonov's theorem of singular perturbation analysis [235] is applied to Eq. 5.4. At a first step, an approximation of the central solution is found. The initial state of this approximation is then used as the initial state of the Eq. 5.4.

An explicit form of Eq. 5.4 is obtained as follow (Eq. 5.6).

$$\frac{l_{\mathrm{O}}^{\mathrm{M}}}{v_{\mathrm{O}}^{\mathrm{M}}}\dot{\tilde{l}}^{\mathrm{M}} = f_{\mathrm{inv}}^{\mathrm{V}}\left(\frac{1}{a(t)f^{\mathrm{L}}(\tilde{l}^{\mathrm{M}})}\left[\frac{f^{\mathrm{T}}(\frac{l^{\mathrm{MT}} - l_{\mathrm{O}}^{\mathrm{M}}\sqrt{\tilde{l}^{\mathrm{M}2} - \sin{\alpha_{\mathrm{O}}}^2}}{l_{\mathrm{S}}^{\mathrm{T}}})}{\sqrt{1-\left(\frac{\sin\alpha_{\mathrm{O}}}{\tilde{l}^{\mathrm{M}}}\right)^2}} - f^{\mathrm{P}}(\tilde{l}^{\mathrm{M}})\right]\right) \tag{5.6}$$

In a compact form Eq. 5.6 becomes:

$$\epsilon\dot{\tilde{l}}^{\mathrm{M}} = g(t, a, l^{\mathrm{MT}}, \tilde{l}^{\mathrm{M}}, \epsilon) \tag{5.7}$$

where, $\epsilon = \frac{l_{\mathrm{O}}^{\mathrm{M}}}{v_{\mathrm{O}}^{\mathrm{M}}}$. For $\epsilon = 0$, Eq. 5.7 degenerates to a transcendental equation ($0 = g(.)$) whose isolated real roots are defined as

$$\bar{\tilde{l}}^{\mathrm{M}} = h(a, l^{\mathrm{MT}}) \tag{5.8}$$

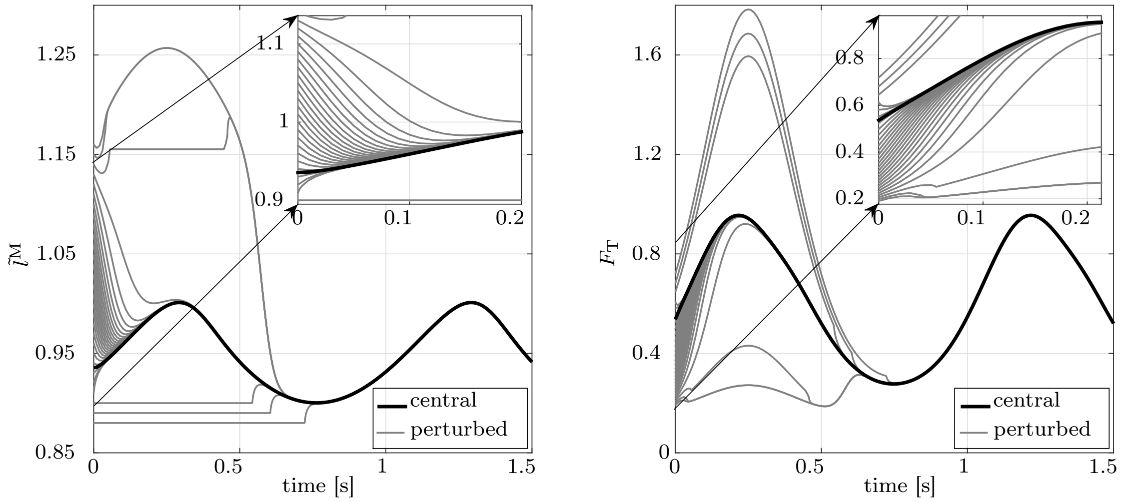

(a) (b)

Figure 5.3: Effect of the initial state ($\tilde{l}^{\mathrm{M}}(t_0)$) of the contraction dynamics on the musculotendon response: (a) normalized muscle-fiber length ($\tilde{l}^{\mathrm{M}}(t)$) and (b) tendon force ($F_{\mathrm{T}}(t)$). Several transient behaviors are observed. However, all the different branches of the perturbed responses (gray curves) converge to a central solution (black curve).

Algorithm 5.2.1 presents the initialization technique developed for the Hill-type model (see also Fig. 5.1).

Algorithm 5.2.1 (model initialization) Given the muscuoltendon model in Eq. 5.1 and Eq. 5.4

1. Consider the initial values of the model excitations, including $a(t_0)$ and $l^{\mathrm{MT}}(t_0)$.
2. Solve the transcendental equation of Eq. 5.8 for the excitation values of step 1 and define $\bar{\tilde{l}}^{\mathrm{M}}(t_0)$.
3. Feed $\bar{\tilde{l}}^{\mathrm{M}}(t_0)$ to Eq. 5.4 as its initial state.

We use an adaptation of Tikhonov's theorem to guarantee that $\bar{\tilde{l}}^{\mathrm{M}}$ is an of order $O(\epsilon)$ approximation of the central solution of Eq. 5.6 (Theorem 5.4.1). This order of magnitude approximation ($O(\epsilon)$) is defined in Definition 5.4.1. Therefore, we consider its initial value ($\bar{\tilde{l}}^{\mathrm{M}}(t_0)$) as an of order $O(\epsilon)$ approximation for the initial state of the central solution of Eq. 5.6.

5.2.4 Evaluation of the method

Two cases are considered to evaluate the performance of the developed initialization technique within the musculotendon model. In the first case, the model reproduces the experimentally measured forces on a maximally activated rat soleus reported by [183]. The musculotendon length excitations (l^{MT}) are considered according to the same experiments [183]. That is, a general sinusoidal excitation is considered with six different maximum amplitudes, including ±0.05 mm, ±0.1 mm, ±0.25 mm, ±0.5 mm, ±1 mm, and ±2 mm. According to [183], the musculotendon parameters are set as $\tau_{\mathrm{dact}} = 40$ ms and $l^{\mathrm{M}}_{\mathrm{O}} = l^{\mathrm{T}}_{\mathrm{S}} = 1.71$ cm. However, the other four musculotendon parameters necessary to simulate the model are not given in [183]. Therefore, a nonlinear parameter identification [247] is casted as follows. It defines τ_{act}, F_{O}, $v^{\mathrm{M}}_{\mathrm{O}}$, and α_{O} such that the mean squared prediction error (MSPE) between $F_{\mathrm{T}}(t)$ as the model force prediction and the experimental results of ±0.1 mm excitation denoted by $F_{\mathrm{exp}_{\pm 0.1}}$ is minimized. The resulting parameters from Eq. 5.9 are then used to simulate the rest of the above mentioned experimental trials.

$$\begin{aligned}
\text{min}\,. \quad & \tfrac{1}{t_1}\textstyle\int_0^{t_1} (F_{\mathrm{T}}(t) - F_{\mathrm{exp}_{\pm 0.1}}(t))^2 dt \\
\text{s.t.} \quad & \Big[a(t) f^{\mathrm{L}}(\tilde{l}^{\mathrm{M}}) f^{\mathrm{V}}(\tfrac{l^{\mathrm{M}}_{\mathrm{O}}}{v^{\mathrm{M}}_{\mathrm{O}}} \dot{\tilde{l}}^{\mathrm{M}}) + f^{\mathrm{P}}(\tilde{l}^{\mathrm{M}})\Big] \sqrt{1 - \Big(\tfrac{\sin\alpha_{\mathrm{O}}}{\tilde{l}^{\mathrm{M}}}\Big)^2} \\
& \qquad = f^{\mathrm{T}}\big(\tfrac{l^{\mathrm{MT}} - l^{\mathrm{M}}_{\mathrm{O}} \sqrt{\tilde{l}^{\mathrm{M}2} - \sin{\alpha_{\mathrm{O}}}^2}}{l^{\mathrm{T}}_{\mathrm{S}}}\big) \\
& \tilde{l}^m(t_0) = \bar{\tilde{l}}^m(t_0)
\end{aligned} \tag{5.9}$$

In the second case, the model is used to predict forces in human middle deltoid during forward flexion with 2 kg weight in hand. The EMG neural excitations and shoulder kinematics are measured during several trials of the same movement on a young healthy subject [212]. The corresponding length excitations are obtained performing inverse kinematics on the measured kinematics using a musculoskeletal model of upper extremity [248]. The measured EMG was treated according to section 5.2.1, and the effect of its variance (due to the several trials) on the predicted force is also presented. The musculotendon parameters of middle deltoid are adapted from [203].

5.3 Results

For the first case, the parameter identification resulted in the following parameters, $\tau_{\mathrm{act}} = 22.2$ ms, $F_{\mathrm{O}} = 1.79$ N, $v^{\mathrm{M}}_{\mathrm{O}} = 0.06\ \mathrm{ms}^{-1}$, and $\alpha_{\mathrm{O}} = 6.59^{\mathrm{o}}$.

The highest and lowest force predicted by the model were around 69% and 106% of the F_{O} associated to ±0.05 mm and ±2 mm trials, respectively (Fig. 5.4). The mean squared prediction errors between $F_{\mathrm{T}}(t)$ and F_{exp} for the different trials increased with the amplitudes of the musculotendon length excitations. More specifically, they varied from 0.0011 to 0.0088, with the former being associated to the ±0.05 mm trial.

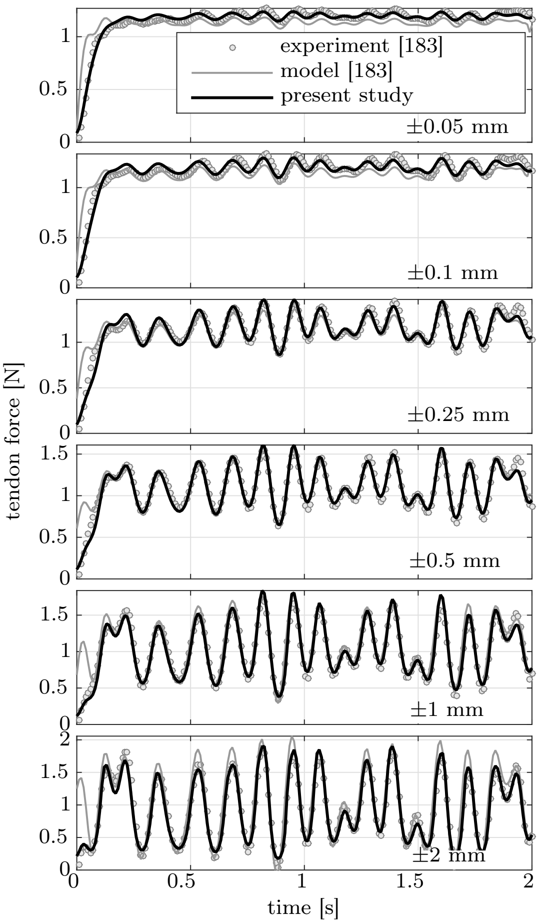

Figure 5.4: Reproductions of the experimentally measured forces on the maximally activated rat soleus from [183] by the developed model. Six different experimental trials were simulated. They were associated with different amplitudes of musculotendon length excitation, including ±0.05 mm, ±0.1 mm, ±0.25 mm, ±0.5 mm, ±1 mm, and ±2 mm. The forces predicted by a typical Hill-type model from [183] was also presented.

For the second case, the force predicted for the middle deltoid increased initially with the arm flexion to its maximum (almost 490 N equivalent to 57% body weight) at 50° (Fig. 5.5). It reached its minimum (around 20% body weight) at the end of the simulated flexion.

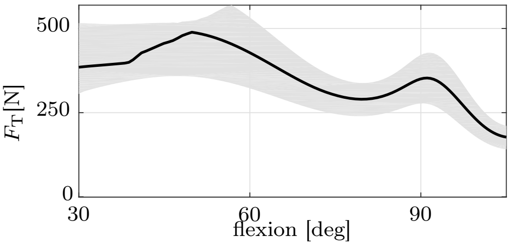

Figure 5.5: Force predicted by the developed model for the middle deltoid during arm forward flexion with 2 kg weight in hand (solid line). The EMG neural excitation and the shoulder kinematics were measured during several trials of the same motion on a subject and transformed to $u(t)$ and $l^{\mathrm{MT}}(t)$. The effect of variances in EMG data on the predicted force presented by the gray shaded area.

5.4 Discussion

The aim of this study was to develop an initialization technique for Hill-type musculotendon models so that the model predictions were devoid of artificial transients. The transient behaviors caused by inappropriate initializations could considerably disturb force predictions of the model. We showed that the ODE associated to the contraction dynamics of a Hill-type model was a singular perturbed system. Therefore, singular perturbation analysis was applied to provide an approximation of the central solution of the contraction dynamics. The initial value of the approximated central solution was then used as the initial state of the contraction dynamics. The developed model together with its initialization was evaluated by reproducing the experimentally measured forces in maximally activated rat soleus and also the middle deltoid forces during forward flexion. The predicted forces for the rat soleus was also compared with predictions of a Hill-type model developed in [183].

For the first case, the model predictions were in an excellent agreement (MSPE less than 0.009) with the experimental results. Furthermore, the model predictions did not experience any artificial transients. However, the corresponding predictions from the model developed in [183] provided at least one order of magnitude higher MSPE. For instance, the MSPE for the ±2 mm simulation was almost 550% higher comparing to the corresponding value of the developed model in the present study. Furthermore, the performance of our initialization technique would be even more evident if a shorter simulation time is considered. For instance, the MSPE associated with the transient part ([0 0.2s]) of the ±1 mm simulation were 0.008 and 0.17 for this study and that of [183], respectively.

The parameter identification resulted in musculotendon parameters for rat soleus that were comparable to those reported by *in vivo* studies, e.g. [249]. This could explain that the model represents the physiology of the system and segregated it from a curve-fitting exercise. Furthermore, the parameter identification was merely performed for one case out of the six experimental trials.

For the second case, the predicted force for middle deltoid held physiological correspondence with previously reported data in the literature [52]. It was frequently reported that inverse-dynamics based predictions of muscles forces underestimated them [21, 188]. Therefore, muscle-driven predictions of muscle forces using musculotendon dynamics could be a potential alternative approach [43, 193, 212].

A limitation of the developed model was that the effects of fatigue [250] and temperature [251] on musculotendon dynamics were neglected. However, during the two cases studied special attention was paid to provide sufficient resting intervals to the musculotendon tissues. In case of applications for which this surrogate approach could not be used, it would be therefore necessary to account for musculotendon fatigue and temperature. The musculotendon fatigue has been approximated often by compromising optimum muscle-fiber force as a linear function of simulation time, e.g. [252]. That is, $F_{\mathrm{C}}(t) = F_{\mathrm{O}}(1-\lambda_f t)$, where $F_{\mathrm{C}}(t)$ is the compromised optimum muscle-fiber force, and λ_f is a small positive constant. It is indeed straightforward to include this fatigue model in the developed model, if necessary.

Future developments should distinguish between slow and fast twitch musculotendons dynamics [91, 170]. This could be accounted for by considering distinguished muscle-fiber force-length and velocity relationships for slow and fast twitch muscles. Nevertheless, in the experimental data used in the present study defining the muscle-fiber force-length relationship two distinct patterns could be observed. This could be associated with the fact that different musculotendons with different twitch properties were used.

The developed Hill-type model required seven musculotendon parameters in order to replicate the behavior of a given musculotendon. However, it is not yet straightforward to obtain these parameters [21, 203]. There are number of cadaveric anthropometry studies providing these parameters for different musculotendon groups of humans, e.g. [203] and [253] for upper and lower extremities, respectively. The accuracy of the model in providing inter-individual predictions can be considerably affected by the uncertainties in these parameters. Therefore, rigorous identifications of musculotendon parameters are the major bottleneck of applications of musculotendon dynamics. Systematic sensitivity analyses can provide insight into the role played by different musculotendon parameters and their contributions in effecting relative model behavior.

In conclusion, we proposed an initialization technique for a developed Hill-type musculotendon model. It had three main advantages. It avoided the model force predictions exhibiting any artificial transients. It was devoid of numerical singularities despite the previous initializations techniques [180, 184]. It also possessed biophysical correspondence, given that no extra assumptions was considered in its development. The model performance was evaluated through two cases and was in excellent agreement with respect to those of experimental studies. In a next step, the developed model would be incorporated into an EMG-assisted shoulder model to simulate coordinated movements.

Appendix: Musculotendon central solution

The velocity of $\tilde{l}^{\mathrm{M}}$ calculated as $\dot{\tilde{l}}^{\mathrm{M}} = \frac{g(.)}{\epsilon}$ can be large due to smallness of ϵ. Therefore, $\tilde{l}^{\mathrm{M}}$ may rapidly converge to $\bar{\tilde{l}}^{\mathrm{M}}$ that is the equilibrium of Eq. 5.7. In fact, having set $\epsilon = 0$, the transient convergence of $\tilde{l}^{\mathrm{M}}$ was made instantaneous. However, this convergence cannot be excepted unless certain stability conditions for the transient (boundary-layer) are satisfied. This boundary-layer is mathematically defined in Definition 5.4.2. The forthcoming adaptation of Tikhonov's theorem guarantees $\bar{\tilde{l}}^{\mathrm{M}}$ to be an of order $O(\epsilon)$ approximation of the central solution of Eq. 5.6 (Theorem 5.4.1). This order of magnitude approximation ($O(\epsilon)$) is defined as

Definition 5.4.1 ($O(\delta_2(\epsilon))$ approximation) $\delta_1(\epsilon)$ is an of order $O(\delta_2(\epsilon))$ approximation if there exist positive constants k and c such that

$$|\delta_1(\epsilon)| \leq k|\delta_2(\epsilon)|, \quad \forall \ |\epsilon| < c$$

Definition 5.4.2 (boundary-layer) Having defined y as $y = \bar{\tilde{l}}^{\mathrm{M}} - h(a, l^{\mathrm{MT}})$ that shifts the equilibrium of Eq. 5.7 to the origin, the boundary-layer can be derived as below by substituting y in Eq. 5.7.

$$\frac{dy}{d\tau} = g(t, a, l^{\mathrm{MT}}, y + h(a, l^{\mathrm{MT}}, 0))$$

where, $\tau = \frac{1}{\epsilon}t$.

Theorem 5.4.1 (singular perturbation) Consider the singular perturbation problem of Eq. 5.7 and let Eq. 5.8 be its equilibrium. Assume the following conditions to be satisfied for $t \in [t_0 \ t_1]$

- The function $g(.)$ and its first partial derivatives with respect $(a, l^{\mathrm{MT}}, \tilde{l}^{\mathrm{M}}, \epsilon)$ are continuous. The function $h(a, l^{\mathrm{MT}})$ and the Jacobian $\frac{\partial g(t,a,l^{\mathrm{MT}},\tilde{l}^{\mathrm{M}},0)}{\partial \tilde{l}^{\mathrm{M}}}$ have continuous first partial derivatives with respect to their arguments.
- The musculotendon inputs ($a(t)$ and $l^{\mathrm{MT}}(t)$) are bounded for all $t \in [t_0 \ t_1]$.
- The origin of the boundary-layer model (Definition 2.2) is exponentially stable.

Then, Eq. 5.7 as a singular perturbation problem has a unique solution $\tilde{l}^{\mathrm{M}}(t, \epsilon)$ on $[t_0 \ t_1]$, and

$$\tilde{l}^{\mathrm{M}}(t,\epsilon) - \bar{\tilde{l}}^{\mathrm{M}} - y(\tau) = O(\epsilon)$$

According to Theorem 5.4.1, $\bar{\tilde{l}}^{\mathrm{M}}$ is guaranteed to be an of order $O(\epsilon)$ approximation of the central solution of Eq. 5.6 on $[t_0\ t_1]$. Therefore, we consider its initial value ($\bar{\tilde{l}}^{\mathrm{M}}(t_0)$) as an of order $O(\epsilon)$ approximation for the initial state of the central solution of Eq. 5.6.

6 EMG-Assisted Load-Sharing for Muscle Force Prediction in Upper-Extremity

This chapter is a preprint version of the following self-authored article that has been submitted to Journal of Medical Engineering and Physics.

Ehsan Sarshari, Matteo Mancuso, Alexandre Terrier, Alain Farron, Philippe Mullhaupt, Dominique Pioletti, “EMG-Assisted Load-Sharing for Muscle Force Prediction in Upper-Extremity”, MEP-D-18-00262, 2018.

Abstract

Prediction of muscles forces in an over-actuated musculoskeletal model involves optimal distributions of net joints moments among muscles by a standard load-sharing (SLS). Given that co-contractions of antagonistic muscles are counterproductive in the net joints moments, the SLS falls short of predicting them. However, muscle co-contractions play crucial roles in the stability of upper extremity joints, specially the glenohumeral (GH) joint. Therefore, the aim of this study is to test the hypothesis that inclusions of measured electromyography (EMG) data into the SLS can improve its predictions of muscle co-contractions. To this end, measured EMG data of fifteen muscles are fed into a musculotendon model. It reproduces their associated muscles forces. Portions of the resulting muscle forces are used as upper and lower bounds in a modified SLS. Given the direct incorporation of the EMG data in the modified SLS, it is called EMG-assisted load-sharing (EALS). We evaluate the EALS during arm flexion and abduction. The results are presented in terms of muscles forces, GH joint reaction forces (JRF), and the intersection foci of JRF and the glenoid fossa. A so-called stability ratio is also defined to quantify the GH joint stability. The results confirm that higher muscle co-contractions are predicted comparing to the SLS (e.g. above 50 N higher forces for both triceps long and biceps long during arm flexion). Also, JRF predictions compared to *in vivo* measurements are improved (on average 88% better predictions for the maximum JRF). It is verified that the developed EALS can better reproduce muscle co-contractions comparing to the SLS.

6.1 Introduction

Noninvasive measurement of muscle forces remains an elusive goal [185]. However, predictions of these forces can be obtained using musculoskeletal models. In the available musculoskeletal models, equilibrium equations are obtained for net joints moments using inverse dynamics [14, 22, 100]. There are more muscles than the number of the equilibrium equations (over-actuation). Therefore, the SLS is used to distribute the net joints moments among muscles [51, 52, 186]. The SLS predicts muscle forces by optimizing a physiological cost function subject to constraints. The constraints are associated with the equilibrium equations, muscle forces upper/lower bounds, and joints stability [39]. Antagonistic muscles are counterproductive in the net joints moments. Therefore, the SLS overlooks forces produced by antagonistic muscles (co-contractions) [26, 187–189]. Consequently, joint contact forces are also underestimated [43, 190, 191]. Predictions of muscle and joint forces can be improved by considering co-contractions, especially for the upper extremity joints. Because, the stability of the GH joint is mainly achieved through muscle co-contractions in the upper extremity [67, 192, 193].

For the upper extremity, few studies improved muscle force predictions by cosidering co-contractions. They enforced co-contractions either by tailoring the optimization of

SLS [39, 194, 195] or by explicit use of measured EMG data [43, 188, 196–198]. However, there were limitations associated to these studies.

Co-contraction was enforced by introducing shift parameters [194] and negative weighting factors [195]. They were used to alleviate the SLS cost function growth due to co-contraction. The choice of shift parameters and weighting factors required *a priori* knowledge of antagonistic muscles. However, this was not straightforward to achieve, given complexities of the upper extremity. For instance, muscles could act simultaneously as agonistic and antagonistic in the upper extremity. A stability constraint was introduced for the GH joint [39] and was commonly used in the upper extremity musculoskeletal models [14, 100]. It constrained SLS solutions such that the resulting JRF always pointed toward inside of the glenoid fossa. Co-contractions were therefore enforced by compromising the SLS optimal solution. But, the model still underestimated the co-contractions [43].

Explicit use of measured EMG data in models did not require further information of antagonistic muscles. It could therefore provide rather straightforward predictions of co-contractions [43, 188, 196–198]. However, the relationship between predicted muscle forces and measured EMG data was over-simplified [188, 196–198]. This deviated from the nonlinear dynamical behavior of musculotendons [170]. The net moments produced by direct applications of measured EMG also failed to satisfy the equilibrium equations [188, 196, 197]. Therefore, the predicted co-contractions might lack a physiological correspondence. Several combinations of measured EMG data were used [43] to predict a joint reaction force closer to experimental results [199]. But, the model did not allow inclusion of all the fourteen measured EMG data, and only a subset of them (four muscles) were used.

Therefore, the aim of this study is to test the hypothesis that inclusions of measured EMG data into the SLS can improve its predictions of muscle co-contractions. To this end, an EALS is developed by modifying the SLS of an upper extremity musculoskeletal model. Muscle forces associated with measured EMG of fifteen superficial muscles are calculated and fed into the EALS. Predicted muscle and joint forces are compared with those of the SLS and *in vivo* measurements [199]. A stability ratio is introduced to quantify the GH joint stability.

6.2 Methods

An upper extremity musculoskeletal model is developed (Section 6.2.1). EMG and motion data are measured during two activities (Section 6.2.2). The measured motions are reconstructed in terms of joints angles using a multi-segment optimization (Section 6.2.3). A musculotendon model is developed to reproduce the muscle forces associated to muscles with measured EMG data (Section 6.2.4). The EALS is detailed (Section 6.2.5). The developed EALS is evaluated within the musculoskeletal model and is compared to the SLS (Section 6.2.6).

6.2.1 Upper extremity Musculoskeletal model

Kinematic model

A musculoskeletal model of the upper extremity is developed from MRI scans of the right shoulder of a healthy male subject (29 year, 186 cm, and 85.5 kg) (Fig. 6.1a). It consists of six rigid bodies including thorax, clavicle, scapula, humerus, ulna, and radius. The hand is assumed to be rigidly tied to the radius. It has nine DOFs attributing to three ball-and-socket joints associating with sternoclavicular (SC), acromioclavicular (AC), and glenohumeral (GH) joints and two hinge joints for humeroulnar (HU) and radioulnar (RU) joints and two holonomic constraints (Fig. 6.1b). Two constraints restrict trigonum scapulae (TS) and angulus inferior (AI) on the scapula medial boarder to glide over two ellipsoids approximating the thorax and their underlying soft tissues (Eq. 6.1). The configuration of each bone segment is defined using at least three non-collinear bony landmarks. Only two bony landmarks can be discerned for the clavicle. The medial epicondyle (EM), lateral epicondyle (EL), and their middle point (HU) on the humerus are borrowed for the ulna and the radius. The ISB recommendations [201] are followed to define six bone-fixed frames. The joints coordinates are coincide with the bone-fixed frames. An Euler angle sequence of $X - Y - Z$ is used for both the SC and the AC joints, but $Z - Y - Z$ is considered for the GH joint. A generalized coordinate vector ($\boldsymbol{q} = [q_1 \;\ldots\; q_{11}]^T$) is considered to define the upper extremity configuration. The following forward kinematic map (ξ) defines the spatial coordinate of the j^{th} bony landmark ($\boldsymbol{x}_j$) associated with the generalized coordinates at time t.

$$\begin{aligned}
&\xi : C_s \subset R^{11} \mapsto W_s \subset R^3 \\
&\xi(\boldsymbol{q}(t)) = \boldsymbol{x}_j(t), \quad j = \{\text{C7}, \;\ldots,\; \text{RS}\}_{1\times 14} \\
&\Phi_{\text{TS}}(\boldsymbol{q}(t)) = ({}_t\boldsymbol{TS}(t) - {}_t\boldsymbol{e}_0)^T E_{\text{TS}}({}_t\boldsymbol{TS}(t) - {}_t\boldsymbol{e}_0) - 1 = 0 \\
&\Phi_{\text{AI}}(\boldsymbol{q}(t)) \;= ({}_t\boldsymbol{AI}(t) - {}_t\boldsymbol{e}_0)^T E_{\text{AI}}({}_t\boldsymbol{AI}(t) - {}_t\boldsymbol{e}_0) \; - 1 = 0
\end{aligned} \tag{6.1}$$

Where, C_s and W_s are the coordinate space and work space of the model [228]. Two holonomic constraints ($\Phi_{\text{TS}} = 0$ and $\Phi_{\text{AI}} = 0$) replicate the kinematic relationships between the scapula and the thorax. The left-hand side subscript t specifies that the landmarks are in the thorax (inertial) frame. The ellipsoids center is ${}_t\boldsymbol{e}_0$, and E_{TS} and E_{AI} are the ellipsoids matrices.

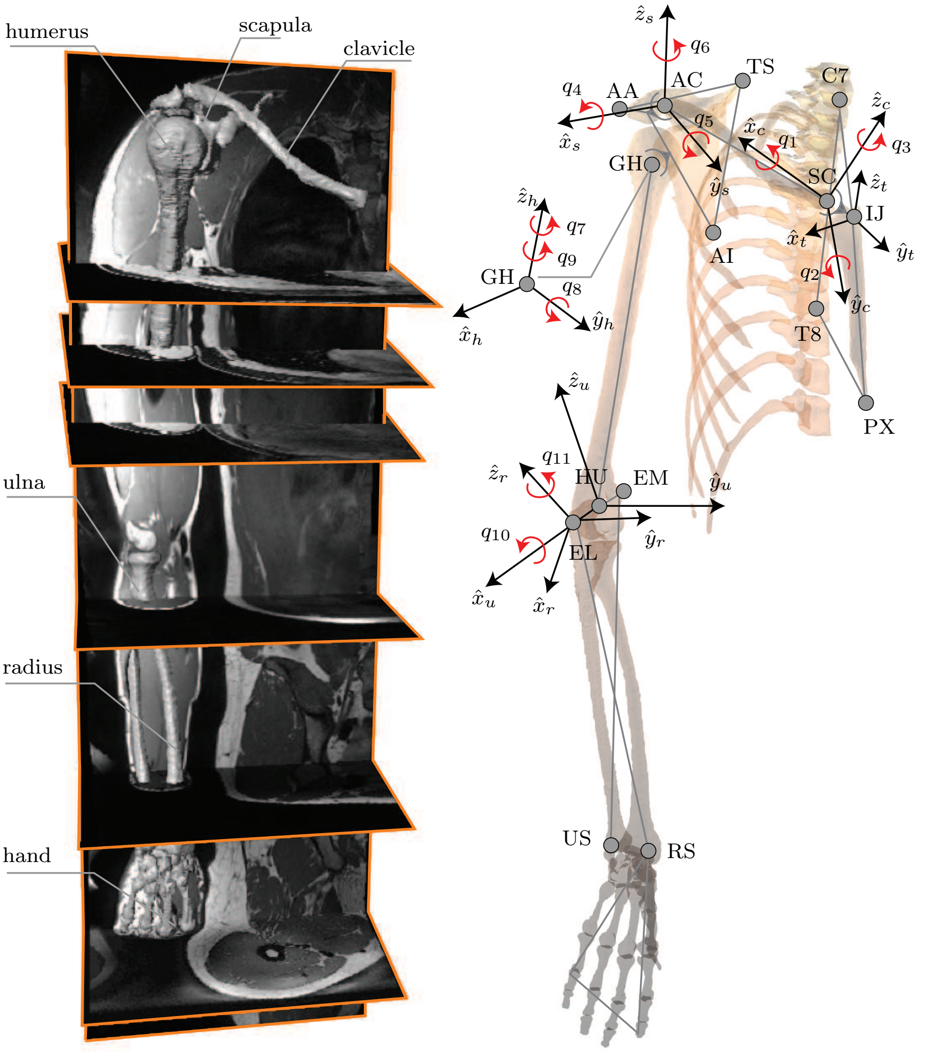

(a) (b)

Figure 6.1: (a) MRI scans of a healthy subject are used to develop the model. (b) The kinematic model. Fifteen bony landmarks are used, including incisura jugularis (IJ), processus xiphoideus (PX), 7th cervical vertebra (C7), 8th thoracic vertebra (T8), SC, AC, AA, EM, HU, EL, radial styloid (RS), and ulnar styloid (US). The bone-fixed frames are: thorax frame $\{\boldsymbol{IJ}, \hat{x}_t, \hat{y}_t, \hat{z}_t\}$, clavicle frame $\{\boldsymbol{SC}, \hat{x}_c, \hat{y}_c, \hat{z}_c\}$, scapula frame $\{\boldsymbol{AC}, \hat{x}_s, \hat{y}_s, \hat{z}_s\}$, humerus frame $\{\boldsymbol{GH}, \hat{x}_h, \hat{y}_h, \hat{z}_h\}$, ulna frame $\{\boldsymbol{HU}, \hat{x}_u, \hat{y}_u, \hat{z}_u\}$, and radius frame $\{\boldsymbol{EL}, \hat{x}_r, \hat{y}_r, \hat{z}_r\}$. The generalized coordinates consist of q_1: SC axial rotation, q_2: SC depression/elevation, q_3: SC protraction/retroaction, q_4: AC posterior/anterior tilt, q_5: AC downward/upward rotation, q_6: AC protraction/retroaction, q_7: GH axial rotation, q_8: GH addcution/abduction, q_9: GH flexion/extension, q_{10}: HU extension/flexion, q_{11}: RU pronation/supination. The humerus frame is shifted for better visualizations.

Dynamic model

Mass and inertial properties are attributed to the bone segments according to [14]. The upper extremity equations of motion are derived using the Lagrange's equations (Eq.

6.2).

$$\frac{d}{dt}\left(\frac{\partial \mathcal{L}}{\partial \dot{\boldsymbol{q}}}\right) - \frac{\partial \mathcal{L}}{\partial \boldsymbol{q}} = \frac{\partial \Omega}{\partial \dot{\boldsymbol{q}}} M + \lambda_{\mathrm{TS}} \frac{\Phi_{\mathrm{TS}}}{\partial \boldsymbol{q}} + \lambda_{\mathrm{AI}} \frac{\Phi_{\mathrm{AI}}}{\partial \boldsymbol{q}} \tag{6.2}$$

Where, $\mathcal{L}$ is the Lagrangian of the model obtained by adding all the bone segments Lagrangians [19, 254]. The $\frac{\partial \Omega}{\partial \dot{\boldsymbol{q}}} M$ is the generalized force vector. The Ω is a horizontal matrix including the angular velocities of all the bone segments. The vertical matrix M consists of the muscle resultant moments around each one of the five joints. The λ_{TS} and λ_{AI} are Lagrange multipliers associating to the scapula-thorax constraints. The generalized moment arms of the constraints are obtained by their jacobians ($\frac{\Phi_{\mathrm{TS}}}{\partial \boldsymbol{q}}$ and $\frac{\Phi_{\mathrm{AI}}}{\partial \boldsymbol{q}}$).

The matrix M can be written as $M = W\boldsymbol{f}$, where W is the moment arm matrix, and $\boldsymbol{f}$ is a vector consisting of the magnitudes of all the muscle forces. The W is obtained using its geometric definition and crosschecked with the tendon excursion method [112]. To this end, the muscles paths as massless elastic strings are approximated using the obstacle set method [111]. The origins/insertions, via points, and wrapping objects of 42 muscles spanning the upper extremity joints are defined from the MRI scans. They include subclavius, serratus anterior upper/middle/lower, trapezius C1-C6/C7/T1/T2-T7, levator scapulae, rhomboid minor/major T1-T2/major T3-T4, pectoralis minor/major clavicular/major sternal/major ribs, latisimuss dorsi thoracic/lumbar/Iliac, deltoid clavicular/acromial/scapular, supraspinatus, infraspinatus, subscapularis, teres minor/major, coracobrachialis, triceps brachii long/medial/lateral, biceps brachii short/long, brachialis, brachioradialis, supinator, pronator Teres, flexor carpi radialis/ulnaris, and extensor carpi radiali long/radialis bervis/ulnaris. Each muscle group of the model can be represented by up to 20 strings (Fig. 6.2a).

6.2.2 Measurements

EMG and motion data are recorded on the same subject for two activities (Fig. 6.2b): forward flexion in the sagittal plane and abduction in the frontal plane. Both activities are performed with 2 kg weight in hand and with a fully flexed elbow. Both activities are repeated for ten trials.

EMG signals of fifteen superficial muscles are measured at 1500 Hz sampling frequency using AgCl Kendall surface button EMG electrodes and are recorded by a 16 channel Desktop DTS system (Noraxon, Arizona, USA). The muscles include deltoid clavicular/acromial/scapular, trapezius C7/T1/T2-T7, pectoralis major sternal, infraspinatus, teres major, triceps brachii long/lateral, biceps brachii short/long, brachialis, and flexor carpi ulnaris. Maximum EMG values are also recorded by performing maximum voluntary contractions (MVC).

There exists no consensus in the literature for transforming the measured EMG signals to muscle excitations [236] (see Section 6.2.4). We follow a common approach in the literature [91]. It consists of high-pass filtering, rectifying, and consequently low-pass filtering the EMG signals. Eighth order zero-phase Butterworth filters are used. Their cut-off frequencies are set by residual analysis and are crosschecked with the harmonic analysis. The resulting EMG signals are normalized for each muscle using the maximum of its associated MVC signal. They are then partitioned per activity and per trial. Their means and standard deviations (σ_{EMG}) associating to the ten trials are obtained.

Trajectories of eleven palpable bony landmarks are measured by tracking their associating skin-fixed markers using an 8 camera VICON videogrammetry system (VICON, UK) at 100 Hz sampling frequency. The bony landmarks include incisura jugularis (IJ), processus xiphoideus (PX), 7th cervical vertebra (C7), 8th thoracic vertebra (T8), SC, AC, AA, EM, EL, radial styloid (RS), and ulnar styloid (US).

The recorded trajectories are low-passed filtered using an 8 order zero-phase Butterworth filter. Its cut-off frequency is obtained following the same procedures as the EMG signals. The resulting trajectories are partitioned for each activity and per trial. Then, their means corresponding to the ten trials are obtained.

6.2.3 Multi-segment optimization

The measured motion is reconstructed in terms of the generalized coordinates using multi-segment optimization. Given that GH is not a palpable bony landmark, it is missing from the measurements. Both TS and AI are also missing. Because, they are masked with thick layers of soft tissues and are not effectively trackable [156]. Therefore, a method developed in [248] is applied to estimate GH, TS, and AI trajectories. Then, multi-segment optimization is used to define the generalized coordinates ($\boldsymbol{q}_i$) for each frame of the measured motions (i) such that the overall distance between the measured markers ($\boldsymbol{x}_{e_j}$) and their corresponding bony landmarks ($\boldsymbol{x}_{m_j}$) is minimized, while satisfying the forward kinematics map (Eq. 6.3).

$$\begin{aligned} \min_{\boldsymbol{q}_i}. \quad & \textstyle\sum_j (\boldsymbol{x}_{m_{j,i}}(\boldsymbol{q}_i) - \boldsymbol{x}_{e_{j,i}})^T W (\boldsymbol{x}_{m_{j,i}}(\boldsymbol{q}_i) - \boldsymbol{x}_{e_{j,i}}) \\ \text{s.t.} \quad & \Phi_{\mathrm{TS}}(\boldsymbol{q}_i) = 0 \\ & \Phi_{\mathrm{AI}}(\boldsymbol{q}_i) = 0 \end{aligned} \tag{6.3}$$

Where, W is a weighting matrix.

Equation 6.3 is a nonlinear programming problem [230] that is solved by iterative

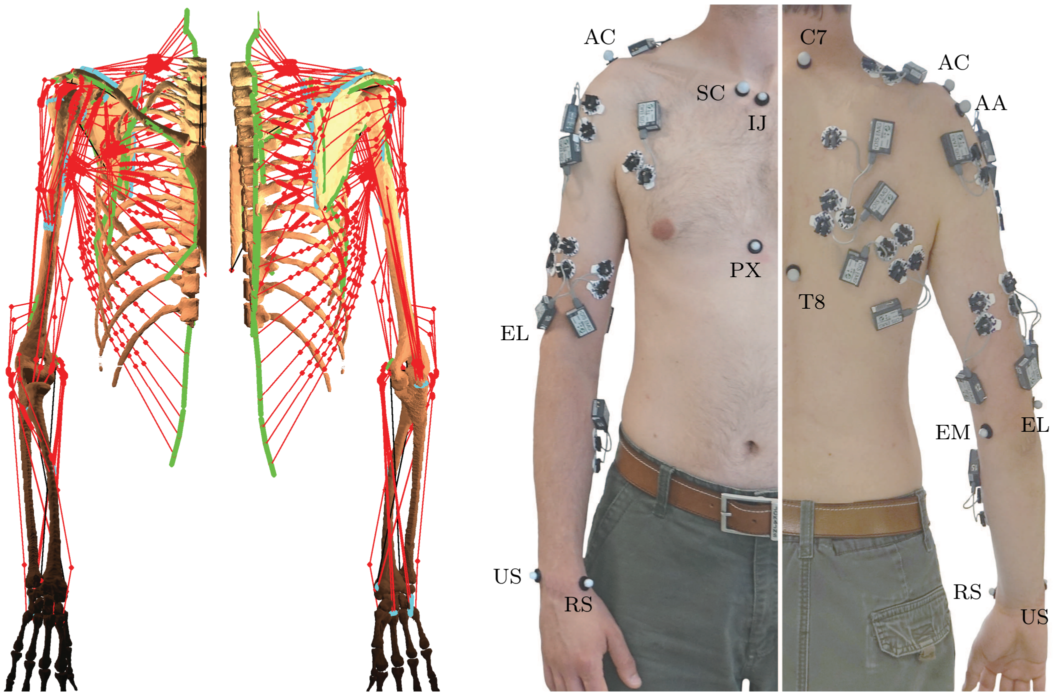

(a) (b)

Figure 6.2: (a) An illustration of the developed model. The model includes 42 muscles that each can be replicated by up to 20 strings (three strings are used in this illustration). (b) EMG and motion data are recorded for two activities. EMG signals of fifteen superficial muscles are measured. Trajectories of eleven skin-fixed markers are tracked.

numerical methods for each i after providing an initial guess for the $\boldsymbol{q}_i$. We use the function `fmincon` of Matlab (Mathworks, MA, USA) and consider $\boldsymbol{q}_{i=1} = \mathbf{0}$. The resulting $\boldsymbol{q}_{i-1}$ is used as an initial guess for $\boldsymbol{q}_i$.

6.2.4 Musculotendon model

A Hill-type musculotendon model is used to predict the muscle forces associating to the measured EMG signals. It provides force predictions for given muscle excitations ($u(t)$) and muscuoltendon lengths ($l^{\mathrm{MT}}(t)$) (Fig. 6.3) [171]. It consists of two unidirectional coupled dynamics, namely activation dynamics and contraction dynamics. The activation dynamics associate $u(t)$ to muscle activation ($a(t)$). The contraction dynamics account for the force reproductions for a given $a(t)$ and $l^{\mathrm{MT}}(t)$.

The means of normalized EMG signals are used as $u(t)$ for each muscle. The $a(t)$ represents the relative amount of calcium release to troponin in muscle fibers. It is obtained from a first order dynamic as follows [170].

$$\frac{da(t)}{dt} = \frac{u(t) - a(t)}{\tau(a(t), u(t))} \quad , \quad \tau(a(t), u(t)) = \begin{cases} \dfrac{\tau_{\mathrm{act}}}{0.5 + 1.5a(t)} & u(t) \leq a(t) \\ \dfrac{\tau_{\mathrm{dact}}}{0.5 + 1.5a(t)} & u(t) > a(t) \end{cases} \tag{6.4}$$

Where, τ_{act} and τ_{dact} are time constants corresponding to muscle activation and deactivation, respectively. Both $u(t)$ and $a(t)$ lie within [0 1].

The contraction dynamics consist of three elements replicating the force production of the musculotendon. A contractile element (CE) is considered to replicate active force productions of the muscle fiber. Passive forces generated by the muscle fiber during its elongation are modeled using a passive elastic element (PE) attached in parallel to the CE. An elastic element (EE) is also connected in series to the muscle fiber to replicate the tendon elongations. The contraction dynamics are derived from a force equilibrium between the muscle fiber and tendon. The following ordinary differential equation is an implicit form of the contraction dynamics [103].

$$\begin{aligned} F_{\mathrm{O}} \left[a(t) f^{\mathrm{L}}(\tilde{l}^{\mathrm{M}}) f^{\mathrm{V}}(\tfrac{l_{\mathrm{O}}^{\mathrm{M}}}{v_{\mathrm{O}}^{\mathrm{M}}} \dot{\tilde{l}}^{\mathrm{M}}) + f^{\mathrm{P}}(\tilde{l}^{\mathrm{M}}) \right] \sqrt{1 - \left(\tfrac{\sin \alpha_{\mathrm{O}}}{\tilde{l}^{\mathrm{M}}}\right)^2} \\ = F_{\mathrm{O}} f^{\mathrm{T}}(\tfrac{l^{\mathrm{MT}} - l_{\mathrm{O}}^{\mathrm{M}} \sqrt{\tilde{l}^{\mathrm{M}2} - \sin \alpha_{\mathrm{O}}{}^2}}{l_{\mathrm{S}}^{\mathrm{T}}}) \end{aligned} \tag{6.5}$$

Where, $f^{\mathrm{L}}(.)$, $f^{\mathrm{V}}(.)$, $f^{\mathrm{P}}(.)$, and $f^{\mathrm{T}}(.)$ are normalized functions associating to muscle force-length, muscle force-velocity, muscle passive force, and tendon force-length relationships. They are adapted from [103] by fitting smooth curves (C^{∞}) to experimental data. The maximum (optimum) muscle fiber force is denoted by F_{O}. The normalized muscle fiber length ($\tilde{l}^{\mathrm{M}}$) is obtained as $\frac{l^{\mathrm{M}}}{l_{\mathrm{O}}^{\mathrm{M}}}$ in which l^{M} and $l_{\mathrm{O}}^{\mathrm{M}}$ are the muscle fiber length and its optimum, respectively. The optimum muscle fiber velocity and the tendon slack length are denoted by $v_{\mathrm{O}}^{\mathrm{M}}$ and $l_{\mathrm{S}}^{\mathrm{T}}$, respectively. The $l_{\mathrm{O}}^{\mathrm{M}}$ and $v_{\mathrm{O}}^{\mathrm{M}}$ correspond to the situations when the muscle force-length and muscle force-velocity relationships are at maximum and zero force, respectively. Also, α_{O} is the pennation angle at $l_{\mathrm{O}}^{\mathrm{M}}$.

Equation 6.5 can be solved using implicit numerical integrators for $\tilde{l}^{\mathrm{M}}$ and consequently provides the tendon force $F_{\mathrm{T}}(t) = F_{\mathrm{O}} f^{\mathrm{T}}(.)$. To this end, $a(t)$, $l^{\mathrm{MT}}(t)$, the five musculotendon parameters (F_{O}, $l_{\mathrm{O}}^{\mathrm{M}}$, $v_{\mathrm{O}}^{\mathrm{M}}$, $l_{\mathrm{S}}^{\mathrm{T}}$, and α_{O}), and an initial condition $\tilde{l}^{\mathrm{M}}(t_0)$ are required. The $a(t)$ is readily obtained from Eq. 6.4. The $l^{\mathrm{MT}}(t)$ is calculated for each muscle using the musculoskeletal model. More specifically, the resulting $\boldsymbol{q}$ from the multi-segment optimization is fed into the model. The model defines the paths and consequently the lengths of musculotendons. We set the five musculotendon parameters according to [203].

A so-called initialization technique [103] is used to define $\tilde{l}^{\mathrm{M}}(t_0)$ such that the solution is devoid of artificial transients.

6.2.5 EMG-assisted load-sharing

The equations of motion (Eq. 6.2) provide eleven second order differential equations for the resulting generalized coordinates $\boldsymbol{q}$ obtained from the multi-segment optimization (Eq. 6.3). There are more unknowns (42 muscles times number of strings per muscle) than the number of equations. Therefore, we cast the following EALS to find an augmented muscle force vector $\tilde{\boldsymbol{f}}_i \equiv [\boldsymbol{f}_i^T \; \lambda_{\mathrm{TS}_i} \; \lambda_{\mathrm{AI}_i}]^T$ for each frame of the measured motions i.

$$
\begin{aligned}
\min_{\tilde{\boldsymbol{f}}_i} \quad & \tilde{\boldsymbol{f}}_i^T P \tilde{\boldsymbol{f}}_i \\
\text{s.t.} \quad & \frac{d}{dt}\left(\frac{\partial \mathcal{L}}{\partial \dot{\boldsymbol{q}}_i}\right) - \frac{\partial \mathcal{L}}{\partial \boldsymbol{q}_i} = \begin{bmatrix} \frac{\partial \Omega}{\partial \dot{\boldsymbol{q}}_i} W & \frac{\Phi_{\mathrm{TS}}}{\partial \boldsymbol{q}_i} & \frac{\Phi_{\mathrm{AI}}}{\partial \boldsymbol{q}_i} \end{bmatrix} \tilde{\boldsymbol{f}}_i \\
& \begin{cases} (1-\epsilon) F_{\mathrm{T}_{k,i}} \le \tilde{f}_k \le (1+\epsilon) F_{\mathrm{T}_{k,i}} & k \in D_{\mathrm{EMG}} \\ 0 \le \tilde{f}_k \le \tilde{f}_{\max_k} & \text{else} \end{cases} \\
& \boldsymbol{\psi}(\boldsymbol{q}_i,\ \dot{\boldsymbol{q}}_i,\ \ddot{\boldsymbol{q}}_i, \tilde{\boldsymbol{f}}_i) \le \boldsymbol{0}
\end{aligned}
\tag{6.6}
$$

Where, P is a diagonal matrix including the inverse squared of muscles physiological cross section areas (PCSA). The numerical values for PCSAs are set according to [203]. The cost function ($\tilde{\boldsymbol{f}}_i^T P \tilde{\boldsymbol{f}}_i$) is the sum of squared muscle stresses. The first constraint is the Eq. 6.2 whose right-hand side is written in a vectorial form. The second set of constraints is the muscle forces upper/lower bounds. The set D_{EMG} includes muscles with measured EMG signals. If the k^{th} muscle segment belongs to D_{EMG}, its tendon force predicted by the musculotendon model ($F_{\mathrm{T}_{k,i}}$) from the measured EMG is used as its upper/lower bounds. The positive coefficient ϵ defines the portion of $F_{\mathrm{T}_{k,i}}$ that is considered. The smallest ϵ that results in feasible solutions is considered. For muscles without measured EMG signals, 0 and $\tilde{f}_{\max_k} = K$ PCSA$_k$ are used as their lower and upper bounds, respectively. The constant K is the well-known Fick constant [206] and is equal to 33.011 Nm^{-2}. The stability constraint is denoted by $\boldsymbol{\psi}$ [19].

Equation 6.6 is a quadratic programming problem that can be solved using `quadprog` of Matlab. It defines $\tilde{\boldsymbol{f}}$ such that the sum of squared muscle stresses are minimized, while the constraints are satisfied. The incorporations of $F_{\mathrm{T}_{k,i}}$ shrink the feasible set of the problem. Therefore, more co-contractions can be expected to be predicted. An equivalent SLS can be obtained from Eq. 6.6 by setting $D_{\mathrm{EMG}} = \{\}$, that is only considering the second set of the upper/lower bounds constraints.

6.2.6 Evaluations of the model

The effects of inclusions of the measured EMG data in the EALS are evaluated on muscles forces, JRF, intersection foci of the JRF and the glenoid fossa, and a stability ratio comparing to the SLS. To this end, the two measured activities are simulated using the developed model and an equivalent SLS (Fig. 6.3).

A stability ratio (SR) is defined for the glenohumeral joint based on the intersection of the JRF and an ellipse approximating the fossa (Eq. 6.7). It quantifies the concentricity of the JRF with respect to the glenoid fossa. It is well-known that co-contractions increase the glenohumeral joint stability by centralizing the JRF within the fossa [67]. Therefore, the SR is linked to the GH joint stability obtained by co-contractions.

$$\mathrm{SR}_i = 1 - \left(\frac{d_{\mathrm{IS}i}}{a_{\mathrm{IS}}}\right)^2 - \left(\frac{d_{\mathrm{PA}i}}{a_{\mathrm{PA}}}\right)^2 \tag{6.7}$$

Where, a_{PA} and a_{IS} are posterior-anterior and inferior-superior radii of an ellipse that approximates the glenoid fossa. $d_{\mathrm{PA}i}$ and $d_{\mathrm{IS}i}$ are intersections of JRF and the glenoid fossa ellipse in posterior-anterior and inferior-superior directions for the i^{th} of the measured kinematics, respectively. The stability ratio lies within [0 1] with SR = 0 being marginal stability (intersection occurred on boundaries of the glenoid fossa ellipse), and SR=1 being a perfectly centered intersection.

The sensitivities of the resulting muscle forces and JRF with respect to $\pm 1\sigma_{\mathrm{EMG}}$ variations of the normalized EMG signals around their means are also defined. To this end, a first order approximation [227, 248] of the sensitivity of Eq. 6.6 with respect to $u(t)$ is calculated.

The results are presented per activity and in terms of the muscle forces, the JRF, intersection foci of JRF and the glenoid fossa, and the SR. The sensitivities of the muscle forces and the JRF are also presented. The results are illustrated along the arm flexion and abduction angles corresponding to the flexion and abduction activity, respectively. The associated results from the SLS are also presented. For the JRF, the corresponding *in vivo* measurements from [199] are also presented. Due to space limits, the complete set of muscle force predictions are left for the Appendix and only a subset of them are presented in Section 6.3.

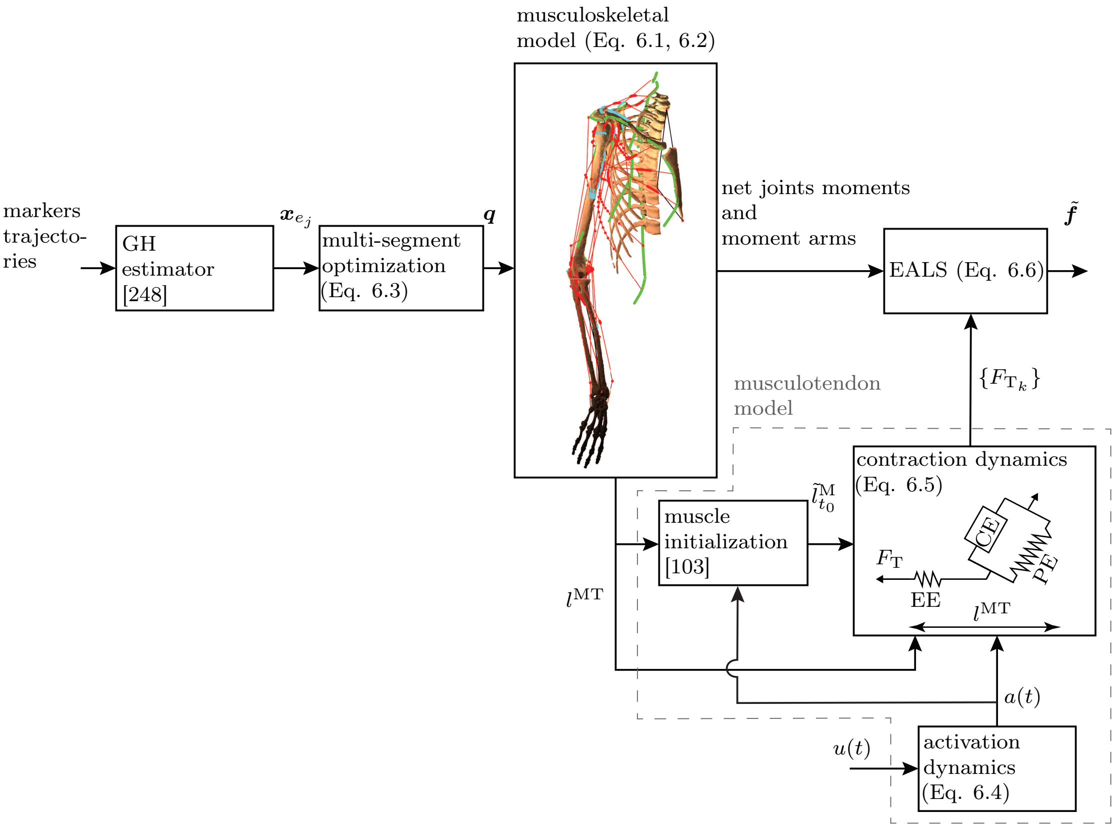

Figure 6.3: Markers trajectories are fed into the GH estimator. The resulting completed trajectories ($\boldsymbol{x}_{e_j}$) are used in the multi-segment optimization to find $\boldsymbol{q}$. The musculoskeletal model defines the net joints moments, moment arms, and l^MT. The musculotendon model consists of activation dynamics and contraction dynamics. The muscle initialization provides $\tilde{l}^\mathrm{M}_{t_0}$ for the contraction dynamics. The contraction dynamics include CE, PE, and EE. It reproduces the muscle forces associated to muscles with measured EMG ($\{F_{\mathrm{T}_k}\ \forall k \in D_\mathrm{EMG}\}$) for given $\tilde{l}^\mathrm{M}_{t_0}$, $a(t)$, and l^MT. The resulting F_{T_k} are used together with the net joints moments and moment arms in the EALS to predict $\tilde{\boldsymbol{f}}$.

6.3 Results

6.3.1 Muscle forces

Forward flexion in the sagittal plane: Serratus anterior lower and rhomboid major T1-T2 had 85% higher maximum forces in EALS than in SLS (Fig. 6.4a). EALS predicted less forces for trapezius (C7 and T2-T7). Instead, it predicted higher forces in rhomboid (minor and major T1-T2).

While SLS predicted no force for deltoid clavicular and scapular (except between 60° to 80° flexion), EALS predicted forces (higher than 52 N) for the entire movement. Deltoid acromial force followed similar patterns in EALS and SLS, but it was 30% higher initially in EALS. The highest muscle forces predicted in EALS were supraspinatus and deltoid acromial with 505 N at 70° flexion and 490 N at 50° flexion, respectively. Deltoid acromial had the highest sensitivity (around 25%) to variations of the normalized EMG.

The supraspinatus and subscapularis forces were substantially higher in EALS than SLS. Their maximums were almost 390% and 90% higher, respectively. The infraspinatus and teres minor forces were similar in EALS and SLS (less than 10% difference in their maximums).

EALS predicted more than 50 N force for triceps long and biceps long. However, SLS predicted only almost zero forces for them. Also, EALS predicted more than 180 N force for triceps lateral flexor carpi radialis against almost zero in SLS. Pronator teres and supinator produced above 100 N in EALS, whereas less than 40 N force for less than 15° flexion was predicted in SLS.

Abduction in the fontal plane: Serratus anterior lower and rhomboid minor had 100% and 200% higher maximum forces in EALS than in SLS (Fig. 6.4b).

Around 25 N and 55 N forces predicted for pectoralis major clavicular and sternal in EALS, respectively. However, SLS predicted 100 N and zero force for them, respectively. Teres major force was 200% higher in EALS than in SLS.

EALS predicted above 55 N force for deltoid clavicular, whereas SLS predicted almost zero force. Almost 145% higher force predicted by EALS for deltoid acromial in the beginning, although SLS prediction was 60% higher at the end of the motion. Both methods predicted very similar forces for deltoid scapular after 50° abduction (normalized root mean squared error > 0.024 and $p < 0.0001$). Subscapularis and deltoid acromial had the highest muscle forces predicted by EALS with 561 N at 76° and 445 N at 58°, respectively. Deltoid acromial also had the highest sensitivity to variations of the normalized EMG.

Higher maximum forces predicted by EALS for supraspinatus, infraspinatus, subscapularis, and teres minor comparing to SLS. For instance, the maximum subscapularis force was 22% higher in EALS.

EALS predicted above 90 N and 40 N forces for triceps long and biceps long, respectively. However, SLS predicted zero forces for them. On average around 200 N force was predicted by EALS for triceps lateral, flexor carpi radialis, supinator, and pronator teres. But, SLS predicted less than 30 N for them.

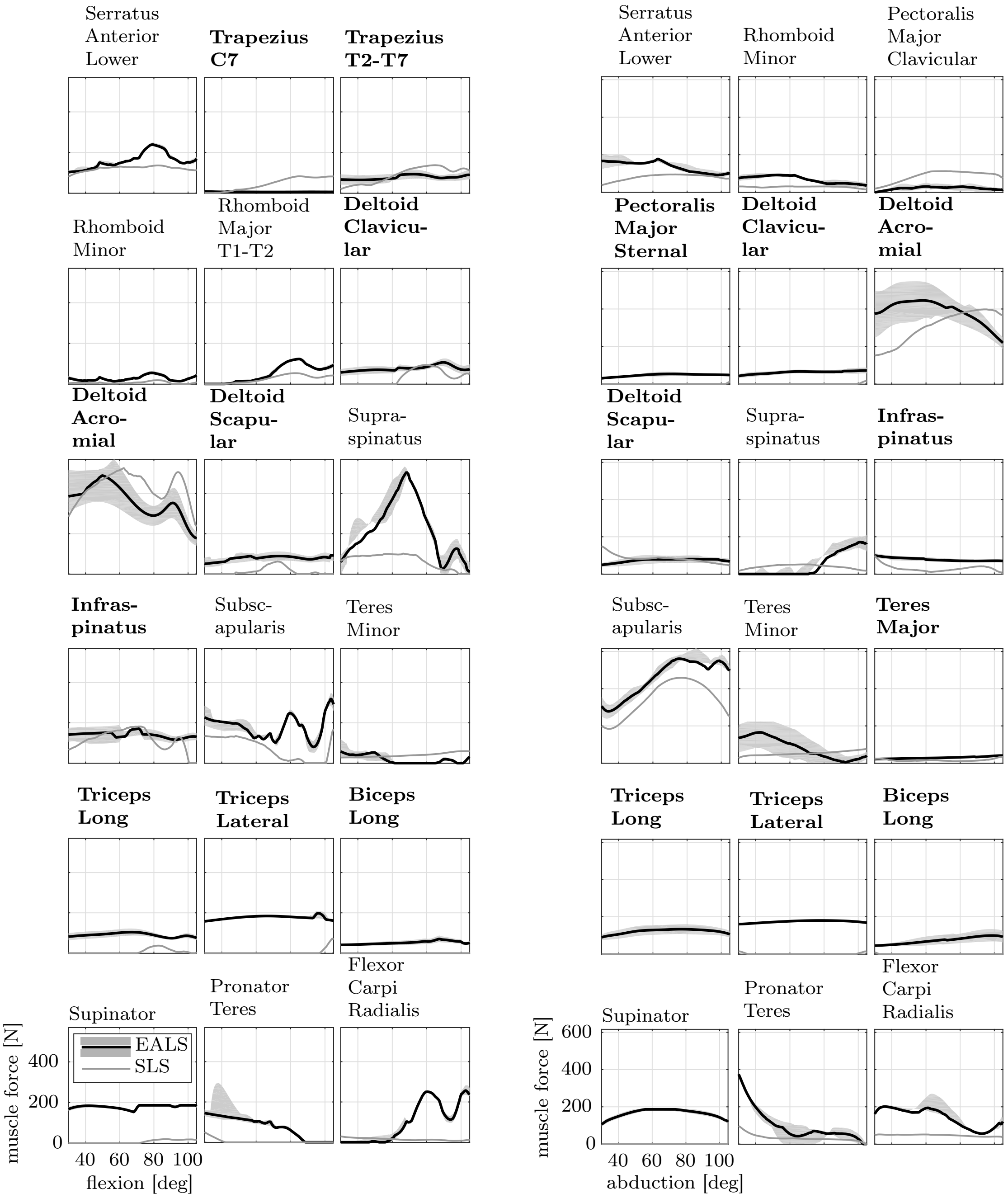

(a) (b)

Figure 6.4: Muscle forces predicted by EALS and SLS for (a) flexion and (b) abduction. The sensitivities to variations of normalized EMG signals were also depicted (gray shaded areas). Bold fonts were used to distinguish the muscles with measured EMG data. The predictions associated with all the 42 muscles were presented in the Appendix.

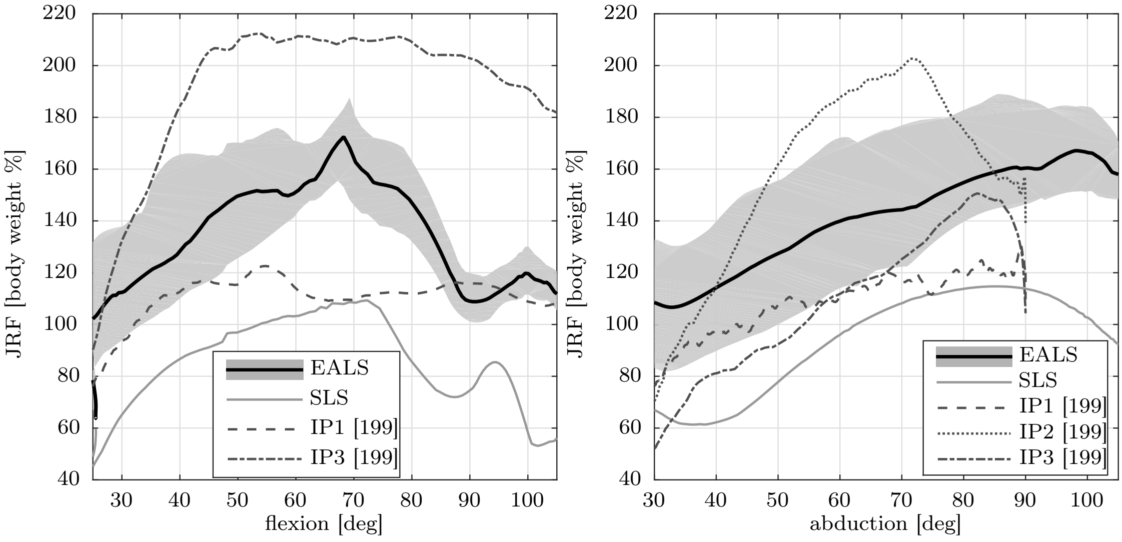

(a) (b)

Figure 6.5: JRF predicted by EALS and SLS along the corresponding *in vivo* data from [199], (a) flexion, (b) abduction. The sensitivities to variations of normalized EMG signals were also depicted (gray shaded areas).

6.3.2 JRF

The maximum JRF predictions by EALS were 58% and 46% higher comparing to SLS for both flexion and abduction motions, respectively (Fig. 6.5a and Fig. 6.5b). They were 172% and 167% of body weight (855 N) and occurred at 68° flexion and 98° abduction, respectively. The resulting JRFs had around 22% sensitivity to the variations of the normalized EMG signals.

6.3.3 SR and intersection foci

The SR was higher for EALS than SLS (more stable GH joint) and reached 0.87 (vs 0.56 for SLS) till the end of flexion (Fig. 6.6a). Intersection foci were more centric in EALS than SLS for both simulated motions (Fig. 6.6b and Fig. 6.6d). During flexion, the intersection foci started on the boundary of the fossa and moved towards center at 58° and 90° in EALS and SLS, respectively. The maximum SR was 46% less in abduction than in flexion according to EALS (Fig. 6.6c). During the abduction motion, the foci lied on the boundary throughout the motion for SLS, whereas in EALS it shifted toward the fossa center at 92°.

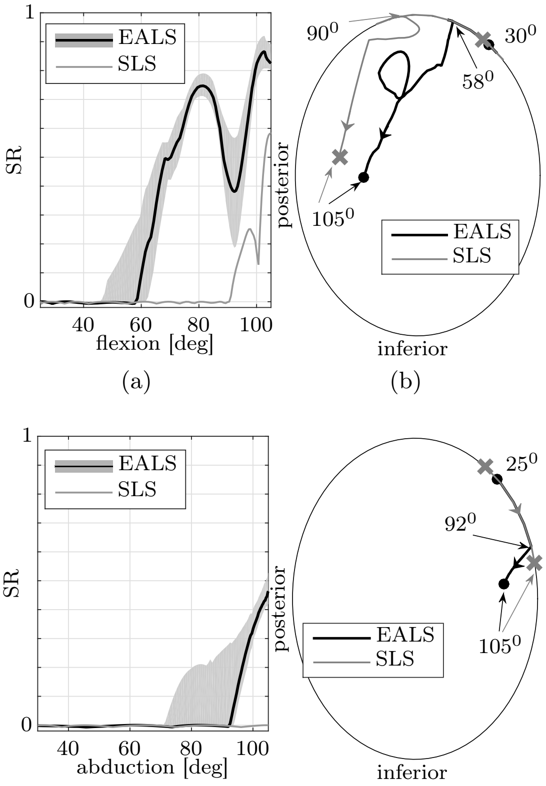

(a) (b)

(c) (d)

Figure 6.6: SR and intersection foci from EALS and SLS for (a,b) flexion, and (c,d) abduction, respectively. The sensitivities to variations of normalized EMG signals were also depicted (gray shaded areas). Cross and solid circle show both the beginning and end of the foci associated with EALS and SLS, respectively.

6.4 Discussion

The aim of this study was to test the hypothesis that EALS could better reproduce muscle co-contractions than the SLS. To this end, the EALS was developed by modifying the SLS of an upper extremity musculoskeletal model. The EALS was evaluated by comparing its muscles forces, JRF, SR, and intersection foci of JRF and the glenoid fossa with those of the equivalent SLS and *in vivo* measurements [199]. It predicted higher muscle co-contractions comparing to the SLS. The JRF was consequently higher comparing to SLS and was more consistent with the *in vivo* measurements.

During forward flexion, higher forces predicted for both serratus anterior lower and rhomboid major T1-T2 by EALS. This resulted in co-contractions around the AC joint. The higher force predicted for deltoid clavicular by EALS was coincide with a higher force from deltoid scapular. This was consistent with the previous findings regarding the antagonistic role of deltoid scapular during arm flexion [255]. Their co-contractions resulted in counterproductive moments around the GH joint. Also, higher forces predicted for triceps long and biceps long as antagonistic muscles. Their antagonistic role for the GH joint movements was reported [73]. According to EALS, muscles were also co-contracting around HU and RU joints, e.g. triceps lateral and flexor carpi radialis for the HU joint and supinator and pronator teres for the RU joint.

During abduction, similar co-contractions as those of flexion were predicted by EALS. Furthermore, pectoralis major sternal and teres major had higher forces in EALS, indicating their higher co-contractions. This co-contraction around the GH joint was consistent with previously studies [256].

Comparison of EALS and SLS muscle force predictions also illustrated shifts in contributions of muscle groups with similar roles. For instance, trapezius and rhomboid muscles could contribute in the scapular upward/downward rotation during flexion. But, EALS predicted more contributions from rhomboid minor/major T1-T2 and less from trapezius C7/T2-T7. The SLS predictions were contrary. During abduction, higher forces predicted for deltoid clavicular and less for deltoid acromial. It was commonly reported that SLS underestimated deltoid clavicular force [222]. Indeed, the use of subject's EMG data in terms of upper/lower bounds in EALS caused these shifts. Therefore, this could illustrate the potential of EALS in replicating inter-individual muscle recruitment patterns comparing to SLS. Certainly, more subjects and more activities must be evaluated by the model before EALS could be fully credited in this regard.

The JRF of EALS for both flexion and abduction activities lied within measurements from different patients with instrumented prosthesis (IP) [199]. However, SLS in general underestimated the JRF in both activities. The trends of the predicted JRF by EALS were in general consistent with the IP measurements, although it provided slightly higher predictions for the beginning of the motions. The sensitivities of the JRF to variations of the normalized EMG signals are consistent with those of muscles forces for EALS. It is worth noting that the IP measurements as means of validation should be used with cautious. Because, the post-surgery patients with IP had impaired musculotendons, and their motions were also compromised due to pain [28]. Therefore, their GH joint functions were expected to be different from our healthy subject.

The SR and intersection foci illustrated the effects of higher co-contractions of EALS on the GH joint stability. The higher co-contractions acted toward stabilizing the GH joint by centralizing the JRF within the glenoid ellipse. For the beginning of both activities the foci were on the boundary of the glenoid ellipse, indicating that the GH joint stability constraint was active. This was consistent with the previous studies regarding stability of the GH joint [31, 67]. However, in EALS the foci left the boundary toward more centralized positions at lower flexion and abduction angles. The SR indicated that the GH joint was more stable during the flexion than the abduction. Given that the humeral head was exposed to a higher portion of the fossa during flexion comparing to abduction

[131], this result was physiologically coherent.

Portions of muscles forces reproduced by the musculotendon model were used in EALS as upper/lower bounds. These portions were defined by the positive coefficient ϵ. The choice of ϵ could obviously alter the force predictions. Smaller values for ϵ resulted in tighter bounds for force predictions of muscles with EMG data. Therefore, the feasible set of the EALS was shrunk further comparing to larger values of ϵ. Consequently, higher co-contractions could be predicted. However, the physiological coherence of the resulting co-contractions required further investigations. Furthermore, smaller ϵ might cause infeasible solutions for the EALS. In these situations larger ϵ had to be used. We chose the smallest ϵ that resulted in feasible solutions during both activities (0.03 and 0.07 for flexion and abduction, respectively).

This study had a number of limitations. A major limitation was that only one subject participated. More subjects would be required to more thoroughly evaluate the model, specially its performance in replicating inter-individual muscle recruitment patterns. Three patients with instrumented prosthesis were considered to find the best combination of EMG signals during forward flexion and abduction [43]. The second limitation was about the musculotendon parameters. The musculotendon model reproduced forces based on normalized EMG and musculotendon lengths. It also required five musculotendon parameters for each muscle. We set these parameters according to [203]. The realism of the reproduced forces could be enhanced if these parameters were personalized to our subject. However, it is not yet straightforward to obtain these parameters. A sensitivity analysis could be performed to evaluate the effects of these parameters on the reproduced forces. Provided the effects of each parameter, special attentions could then be paid to personalize the parameters with the most significant effects and the widest variabilities. The third limitation was that the effects of fatigue [250] and temperature [251] were not considered in our musculotendon model. However, we paid special attentions to provide sufficient resting intervals for the participant. If necessary, the effects of fatigue could be readily included in our model by linearly scaling the F_{O} with simulation time [252]. Another limitation referred to the fact that a same musculotendon type was considered for all the fifteen musculotendons with EMG data. However, there were several musculotendon types in the upper extremity, including fast and slow twitch muscles [203]. Considering the musculotendon types required individualizing more parameters for each muscle, which was not feasible. Another limitation was that only two activities were considered. This imposed certain limitations ahead of generalizing our results. Future applications of the model should consider more activities, including activities of daily living (ADL). This could provide useful information about normal loading conditions of the GH joint. Provided this, specific activities could be pre/proscribed for specific shoulder pathologies.

In conclusion, we verified that the EALS better predicted muscle co-contractions in an upper extremity musculoskeletal model. It predicted co-contractions by incorporating fifteen EMG-based muscles forces obtained from a musculotendon model. The incorporation of the EMG-based muscles forces shrank the feasible set of the EALS and therefore more co-contractions could be predicted comparing to the SLS. The JRF predictions better matched *in vivo* measurements. This conclusion should be confirmed with movements of daily living and could be applied to answer clinical related questions, such as treatment and rehabilitation of GH joint osteoarthritis.

Appendix: Muscles forces

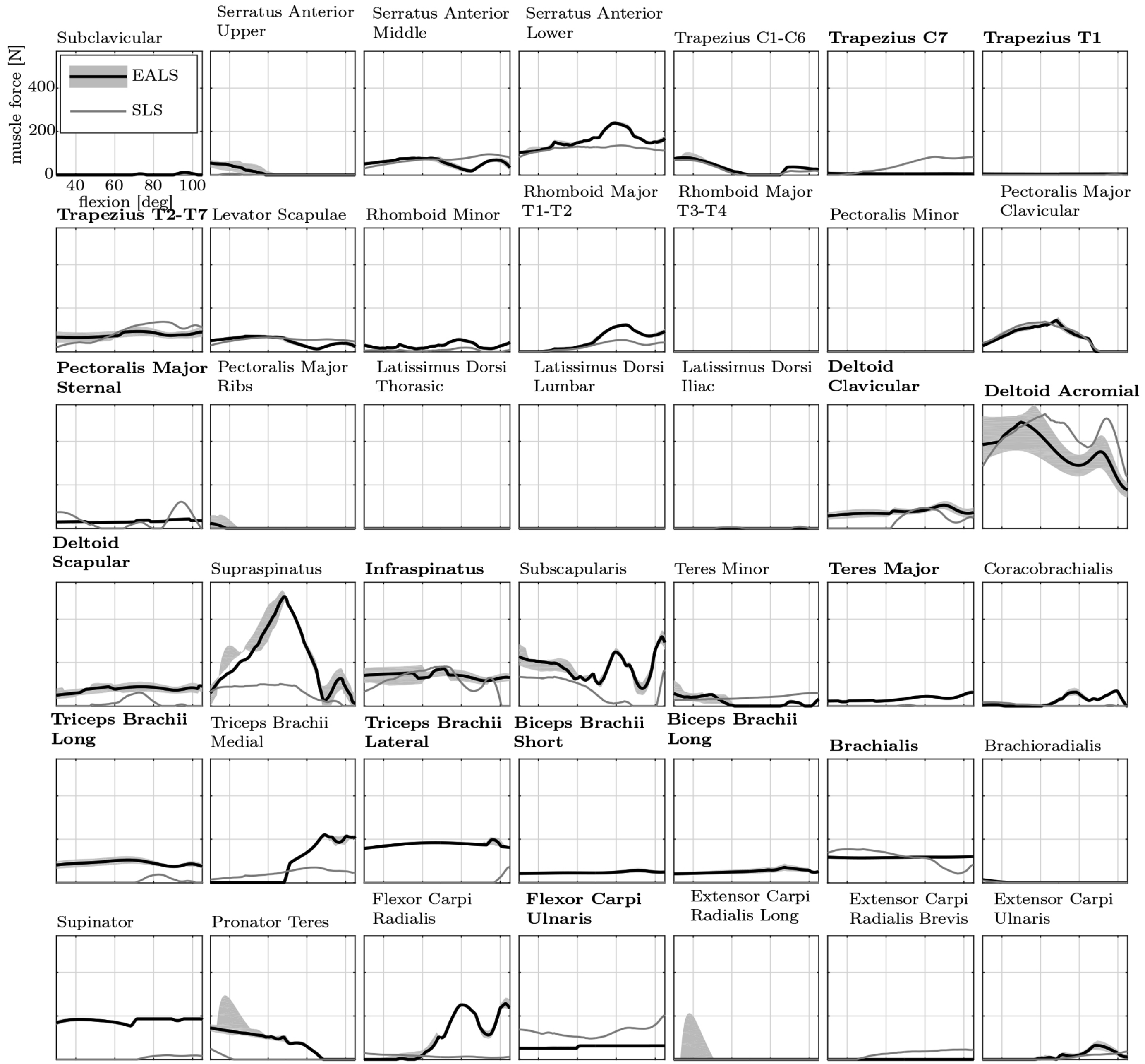

Figure 6.7: Muscle forces predicted by EALS and SLS for flexion. The sensitivities to variations of normalized EMG signals were also depicted (gray shaded areas). Bold fonts were used to distinguish the muscles with measured EMG data.

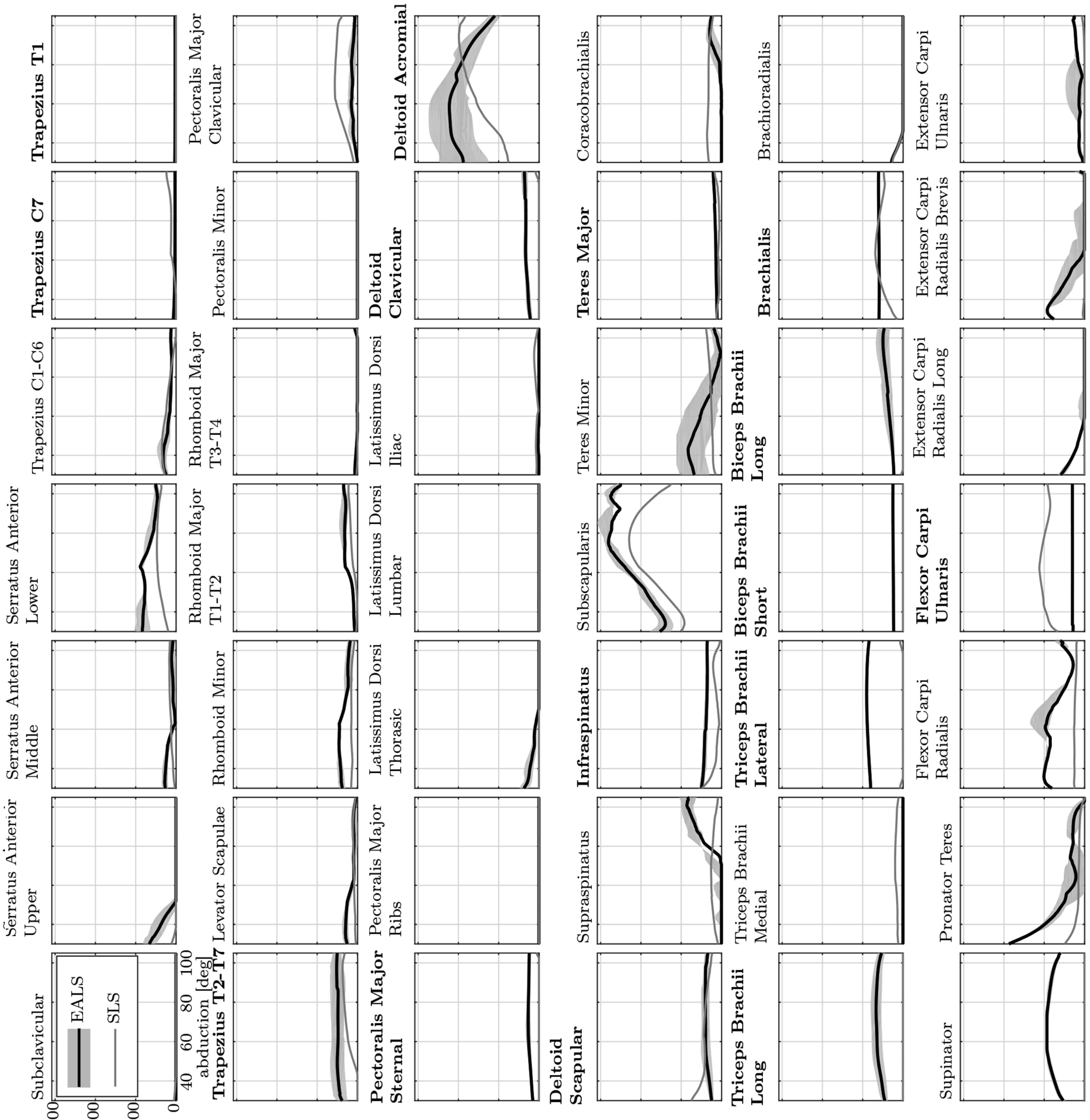

Figure 6.8: Muscle forces predicted by EALS and SLS for abduction. The sensitivities to variations of normalized EMG signals were also depicted (gray shaded areas). Bold fonts were used to distinguish the muscles with measured EMG data.

7 Conclusions

7.1 Summary

The aim of this thesis was to extend an existing shoulder musculoskeletal model [19] for patient-specific clinical applications. To this end, number of improvements were considered that were detailed in chapters 2 to 6.

The elbow and the muscle groups spanning it were included in the shoulder model. The bone morphologies of the ulna and the radius and muscles origins/insertions were obtained from MRI scans. The elbow was modeled using two non-perpendicular hinge joints. Two DOFs for flexion/extension and pronation/supination were considered.

Scaling routines were developed to scale model's bone segment inertial properties, skeletal morphologies, and muscles architectures according to any specific subjects. The model was also presented as a Matlab toolbox with a graphical user interface. The effects of anthropometric parameters, including subject's gender, height, weight, glenoid inclination, and degenerations of rotator cuff muscles on the glenohumeral (GH) joint reaction force (JRF) predictions were evaluated.

A framework was developed that allowed forward-dynamics simulation of the model. Six DOFs were considered for the GH joint, including its translations and rotations. A deformable articular contact was included in the framework defining the GH joint contact force in terms of the joint rotations and translations. The framework provided a straightforward solution for estimations of the humeral head translations (HHT).

Videogrammetry-based measured motions of the upper extremity were reconstructed in the absence of scapula kinematics measurement-devices. A method was developed that estimated the GH joint center and consequently scapula configurations based on trajectories of few markers and an MRI scan of each subject's glenohumeral joint. Multi-segment optimization was used to reconstruct the measured activities that was completed by the developed estimation method.

An initialization technique was developed for a Hill-type musculotendon model by performing singular perturbation analysis. It provided initial conditions for the developed Hill-type model such that the resulting force reproductions were devoid of artificial transients.

The standard load-sharing (SLS) scheme of the model was modified such that measured electromyography (EMG) data could be incorporated in the model. It was hypothesized that inclusions of the measured EMG could improve model predictions of muscle co-contractions and consequently its JRF predictions. The hypothesis was confirmed by evaluating the modified load-sharing (EALS) during measured activities.

7.2 General discussion

Several studies reported the importance of the elbow on shoulder kinematics, e.g. [42, 69]. Biceps and triceps were shown to play a crucial role in the stability of the GH joint [67, 73]. However, given the complex multiple DOF kinematics of the elbow, there was no consensus in the literature concerning its modeling [50, 69]. Variety of approaches existed from very simplistic cardanic joints [74] to complex closed-kinematic chains [83]. A majority of the available shoulder musculoskeletal models [12–14, 17, 46, 47] followed the ISB recommendations for modeling the elbow [201]. Therefore, they only considered a single segment for both the ulna and the radius. Furthermore, ISB recommendations for the elbow bone-fixed frame resulted in non-physiological configurations of the forearm relative to humerus [202]. In this thesis both the ulna and the radius were considered to model the elbow. This was shown to help better represent the elbow and the interplay between the ulna and the radius [80]. Reference configurations were also defined in this thesis. Therefore, inherent alignment of the ulna and the radius bone-fixed frames were not required, despite the ISB recommendations.

Indeed, a few numbers of the available shoulder musculoskeletal models allow scaling the models to any specific subjects, e.g. [42, 210, 211]. Body segments inertial properties (BSIP) were commonly scaled using predictive equations [89–91]. However, these predictive equations required further adjustments to accurately scale BSIP in the 3D space. In this thesis predictive equations of [93, 94] were used which were adjusted by [95] to provide 3D applicable predictive equations to scale BSIP. Skeletal morphologies were commonly scaled using isotropic scaling factors [16, 42, 97] in order to avoid infeasible kinematics [96]. However, this implied an unrealistic uniform scaling between different individuals [89]. In this thesis, infeasible kinematics were linked to the scaling of the ribcage ellipsoids. Therefore, a method was developed to scale the ribcage ellipsoids that provided consistent positions of the scapula with respect to the thorax. It allowed applications of anisotropic scaling factors and also having feasible kinematics. Several studies reported the effects of glenoid inclination/version on model force predictions and joint translations [64, 101, 193, 200]. However, the available models did not allow adapting them to specific subjects. A method was developed in this thesis adapting the glenoid inclination/version to specific subjects. The effects of these adaptations were shown to be considerable, specially during lower degrees of arm abductions. Scaling the wrapping objects was not addressed at least explicitly in the available models. However, the wrapping objects could considerably alter muscle moment arms and model force predictions [111, 112]. Therefore, the wrapping objects were also scaled using anisotropic scaling factors in this thesis. The body mass index (BMI) [115] was commonly used to scale muscles physiological cross section areas (PCSA) [42]. But, direct association of the BMI to PCSA was arguable [116]. Therefore, in this thesis a predictive equation [117] was used that defined muscle percentage of the body composition. The developed scaled-generic model was evaluated by investigating the effects of subject's gender, height, weight, glenoid inclination, and PCSAs of rotator cuff muscles on the JRF predictions. This typically required participants with different anthropometric parameters [88]. For instance, to evaluate the effect of height, several participants with different heights but ideally same weights were required [86]. Their kinematics must be first recorded and then models would be used to predict JRFs. This procedure might be lengthly and expensive. Its outcome might also be subject to uncertainties associating to kinematic measurements. However, a strength of the model developed in this thesis was that it allowed performing the parameter study, while no participants was required. Because, the model could numerically produce the kinematics associated to each virtual subject considered [100].

The model was developed as a Matlab toolbox with a graphical user interface (GUI). The GUI would facilitate its clinical applications by exempting users from further programmings. To the best of my knowledge, this is the first and the only available Matlab toolbox for shoulder and elbow musculoskeletal modeling.

The framework developed in this thesis provided a straightforward solution for estimation of the HHT. It allowed forward-dynamics simulation of the model and considered a deformable articular contact between the humeral head and the glenoid fossa. It allowed solving the differential equations of motion of the model with a six DOF GH joint. Therefore, the dynamic effects of motion were naturally included in the translations predicted. The first and second derivatives of the translational DOFs were neglected in the previous studies (e.g. [119, 122, 124]) in order to transform the differential equations of motion to a set of algebraic equations. The deformable articular contact was developed by considering a viscoelastic contact model. This was more physiologically consistent comparing to an elastic potential function used in [135]. The elastic potential function did not account for the moment applied on the humerus due to the articular contact. The developed framework incorporated a representation of the cartilage contact mechanics into the musculoskeletal model. It therefore provided an integrated solution to study the relationship between joint kinematics, muscle forces, and cartilage stress. Indeed, the common approach in the literature consists of two steps. First a musculoskeletal model is used to define the rotational joint kinematics as well as the muscle forces. Then, a finite element analysis is performed to define the translational joint kinematics and the cartilage stress [119, 121, 124, 125].

The common approach in the literature for motion reconstructions using videogrammetry systems requires scapula kinematics measurement-devices (SKMD) [91]. The SKMD defines the scapula kinematics from which the GH joint center would be estimated using either formal methods [144–149] or predictive methods [150, 151, 153]. However, applications of SKMD are neither straightforward [154] nor always noninvasive [157]. Therefore, in this thesis an inverse approach comparing to the common approach was used. A method was proposed to provide estimations of the GH joint center. Then, the scapula configurations would be obtained based on the resulting GH joint center estimations. This facilitated motion reconstructions in the upper extremity by lifting the dependency on SKMD. Indeed, there existed a predictive method [152] that allowed estimations of the GH joint center independent of the scapula configurations. However, its accuracy dropped significantly during arm motions [147, 152]. Given that the developed method in this thesis accounted for the soft tissue artifacts, it provided practical predictions throughout the arm motion.

The multi-segment optimization was solved for joints angles in each frame of the measured data. Therefore, there was no guarantee that the resulting joints angles were continuous. Continuity of the resulting joints angles is an essential attribute if they are going to be used in inverse dynamics for muscle force predictions [193, 234]. Therefore, the resulting joints angles are commonly smoothened by fitting continuous curves (often polynomials) [50, 142]. The downside of this approach is that the resulting continuous curves might not satisfy the kinematic constraints of the forward kinematic map. Therefore, I examined an alternative approach to directly define continuous joints angles, while they were satisfying the kinematic constraints of the forward kinematic map. I first parametrized the joints angles by continuous functions (8th degree piecewise polynomials). Then, the multi-segment optimization was solved to define the unknown coefficients of these continuous polynomials. The primary results showed that the method resulted in continuous polynomials that satisfied the kinematic constraints. However, the inter-sample behavior of the resulting joints angles (the behavior between two consequent data frame) was not acceptable. Furthermore, the method was computationally inefficient even for very simple trajectories. Although I did not succeed in bringing this approach to practice, further exploration of this method is required for a definite conclusion regarding its performance.

Indeed, a few initialization techniques existed for Hill-type musculotendon models [180, 184]. However, their provided initializations were subject to singularities of the relative stiffness of muscle fibers and tendons. Furthermore, they might lack biophysical correspondence [178]. The initialization technique developed in this thesis was devoid of numerical singularities. It also possessed biophysical correspondence, given that no extra assumptions was considered in its development. It reproduced forces that were in an excellent agreement with the *in vivo* measurements [183]. The normalized functions used to develop the Hill-type model were obtained by fitting smooth curves to a large data set of experimental data reported by [7, 170, 173, 178, 182, 183, 237–244]. Provided this and given the rigorous mathematical formulations used, the developed model could be regenerated by others. Although, Hill-type models were extensively used in simulations of coordinated movements [21, 43], their rigorous mathematical representations are rare in the literature.

Few studies investigated effects of inclusions of EMG data on muscle co-contractions in the upper extremity [43, 188, 196–198]. However, the relationship between predicted muscle forces and measured EMG data was over-simplified [188, 196–198]. This deviated from the nonlinear dynamical behavior of musculotendons [170]. The net moments produced by direct applications of measured EMG also failed to satisfy the equilibrium equations [188, 196, 197]. Therefore, the predicted co-contractions might lack a physiological correspondence. In contrast to these studies, the developed EALS scheme of this thesis used the musculotendon model that was separately validated in Chapter 5. The equilibrium equations were also naturally satisfied by solving the developed EALS scheme. I showed that inclusions of the EMG data would improve predictions of muscle co-contractions. The EMG-based muscle forces used as upper/lower bounds shrank the feasible set of the EALS. Therefore, EALS would have to find the optimal solution in a smaller set of possible muscle forces. The more this feasible set was shrunk the more accurate the muscle co-contractions would be predicted. The EMG data of fifteen muscles were used in the developed EALS, while the maximum reported number was four [43].

There were two main constraints against thorough validations of the model. First, access to golden validation standards [28] was not granted during this thesis. For instance, the shoulder instrumented prosthesis (IP) [199] was commonly considered as a golden standard for JRF validation. The JRF data from IP were available online for several activities. A rigorous validation of the model JRF required not only the JRF but also at least the associated kinematics and EMG data of the patients. The associated kinematics and EMG data would be used to reproduce the JRF through inverse-dynamics. Further information about the IP patients such as their BSIP, muscles architectures, glenoid inclination/version, and skeletal morphologies would improve the rigor of the validation.

Despite the lack of access to the golden validation standards, several attempts were made in this thesis to directly or indirectly validate the model itself and its subsystems. For instance, in Chapter 3, the JRF predictions during abduction in the scapula plane was compared to previous numerical studies and IP measurements [199]. The same approach was used for the resulting HHT. The golden standard for HHT was a 3D tracking of the GH joint center using biplane X-ray images [8]. In Chapter 4, the scapula kinematics were compared to *in vivo* measurements [138, 139] during slow abduction in the frontal plane. The scapula kinematics were well-known to have considerable effects on the JRF and HHT [98]. The golden standard for tracking the scapula was a transcortical pin placed into the scapula [139]. The musculotendon model as a subsystem of the model was also validated against *in vivo* measurements [183] by reproducing experimentally measured forces. The JRF predictions associating to abduction and forward flexion with 2 kg weight in hand were also compared to IP measurements [199] in Chapter 6.

Second, there were either limitations concerning the available golden validation standards or it was a lack of validation standard in the literature. For instance, the post-surgery patients of IP had compromised motions due to pain, and their musculotendon and joint structure were impaired due to the invasive surgery. Therefore, their joint kinematics and mechanics were expected to be different than the healthy subject of the model. Furthermore, the accuracy of the biplane X-ray images for measuring the HHT was limited by the inaccuracies of its image processing algorithms. On the other hand, given that it was not possible to measure the muscle forces non-invasively, there was a lack of validation standard for muscle force predictions [185]. In these situations, applications of parameter studies and sensitivity analyses were justified to verify the model. In Chapter 1, I indirectly verified the model by evaluating the effects of subject specific parameters, including gender, height, and weight. In Chapter 4, the sensitivities of the joint angle predictions to variations in measured trajectories were analyzed.

7.3 Perspectives

Model validations: The developed model provided useful predictions of muscles forces, JRF, and HHT. However, the main barrier ahead of its wide spread clinical applications was the lack of rigorous and comprehensive validation. This could be an important direction for future improvement. Profound sensitivity analyses could also help evaluate the model. They quantify effects of different model parameters on the model outcomes [207]. For instance, the developed EALS used five musculotendon parameters for each of the fifteen muscles with EMG data. The parameters were set according to the literature [203]. A sensitivity analysis could evaluate effects of these parameters and specify the most influential ones. Provided this, more attention could be paid to measure and personalize the most influential parameters [257], if they also had high variabilities.

Model evaluations: Three movements were considered throughout this thesis, including abductions in the scapula and frontal planes and forward flexion in the sagittal plane. However, evaluations of more movements would be fruitful at least in two ways. First, it would help verify the behavior of the model and its subsystems during other movements. For instance, the muscles paths were verified visually during the three movements considered. This would be necessary for other activities in order to avoid unexpected surprises during possible clinical applications of the model. Second, evaluations of the model during different movements, including activities of daily living could provide a useful database on the joint kinematics and kinetics [258]. Provided this, specific movements could be pre/proscribed for specific shoulder pathologies. This would therefore open a door toward improving subject-specific rehabilitation techniques [259]. On the other hand, only one subject was considered in this thesis. More subjects would be required to evaluate the model predictions, specially its ability to replicate inter-individual variabilities.

Ambulatory motion reconstructions: A viodegrammetry system that tracked skin-fixed markers was used for motion reconstructions. However, there were limitations concerning clinical applications of videogrammetry systems. For instance, they were in general costly and complex. It was also too cumbersome to set up them in small areas, such as a therapist's office. Given the dependency of the model on kinematics data [92], its clinical applications would require an ambulatory approach for motion tracking. To this end, a method that did not require measured data was included in the model [100]. Given that it required several trial and errors to replicate a motion, it would not be clinically practical. Inertial and magnetic measurement systems were recently used for motion tracking in the upper extremity [260]. They did not have the recurrent limitations of the videogrammetry sytsems. Therefore, they could be diffused with the developed kinematic model to reconstruct the motion in more ambulatory settings.

Clinical applications: A major limitation concerning clinical applications of the model was that only one healthy subject was considered. Future applications of the model should include a higher number of subjects including healthy and with shoulder pathologies. The initial steps toward this direction were taken. Cohort of patients from pre/post operative total shoulder arthroplasty was collected [205]. The developed EMG-assisted scaled-generic model could be adapted to these subjects to predict muscle and joint forces. The outcome could be translated for answering clinical questions for improving treatment and rehabilitation techniques of GH joint osteoarthritis [62, 137].

Goal-directed simulations: An important direction for future developments would be goal-directed simulations of the model. In goal-directed simulations, trajectories or initial and final positions of the hand as the upper extremity end-effector are used as the model inputs. Muscle activation patterns are the model outputs. It would require an inverse-kinematics formulation to calculate optimal joints angles for given trajectories of the hand. Given the kinematic redundancy of the upper extremity, this would be a challenging task [261]. It would also require forward-dynamics simulations to define for instance time optimal and physiological muscle activations pattern. Although, a forward-dynamics framework was developed in Chapter 3, further developments would be required to incorporate it in goal-directed simulations. The developed forward-dynamics framework was based on inversion control. Given that the inertial matrix of the system might become ill-conditioned, inversion control would result in unreasonable muscle activation patterns [262]. Furthermore, the musculotendon dynamics were not considered in the developed forward-dynamics framework. Inclusion of the musculotendon dynamics would transform the optimal load-sharing to a dynamic optimization problem [263]. Given that solving dynamics optimization problem would require several times integration of the systems's equations of motion [264], it would therefore become immediately computationally demanding [218]. Nevertheless, goal-directed simulations of the upper extremity musculoskeletal models would open a new door toward their cross-disciplinary applications. For instance, they could be used for systematically calculating muscle activation patterns for upper extremity exoskeletons and neuroprosthetic systems [47].

Bibliography

[1] J. A. Haagsma, N. Graetz, I. Bolliger, M. Naghavi, H. Higashi, E. C. Mullany, S. F. Abera, J. P. Abraham, K. Adofo, U. Alsharif, et al., The global burden of injury: incidence, mortality, disability-adjusted life years and time trends from the global burden of disease study 2013, Injury prevention 22 (1) (2016) 3–18.

[2] C. J. Murray, J. Abraham, M. K. Ali, M. Alvarado, C. Atkinson, L. M. Baddour, D. H. Bartels, E. J. Benjamin, K. Bhalla, G. Birbeck, et al., The state of us health, 1990-2010: burden of diseases, injuries, and risk factors, Jama 310 (6) (2013) 591–606.

[3] J. S. Day, E. Lau, K. L. Ong, G. R. Williams, M. L. Ramsey, S. M. Kurtz, Prevalence and projections of total shoulder and elbow arthroplasty in the united states to 2015, Journal of shoulder and elbow surgery 19 (8) (2010) 1115–1120.

[4] A. G. Cutti, E. K. Chadwick, Shoulder biomechanics and the success of translational research (2014).

[5] M. Masjedi, A. Kontaxis, S. Lawson, G. Johnson, Effect of bayley-walker and delta implants on the deltoid muscle moment arm, Journal of Biomechanics 40 (2007) S151.

[6] A. Terrier, P. Büchler, A. Farron, Influence of glenohumeral conformity on glenoid stresses after total shoulder arthroplasty, Journal of shoulder and elbow surgery 15 (4) (2006) 515–520.

[7] C. N. Maganaris, J. P. Paul, Tensile properties of the in vivo human gastrocnemius tendon, J Biomech 35 (12) (2002) 1639–46.

[8] C. Zhang, W. Skalli, P.-Y. Lagacé, F. Billuart, X. Ohl, T. Cresson, N. J. Bureau, D. M. Rouleau, A. Roy, P. Tétreault, et al., Investigation of 3d glenohumeral displacements from 3d reconstruction using biplane x-ray images: Accuracy and reproducibility of the technique and preliminary analysis in rotator cuff tear patients, Journal of Electromyography and Kinesiology.

[9] B. Bolsterlee, D. H. Veeger, E. K. Chadwick, Clinical applications of musculoskeletal modelling for the shoulder and upper limb, Medical & biological engineering & computing 51 (9) (2013) 953–963.

[10] M. W. Spong, S. Hutchinson, M. Vidyasagar, et al., Robot modeling and control, Vol. 3, Wiley New York, 2006.

[11] H. Baruh, Analytical dynamics, WCB/McGraw-Hill Boston, 1999.

[12] D. Karlsson, B. Peterson, Towards a model for force predictions in the human shoulder, Journal of biomechanics 25 (2) (1992) 189–199.

[13] A. A. Nikooyan, H. Veeger, E. Chadwick, M. Praagman, F. C. van der Helm, Development of a comprehensive musculoskeletal model of the shoulder and elbow, Medical & biological engineering & computing 49 (12) (2011) 1425–1435.

[14] B. A. Garner, M. G. Pandy, Musculoskeletal model of the upper limb based on the visible human male dataset, Computer methods in biomechanics and biomedical engineering 4 (2) (2001) 93–126.

[15] N. Lindsay, Modelling of the Shoulder Mechanism: A Report Describing the Development of a Three-dimensional Biomechanical Model of the Human Shoulder Complex, Institute of Mechanical Engineering, Aalborg University, 2001.

[16] I. W. Charlton, G. Johnson, A model for the prediction of the forces at the glenohumeral joint, Proceedings of the Institution of Mechanical Engineers, Part H: Journal of Engineering in Medicine 220 (8) (2006) 801–812.

[17] C. Quental, J. Folgado, J. Ambrósio, J. Monteiro, A multibody biomechanical model of the upper limb including the shoulder girdle, Multibody System Dynamics 28 (1-2) (2012) 83–108.

[18] P. Favre, A model to study active shoulder motion and stability, Ph.D. thesis, Eth Zurich (2011).

[19] D. Ingram, Musculoskeletal model of the human shoulder for joint force estimation, Ph.D. thesis (2015).

[20] S. L. Delp, J. P. Loan, M. G. Hoy, F. E. Zajac, E. L. Topp, J. M. Rosen, An interactive graphics-based model of the lower extremity to study orthopaedic surgical procedures, IEEE Transactions on Biomedical engineering 37 (8) (1990) 757–767.

[21] D. G. Lloyd, T. F. Besier, An emg-driven musculoskeletal model to estimate muscle forces and knee joint moments in vivo, Journal of biomechanics 36 (6) (2003) 765–776.

[22] E. M. Arnold, S. R. Ward, R. L. Lieber, S. L. Delp, A model of the lower limb for analysis of human movement, Annals of biomedical engineering 38 (2) (2010) 269–279.

[23] M. G. Hoy, F. E. Zajac, M. E. Gordon, A musculoskeletal model of the human lower extremity: the effect of muscle, tendon, and moment arm on the moment-angle relationship of musculotendon actuators at the hip, knee, and ankle, Journal of biomechanics 23 (2) (1990) 157–169.

[24] F. Moissenet, L. Chèze, R. Dumas, A 3d lower limb musculoskeletal model for simultaneous estimation of musculo-tendon, joint contact, ligament and bone forces during gait, Journal of biomechanics 47 (1) (2014) 50–58.

[25] M. Christophy, N. A. F. Senan, J. C. Lotz, O. M. O'Reilly, A musculoskeletal model for the lumbar spine, Biomechanics and modeling in mechanobiology 11 (1-2) (2012) 19–34.

[26] D. Gagnon, N. Arjmand, A. Plamondon, A. Shirazi-Adl, C. Larivière, An improved multi-joint emg-assisted optimization approach to estimate joint and muscle forces in a musculoskeletal model of the lumbar spine, Journal of biomechanics 44 (8) (2011) 1521–1529.

[27] A. G. Bruno, M. L. Bouxsein, D. E. Anderson, Development and validation of a musculoskeletal model of the fully articulated thoracolumbar spine and rib cage, Journal of biomechanical engineering 137 (8) (2015) 081003.

[28] J. A. Prinold, M. Masjedi, G. R. Johnson, A. M. Bull, Musculoskeletal shoulder models: a technical review and proposals for research foci, Proceedings of the Institution of Mechanical Engineers, Part H: Journal of Engineering in Medicine 227 (10) (2013) 1041–1057.

[29] J. L. Hicks, T. K. Uchida, A. Seth, A. Rajagopal, S. L. Delp, Is my model good enough? best practices for verification and validation of musculoskeletal models and simulations of movement, Journal of biomechanical engineering 137 (2) (2015) 020905.

[30] M. E. Lund, M. de Zee, M. S. Andersen, J. Rasmussen, On validation of multibody musculoskeletal models, Proceedings of the Institution of Mechanical Engineers, Part H: Journal of Engineering in Medicine 226 (2) (2012) 82–94.

[31] H. Veeger, F. Van Der Helm, Shoulder function: the perfect compromise between mobility and stability, Journal of biomechanics 40 (10) (2007) 2119–2129.

[32] M. A. Zumstein, M. Pinedo, J. Old, P. Boileau, Problems, complications, reoperations, and revisions in reverse total shoulder arthroplasty: a systematic review, Journal of shoulder and elbow surgery 20 (1) (2011) 146–157.

[33] A. Fick, E. Weber, Anatomisch-mechanische Studie über die Schultermuskeln, 1877.

[34] N. Wuelker, C. Wirth, W. Plitz, B. Roetman, A dynamic shoulder model: reliability testing and muscle force study, Journal of biomechanics 28 (5) (1995) 489–499.

[35] C. J. de Duca, W. J. Forrest, Force analysis of individual muscles acting simultaneously on the shoulder joint during isometric abduction, Journal of biomechanics 6 (4) (1973) 385–386.

[36] N. Poppen, P. Walker, Forces at the glenohumeral joint in abduction., Clinical Orthopaedics and Related Research (135) (1978) 165–170.

[37] C. Högfors, G. Sigholm, P. Herberts, Biomechanical model of the human shoulder—i. elements, Journal of biomechanics 20 (2) (1987) 157–166.

[38] A. Seireg, R. Arvikar, Biomechanical analysis of the musculoskeletal structure for medicine and sports, Hemisphere Pub, 1989.

[39] F. C. Van der Helm, Analysis of the kinematic and dynamic behavior of the shoulder mechanism, Journal of biomechanics 27 (5) (1994) 527–550.

[40] F. C. Van der Helm, A finite element musculoskeletal model of the shoulder mechanism, Journal of biomechanics 27 (5) (1994) 555–569.

[41] G. M. Pronk, A kinematic model of the shoulder girdle: a resume, Journal of medical engineering & technology 13 (1-2) (1989) 119–123.

[42] A. Nikooyan, H. Veeger, P. Westerhoff, F. Graichen, G. Bergmann, F. Van der Helm, Validation of the delft shoulder and elbow model using in-vivo glenohumeral joint contact forces, Journal of biomechanics 43 (15) (2010) 3007–3014.

[43] A. Nikooyan, H. Veeger, P. Westerhoff, B. Bolsterlee, F. Graichen, G. Bergmann, F. Van der Helm, An emg-driven musculoskeletal model of the shoulder, Human movement science 31 (2) (2012) 429–447.

[44] M. Damsgaard, J. Rasmussen, S. T. Christensen, E. Surma, M. De Zee, Analysis of musculoskeletal systems in the anybody modeling system, Simulation Modelling Practice and Theory 14 (8) (2006) 1100–1111.

[45] K. R. Holzbaur, W. M. Murray, S. L. Delp, A model of the upper extremity for simulating musculoskeletal surgery and analyzing neuromuscular control, Annals of biomedical engineering 33 (6) (2005) 829–840.

[46] C. R. Dickerson, D. B. Chaffin, R. E. Hughes, A mathematical musculoskeletal shoulder model for proactive ergonomic analysis, Computer methods in biomechanics and biomedical engineering 10 (6) (2007) 389–400.

[47] D. Blana, J. G. Hincapie, E. K. Chadwick, R. F. Kirsch, A musculoskeletal model of the upper extremity for use in the development of neuroprosthetic systems, Journal of biomechanics 41 (8) (2008) 1714–1721.

[48] W. Maurel, 3d modeling of the human upper limb including the biomechanics of joints, muscles and soft tissues, Tech. rep., EPFL Lausanne (1999).

[49] A. Naaim, F. Moissenet, S. Duprey, M. Begon, L. Cheze, Effect of various upper limb multibody models on soft tissue artefact correction: A case study, Journal of biomechanics 62 (2017) 102–109.

[50] S. Duprey, A. Naaim, F. Moissenet, M. Begon, L. Chèze, Kinematic models of the upper limb joints for multibody kinematics optimisation: An overview, Journal of biomechanics 62 (2017) 87–94.

[51] A. Erdemir, S. McLean, W. Herzog, A. J. van den Bogert, Model-based estimation of muscle forces exerted during movements, Clinical biomechanics 22 (2) (2007) 131–154.

[52] A. Terrier, M. Aeberhard, Y. Michellod, P. Mullhaupt, D. Gillet, A. Farron, D. P. Pioletti, A musculoskeletal shoulder model based on pseudo-inverse and null-space optimization, Medical Engineering and Physics 32 (9) (2010) 1050–1056.

[53] F. Leboeuf, G. Bessonnet, P. Seguin, P. Lacouture, Energetic versus sthenic optimality criteria for gymnastic movement synthesis, Multibody System Dynamics 16 (3) (2006) 213–236.

[54] S. L. Fischer, E. C. Brenneman, R. P. Wells, C. R. Dickerson, Relationships between psychophysically acceptable and maximum voluntary hand force capacity in the context of underlying biomechanical limitations, Applied ergonomics 43 (5) (2012) 813–820.

[55] B. Stenlund, L. Lindbeck, D. Karlsson, Significance of house painters' work techniques on shoulder muscle strain during overhead work, Ergonomics 45 (6) (2002) 455–468.

[56] Y. Boulanaache, S. Bergamin, F. Becce, A. Farron, A. Terrier, Overcorrected glenoid implants to prevent recurrent glenohumeral subluxation after total shoulder arthroplasty: a patient-specific finite element analysis, Computer methods in biomechanics and biomedical engineering 20 (sup1) (2017) 25–26.

[57] K. R. Saul, S. Hayon, T. L. Smith, C. J. Tuohy, S. Mannava, Postural dependence of passive tension in the supraspinatus following rotator cuff repair: a simulation analysis, Clinical Biomechanics 26 (8) (2011) 804–810.

[58] E. Sarshari, D. Ingram, C. A. Engelhardt, A. Farron, D. Pioletti, A. Terrier, P. Müllhaupt, Active stability of glenohumeral joint diminishes during the end-range motions, in: ESB15-0089, no. EPFL-CONF-205110, 2015.

[59] D. Blana, J. G. Hincapie, E. K. Chadwick, R. F. Kirsch, Selection of muscle and nerve-cuff electrodes for neuroprostheses using customizable musculoskeletal model., Journal of Rehabilitation Research & Development 50 (3).

[60] J. G. Hincapie, R. F. Kirsch, Feasibility of emg-based neural network controller for an upper extremity neuroprosthesis, IEEE transactions on neural systems and rehabilitation engineering 17 (1) (2009) 80–90.

[61] B. W. Kibler, A. Sciascia, T. Wilkes, Scapular dyskinesis and its relation to shoulder injury, JAAOS-Journal of the American Academy of Orthopaedic Surgeons 20 (6) (2012) 364–372.

[62] A. Farron, A. Terrier, P. Büchler, Risks of loosening of a prosthetic glenoid implanted in retroversion, Journal of shoulder and elbow surgery 15 (4) (2006) 521–526.

[63] A. Terrier, R. Obrist, F. Becce, A. Farron, Cement stress predictions after anatomic total shoulder arthroplasty are correlated with preoperative glenoid bone quality, Journal of shoulder and elbow surgery 26 (9) (2017) 1644–1652.

[64] C. Engelhardt, A. Farron, F. Becce, N. Place, D. P. Pioletti, A. Terrier, Effects of glenoid inclination and acromion index on humeral head translation and glenoid articular cartilage strain, Journal of shoulder and elbow surgery 26 (1) (2017) 157–164.

[65] D. Magermans, E. Chadwick, H. Veeger, F. Van der Helm, P. Rozing, Biomechanical analysis of tendon transfers for massive rotator cuff tears, Clinical Biomechanics 19 (4) (2004) 350–357.

[66] A. G. Cutti, H. D. Veeger, Shoulder biomechanics: today's consensus and tomorrow's perspectives (2009).

[67] T. Yanagawa, C. J. Goodwin, K. B. Shelburne, J. E. Giphart, M. R. Torry, M. G. Pandy, Contributions of the individual muscles of the shoulder to glenohumeral joint stability during abduction, Journal of biomechanical engineering 130 (2) (2008) 021024.

[68] B. Bolsterlee, Subject-specific upper extremity modelling.

[69] M. Laitenberger, M. Raison, D. Périé, M. Begon, Refinement of the upper limb joint kinematics and dynamics using a subject-specific closed-loop forearm model, Multibody System Dynamics 33 (4) (2015) 413–438.

[70] M. W. Rodosky, C. D. Harner, F. H. Fu, The role of the long head of the biceps muscle and superior glenoid labrum in anterior stability of the shoulder, The American journal of sports medicine 22 (1) (1994) 121–130.

[71] E. Itoi, D. K. Kuechle, S. R. Newman, B. F. Morrey, K.-N. An, Stabilising function of the biceps in stable and unstable shoulders, The Journal of bone and joint surgery. British volume 75 (4) (1993) 546–550.

[72] J. J. Warner, P. J. McMahon, The role of the long head of the biceps brachii in superior stability of the glenohumeral joint, JBJS 77 (3) (1995) 366–372.

[73] M. J. Pagnani, X.-H. Deng, R. F. Warren, P. A. Torzilli, S. J. O'Brien, Role of the long head of the biceps brachii in glenohumeral stability: a biomechanical study in cadavera, Journal of shoulder and elbow surgery 5 (4) (1996) 255–262.

[74] E. Roux, S. Bouilland, A.-P. Godillon-Maquinghen, D. Bouttens, Evaluation of the global optimisation method within the upper limb kinematics analysis, Journal of biomechanics 35 (9) (2002) 1279–1283.

[75] H. Veeger, B. Yu, Orientation of axes in the elbow and forearm for biomechanical modelling, in: Biomedical Engineering Conference, 1996., Proceedings of the 1996 Fifteenth Southern, IEEE, 1996, pp. 377–380.

[76] O. Rettig, L. Fradet, P. Kasten, P. Raiss, S. I. Wolf, A new kinematic model of the upper extremity based on functional joint parameter determination for shoulder and elbow, Gait & posture 30 (4) (2009) 469–476.

[77] M. L. Zampagni, D. Casino, S. Martelli, A. Visani, M. Marcacci, A protocol for clinical evaluation of the carrying angle of the elbow by anatomic landmarks, Journal of shoulder and elbow surgery 17 (1) (2008) 106–112.

[78] M. Raison, C. Detrembleur, P. Fisette, J.-C. Samin, Assessment of antagonistic muscle forces during forearm flexion/extension, in: Multibody Dynamics, Springer, 2011, pp. 215–238.

[79] A. Weinberg, I. Pietsch, M. Helm, J. Hesselbach, H. Tscherne, A new kinematic model of pro-and supination of the human forearm, Journal of biomechanics 33 (4) (2000) 487–491.

[80] A. Kecskeméthy, A. Weinberg, An improved elasto-kinematic model of the human forearm for biofidelic medical diagnosis, Multibody System Dynamics 14 (1) (2005) 1–21.

[81] A. Weinberg, I. Pietsch, M. Krefft, H. Pape, M. Van Griensven, M. Helm, H. Reilmann, H. Tscherne, Die pro-und supination des unterarms unter besonderer berücksichtigung der articulatio humeroulnaris, Der Unfallchirurg 104 (5) (2001) 404–409.

[82] P. Kasten, M. Krefft, J. Hesselbach, A.-M. Weinberg, Kinematics of the ulna during pronation and supination in a cadaver study: implications for elbow arthroplasty, Clinical Biomechanics 19 (1) (2004) 31–35.

[83] D. Gattamelata, E. Pezzuti, P. P. Valentini, Accurate geometrical constraints for the computer aided modelling of the human upper limb, Computer-Aided Design 39 (7) (2007) 540–547.

[84] J. Xu, P. Kasten, A. Weinberg, A. Kecskeméthy, Automated fitting of an elastokinematic surrogate mechanism for forearm motion from mri measurements, in: Advances in Robot Kinematics: Motion in Man and Machine, Springer, 2010, pp. 349–358.

[85] S. Martelli, M. E. Kersh, M. G. Pandy, Sensitivity of femoral strain calculations to anatomical scaling errors in musculoskeletal models of movement, Journal of biomechanics 48 (13) (2015) 3615–3624.

[86] G. Rao, D. Amarantini, E. Berton, D. Favier, Influence of body segments' parameters estimation models on inverse dynamics solutions during gait, Journal of biomechanics 39 (8) (2006) 1531–1536.

[87] W. Wu, P. V. Lee, A. L. Bryant, M. Galea, D. C. Ackland, Subject-specific musculoskeletal modeling in the evaluation of shoulder muscle and joint function, Journal of biomechanics 49 (15) (2016) 3626–3634.

[88] M. L. Neal, R. Kerckhoffs, Current progress in patient-specific modeling, Briefings in bioinformatics 11 (1) (2009) 111–126.

[89] V. Zatsiorski, In vivo body segment inertial parameters determination using gamma-scanner method, Biomechanics of human movement (1990) 186–202.

[90] P. De Leva, Adjustments to zatsiorsky-seluyanov's segment inertia parameters, Journal of biomechanics 29 (9) (1996) 1223–1230.

[91] D. A. Winter, Biomechanics and motor control of human movement, John Wiley & Sons, 2009.

[92] J. A. Prinold, A. M. Bull, Scaling and kinematics optimisation of the scapula and thorax in upper limb musculoskeletal models, Journal of biomechanics 47 (11) (2014) 2813–2819.

[93] J. T. McConville, C. E. Clauser, T. D. Churchill, J. Cuzzi, I. Kaleps, Anthropometric relationships of body and body segment moments of inertia, Tech. rep., ANTHROPOLOGY RESEARCH PROJECT INC YELLOW SPRINGS OH (1980).

[94] J. W. Young, R. F. Chandler, C. C. Snow, K. M. Robinette, G. F. Zehner, M. S. Lofberg, Anthropometric and mass distribution characteristics of the adult female, Tech. rep. (1983).

[95] R. Dumas, L. Cheze, J.-P. Verriest, Adjustments to mcconville et al. and young et al. body segment inertial parameters, Journal of biomechanics 40 (3) (2007) 543–553.

[96] S. Martelli, H. Veeger, F. Van der Helm, Scaling of a shoulder musculoskeletal model does not lead to significant improvements, in: Proceedings of the 7th Conference of the International Shoulder Group. University of Bologna, Italy, 2008.

[97] J. Rasmussen, M. de Zee, M. Damsgaard, S. T. Christensen, C. Marek, K. Siebertz, A general method for scaling musculo-skeletal models, in: 2005 International Symposium on Computer Simulation in Biomechanics, Cleveland, OH, 2005.

[98] B. Bolsterlee, H. Veeger, F. C. van der Helm, Modelling clavicular and scapular kinematics: from measurement to simulation, Medical & biological engineering & computing 52 (3) (2014) 283–291.

[99] M. E. Lund, M. S. Andersen, M. de Zee, J. Rasmussen, Scaling of musculoskeletal models from static and dynamic trials, International Biomechanics 2 (1) (2015) 1–11.

[100] D. Ingram, C. Engelhardt, A. Farron, A. Terrier, P. Müllhaupt, Modelling of the human shoulder as a parallel mechanism without constraints, Mechanism and Machine Theory 100 (2016) 120–137.

[101] R. W. Nyffeler, R. Sheikh, T. S. Atkinson, H. A. Jacob, P. Favre, C. Gerber, Effects of glenoid component version on humeral head displacement and joint reaction forces: an experimental study, Journal of shoulder and elbow surgery 15 (5) (2006) 625–629.

[102] A. S. Wong, L. Gallo, J. E. Kuhn, J. E. Carpenter, R. E. Hughes, The effect of glenoid inclination on superior humeral head migration, Journal of shoulder and elbow surgery 12 (4) (2003) 360–364.

[103] E. Sarshari, A. Terrier, A. Farron, P. Mullhaupt, An initialization technique for hill-type musculotendon models, submitted to ASME Journal of Biomechanical Engineering (BIO-18-1186).

[104] B. Bolsterlee, A. A. Zadpoor, Transformation methods for estimation of subject-specific scapular muscle attachment sites, Computer methods in biomechanics and biomedical engineering 17 (13) (2014) 1492–1501.

[105] R. Matias, C. Andrade, A. P. Veloso, A transformation method to estimate muscle attachments based on three bony landmarks, Journal of biomechanics 42 (3) (2009) 331–335.

[106] B. Kaptein, F. Van der Helm, Estimating muscle attachment contours by transforming geometrical bone models, Journal of biomechanics 37 (3) (2004) 263–273.

[107] Y. M. Yang, D. Rueckert, A. M. Bull, Predicting the shapes of bones at a joint: application to the shoulder, Computer Methods in Biomechanics and Biomedical Engineering 11 (1) (2008) 19–30.

[108] L. Scheys, I. Jonkers, D. Loeckx, F. Maes, A. Spaepen, P. Suetens, Image based musculoskeletal modeling allows personalized biomechanical analysis of gait, in: International Symposium on Biomedical Simulation, Springer, 2006, pp. 58–66.

[109] A. Krobot, M. Janura, M. Elfmark, Functional categorization of the individual morphology of the scapula, Medical & biological engineering & computing 47 (5) (2009) 497–506.

[110] D. Nolte, C. K. Tsang, K. Y. Zhang, Z. Ding, A. E. Kedgley, A. M. Bull, Non-linear scaling of a musculoskeletal model of the lower limb using statistical shape models, Journal of biomechanics 49 (14) (2016) 3576–3581.

[111] B. A. Garner, M. G. Pandy, The obstacle-set method for representing muscle paths in musculoskeletal models, Computer methods in biomechanics and biomedical engineering 3 (1) (2000) 1–30.

[112] D. Ingram, C. Engelhardt, A. Farron, A. Terrier, P. Müllhaupt, Muscle moment-arms: a key element in muscle-force estimation, Computer methods in biomechanics and biomedical engineering 18 (5) (2015) 506–513.

[113] B. Bolsterlee, A. N. Vardy, F. C. van der Helm, H. D. Veeger, The effect of scaling physiological cross-sectional area on musculoskeletal model predictions, Journal of biomechanics 48 (10) (2015) 1760–1768.

[114] K. R. Holzbaur, W. M. Murray, G. E. Gold, S. L. Delp, Upper limb muscle volumes in adult subjects, Journal of biomechanics 40 (4) (2007) 742–749.

[115] K. M. Flegal, M. D. Carroll, B. K. Kit, C. L. Ogden, Prevalence of obesity and trends in the distribution of body mass index among us adults, 1999-2010, Jama 307 (5) (2012) 491–497.

[116] S. Meeuwsen, G. Horgan, M. Elia, The relationship between bmi and percent body fat, measured by bioelectrical impedance, in a large adult sample is curvilinear and influenced by age and sex, Clinical nutrition 29 (5) (2010) 560–566.

[117] D. C. Frankenfield, W. A. Rowe, R. N. Cooney, J. S. Smith, D. Becker, Limits of body mass index to detect obesity and predict body composition, Nutrition 17 (1) (2001) 26–30.

[118] M. Froeling, A. J. Nederveen, D. F. Heijtel, A. Lataster, C. Bos, K. Nicolay, M. Maas, M. R. Drost, G. J. Strijkers, Diffusion-tensor mri reveals the complex muscle architecture of the human forearm, Journal of Magnetic Resonance Imaging 36 (1) (2012) 237–248.

[119] A. Terrier, A. Vogel, M. Capezzali, A. Farron, An algorithm to allow humerus translation in the indeterminate problem of shoulder abduction, Medical engineering & physics 30 (6) (2008) 710–716.

[120] A. Terrier, X. Larrea, V. M. Camine, D. Pioletti, A. Farron, Importance of the subscapularis muscle after total shoulder arthroplasty, Clinical Biomechanics 28 (2) (2013) 146–150.

[121] A. R. Hopkins, U. N. Hansen, A. A. Amis, M. Taylor, N. Gronau, C. Anglin, Finite element modelling of glenohumeral kinematics following total shoulder arthroplasty, Journal of biomechanics 39 (13) (2006) 2476–2483.

[122] L. Sins, P. Tétreault, N. Hagemeister, N. Nuño, Adaptation of the anybody™ musculoskeletal shoulder model to the nonconforming total shoulder arthroplasty context, Journal of biomechanical engineering 137 (10) (2015) 101006.

[123] C. Quental, J. Folgado, J. Ambrósio, J. Monteiro, A new shoulder model with a biologically inspired glenohumeral joint, Medical Engineering & Physics 38 (9) (2016) 969–977.

[124] P. Favre, M. Senteler, J. Hipp, S. Scherrer, C. Gerber, J. G. Snedeker, An integrated model of active glenohumeral stability, Journal of biomechanics 45 (13) (2012) 2248–2255.

[125] P. Büchler, N. Ramaniraka, L. Rakotomanana, J. Iannotti, A. Farron, A finite element model of the shoulder: application to the comparison of normal and osteoarthritic joints, Clinical Biomechanics 17 (9) (2002) 630–639.

[126] N. Wuelker, H. Schmotzer, K. Thren, M. Korell, Translation of the glenohumeral joint with simulated active elevation., Clinical orthopaedics and related research 309 (1994) 193–200.

[127] R. Kelkar, V. M. Wang, E. L. Flatow, P. M. Newton, G. A. Ateshian, L. U. Bigliani, R. J. Pawluk, V. C. Mow, Glenohumeral mechanics: a study of articular geometry, contact, and kinematics, Journal of Shoulder and Elbow Surgery 10 (1) (2001) 73–84.

[128] D. S. Teyhen, T. R. Christ, E. R. Ballas, C. W. Hoppes, J. D. Walters, D. S. Christie, G. Dreitzler, E. J. Kane, Digital fluoroscopic video assessment of glenohumeral migration: Static vs. dynamic conditions, Journal of biomechanics 43 (7) (2010) 1380–1385.

[129] D. F. Massimini, P. J. Boyer, R. Papannagari, T. J. Gill, J. P. Warner, G. Li, In-vivo glenohumeral translation and ligament elongation during abduction and abduction with internal and external rotation, Journal of orthopaedic surgery and research 7 (1) (2012) 1.

[130] W. Sahara, K. Sugamoto, M. Murai, H. Tanaka, H. Yoshikawa, The three-dimensional motions of glenohumeral joint under semi-loaded condition during arm abduction using vertically open mri, Clinical Biomechanics 22 (3) (2007) 304–312.

[131] H. Graichen, T. Stammberger, H. Bonel, K.-H. Englmeier, M. Reiser, F. Eckstein, Glenohumeral translation during active and passive elevation of the shoulder—a 3d open-mri study, Journal of biomechanics 33 (5) (2000) 609–613.

[132] N. Nishinaka, H. Tsutsui, K. Mihara, K. Suzuki, D. Makiuchi, Y. Kon, T. W. Wright, M. W. Moser, K. Gamada, H. Sugimoto, et al., Determination of in vivo glenohumeral translation using fluoroscopy and shape-matching techniques, Journal of Shoulder and Elbow Surgery 17 (2) (2008) 319–322.

[133] M. J. Bey, S. K. Kline, R. Zauel, T. R. Lock, P. A. Kolowich, Measuring dynamic in-vivo glenohumeral joint kinematics: technique and preliminary results, Journal of biomechanics 41 (3) (2008) 711–714.

[134] M. S. Andersen, M. Damsgaard, J. Rasmussen, Force-dependent kinematics: a new analysis method for non-conforming joints, in: 13th Biennial International Symposium on Computer Simulation in Biomechanics, 2011.

[135] D. P. Pioletti, L. Rakotomanana, J.-F. Benvenuti, P.-F. Leyvraz, Viscoelastic constitutive law in large deformations: application to human knee ligaments and tendons, Journal of biomechanics 31 (8) (1998) 753–757.

[136] A. Terrier, A. Reist, A. Vogel, A. Farron, Effect of supraspinatus deficiency on humerus translation and glenohumeral contact force during abduction, Clinical Biomechanics 22 (6) (2007) 645–651.

[137] A. Terrier, F. Merlini, D. P. Pioletti, A. Farron, Total shoulder arthroplasty: downward inclination of the glenoid component to balance supraspinatus deficiency, Journal of shoulder and elbow surgery 18 (3) (2009) 360–365.

[138] M. Warner, P. Chappell, M. Stokes, Measuring scapular kinematics during arm lowering using the acromion marker cluster, Human movement science 31 (2) (2012) 386–396.

[139] P. M. Ludewig, V. Phadke, J. P. Braman, D. R. Hassett, C. J. Cieminski, R. F. LaPrade, Motion of the shoulder complex during multiplanar humeral elevation, The Journal of Bone and Joint Surgery. American volume. 91 (2) (2009) 378.

[140] R. Stagni, S. Fantozzi, A. Cappello, A. Leardini, Quantification of soft tissue artefact in motion analysis by combining 3d fluoroscopy and stereophotogrammetry: a study on two subjects, Clinical Biomechanics 20 (3) (2005) 320–329.

[141] A. G. Cutti, G. Paolini, M. Troncossi, A. Cappello, A. Davalli, Soft tissue artefact assessment in humeral axial rotation, Gait & Posture 21 (3) (2005) 341–349.

[142] T.-W. Lu, J. O'connor, Bone position estimation from skin marker co-ordinates using global optimisation with joint constraints, Journal of biomechanics 32 (2) (1999) 129–134.

[143] H. Veeger, The position of the rotation center of the glenohumeral joint, Journal of biomechanics 33 (12) (2000) 1711–1715.

[144] H. Woltring, R. Huiskes, A. De Lange, F. Veldpaus, Finite centroid and helical axis estimation from noisy landmark measurements in the study of human joint kinematics, Journal of biomechanics 18 (5) (1985) 379–389.

[145] V. Camomilla, A. Cereatti, G. Vannozzi, A. Cappozzo, An optimized protocol for hip joint centre determination using the functional method, Journal of biomechanics 39 (6) (2006) 1096–1106.

[146] M. H. Schwartz, A. Rozumalski, A new method for estimating joint parameters from motion data, Journal of biomechanics 38 (1) (2005) 107–116.

[147] R. M. Ehrig, W. R. Taylor, G. N. Duda, M. O. Heller, A survey of formal methods for determining the centre of rotation of ball joints, Journal of biomechanics 39 (15) (2006) 2798–2809.

[148] K. Halvorsen, Bias compensated least squares estimate of the center of rotation, Journal of Biomechanics 36 (7) (2003) 999–1008.

[149] S. S. H. U. Gamage, J. Lasenby, New least squares solutions for estimating the average centre of rotation and the axis of rotation, Journal of biomechanics 35 (1) (2002) 87–93.

[150] C. Meskers, F. C. Van der Helm, L. Rozendaal, P. Rozing, In vivo estimation of the glenohumeral joint rotation center from scapular bony landmarks by linear regression, Journal of biomechanics 31 (1) (1997) 93–96.

[151] D. Lloyd, J. Alderson, B. Elliott, An upper limb kinematic model for the examination of cricket bowling: A case study of mutiah muralitharan, Journal of sports sciences 18 (12) (2000) 975–982.

[152] A. Campbell, D. Lloyd, J. Alderson, B. Elliott, Mri development and validation of two new predictive methods of glenohumeral joint centre location identification and comparison with established techniques, Journal of biomechanics 42 (10) (2009) 1527–1532.

[153] R. Schmidt, C. Disselhorst-Klug, J. Silny, G. Rau, A marker-based measurement procedure for unconstrained wrist and elbow motions, Journal of Biomechanics 32 (6) (1999) 615–621.

[154] K. F. MacLean, J. N. Chopp, T.-J. Grewal, B. R. Picco, C. R. Dickerson, Three-dimensional comparison of static and dynamic scapular motion tracking techniques, Journal of Electromyography and Kinesiology 24 (1) (2014) 65–71.

[155] M. Lempereur, S. Brochard, V. Burdin, O. Rémy-Néris, Difference between palpation and optoelectronics recording of scapular motion, Computer methods in biomechanics and biomedical engineering 13 (1) (2010) 49–57.

[156] K. Matsui, K. Shimada, P. D. Andrew, Deviation of skin marker from bone target during movement of the scapula, Journal of Orthopaedic Science 11 (2) (2006) 180–184.

[157] A. R. Karduna, P. W. McClure, L. A. Michener, B. Sennett, Dynamic measurements of three-dimensional scapular kinematics: a validation study, Journal of biomechanical engineering 123 (2) (2001) 184–190.

[158] J. De Groot, R. Brand, A three-dimensional regression model of the shoulder rhythm, Clinical Biomechanics 16 (9) (2001) 735–743.

[159] T.-J. Grewal, C. R. Dickerson, A novel three-dimensional shoulder rhythm definition that includes overhead and axially rotated humeral postures, Journal of biomechanics 46 (3) (2013) 608–611.

[160] J. H. de Groot, E. R. Valstar, H. J. Arwert, Velocity effects on the scapulo-humeral rhythm, Clinical Biomechanics 13 (8) (1998) 593–602.

[161] C. Högfors, B. Peterson, G. Sigholm, P. Herberts, Biomechanical model of the human shoulder joint—ii. the shoulder rhythm, Journal of biomechanics 24 (8) (1991) 699–709.

[162] F. C. van der Helm, G. M. Pronk, Three-dimensional recording and description of motions of the shoulder mechanism, Journal of biomechanical engineering 117 (1) (1995) 27–40.

[163] J. Mattson, S. Russo, W. Rose, K. Rowley, J. Richards, Identification of scapular kinematics using surface mapping: a validation study, Journal of biomechanics 45 (12) (2012) 2176–2179.

[164] K. J. McQuade, G. L. Smidt, Dynamic scapulohumeral rhythm: the effects of external resistance during elevation of the arm in the scapular plane, Journal of Orthopaedic & Sports Physical Therapy 27 (2) (1998) 125–133.

[165] J. A. Prinold, A. F. Shaheen, A. M. Bull, Skin-fixed scapula trackers: a comparison of two dynamic methods across a range of calibration positions, Journal of biomechanics 44 (10) (2011) 2004–2007.

[166] G. Johnson, P. Stuart, S. Mitchell, A method for the measurement of three-dimensional scapular movement, Clinical Biomechanics 8 (5) (1993) 269–273.

[167] C. van Andel, K. van Hutten, M. Eversdijk, D. Veeger, J. Harlaar, Recording scapular motion using an acromion marker cluster, Gait & posture 29 (1) (2009) 123–128.

[168] N. Klopčar, J. Lenarčič, Bilateral and unilateral shoulder girdle kinematics during humeral elevation, Clinical Biomechanics 21 (2006) S20–S26.

[169] A. Shaheen, C. Alexander, A. Bull, Effects of attachment position and shoulder orientation during calibration on the accuracy of the acromial tracker, Journal of biomechanics 44 (7) (2011) 1410–1413.

[170] F. E. Zajac, Muscle and tendon properties models scaling and application to biomechanics and motor, Critical reviews in biomedical engineering 17 (4) (1989) 359–411.

[171] J. M. Winters, L. Stark, Muscle models: what is gained and what is lost by varying model complexity, Biological cybernetics 55 (6) (1987) 403–420.

[172] A. Huxley, Muscular contraction., The Journal of physiology 243 (1) (1974) 1–43.

[173] E. Eisenberg, T. L. Hill, Y.-d. Chen, Cross-bridge model of muscle contraction. quantitative analysis, Biophysical Journal 29 (2) (1980) 195–227.

[174] G. I. Zahalak, S.-P. Ma, Muscle activation and contraction: constitutive relations based directly on cross-bridge kinetics, Journal of biomechanical engineering 112 (1) (1990) 52–62.

[175] A. Hill, The heat of shortening and the dynamic constants of muscle, in: Proc. R. Soc. Lond. B, Vol. 126, The Royal Society, 1938, pp. 136–195.

[176] D. Wilkie, The relation between force and velocity in human muscle, The Journal of physiology 110 (3-4) (1949) 249–280.

[177] J. Ritchie, D. Wilkie, The dynamics of muscular contraction, The Journal of physiology 143 (1) (1958) 104–113.

[178] J. M. Winters, L. Stark, Analysis of fundamental human movement patterns through the use of in-depth antagonistic muscle models, IEEE transactions on biomedical engineering (10) (1985) 826–839.

[179] J. M. Winters, An improved muscle-reflex actuator for use in large-scale neuromusculoskeletal models, Annals of biomedical engineering 23 (4) (1995) 359–374.

[180] M. Millard, T. Uchida, A. Seth, S. L. Delp, Flexing computational muscle: modeling and simulation of musculotendon dynamics, Journal of biomechanical engineering 135 (2) (2013) 021005.

[181] J. M. Winters, M. H. Nam, L. W. Stark, Modeling dynamical interactions between fast and slow movements: fast saccadic eye movement behavior in the presence of the slower vor, Mathematical biosciences 68 (2) (1984) 159–185.

[182] G. Joyce, P. Rack, Isotonic lengthening and shortening movements of cat soleus muscle, The Journal of physiology 204 (2) (1969) 475–491.

[183] A. M. Krylow, T. G. Sandercock, Dynamic force responses of muscle involving eccentric contraction, Journal of biomechanics 30 (1) (1997) 27–33.

[184] P. Loan, Dynamics pipeline, Evanston IL, Musculographics.

[185] J. T. Dennerlein, Finger flexor tendon forces are a complex function of finger joint motions and fingertip forces, Journal of Hand Therapy 18 (2) (2005) 120–127.

[186] W. Herzog, Force-sharing among synergistic muscles: theoretical considerations and experimental approaches., Exercise and sport sciences reviews 24 (1) (1996) 173–202.

[187] J. Cholewicki, S. M. McGill, R. W. Norman, Comparison of muscle forces and joint load from an optimization and emg assisted lumbar spine model: towards development of a hybrid approach, Journal of biomechanics 28 (3) (1995) 321–331.

[188] C. Engelhardt, V. Malfroy Camine, D. Ingram, P. Müllhaupt, A. Farron, D. Pioletti, A. Terrier, Comparison of an emg-based and a stress-based method to predict shoulder muscle forces, Computer methods in biomechanics and biomedical engineering 18 (12) (2015) 1272–1279.

[189] J. Collins, The redundant nature of locomotor optimization laws, Journal of biomechanics 28 (3) (1995) 251–267.

[190] P. Favre, R. Sheikh, S. F. Fucentese, H. A. Jacob, An algorithm for estimation of shoulder muscle forces for clinical use, Clinical biomechanics 20 (8) (2005) 822–833.

[191] P. Favre, J. G. Snedeker, C. Gerber, Numerical modelling of the shoulder for clinical applications, Philosophical Transactions of the Royal Society of London A: Mathematical, Physical and Engineering Sciences 367 (1895) (2009) 2095–2118.

[192] J. E. Labriola, T. Q. Lee, R. E. Debski, P. J. McMahon, Stability and instability of the glenohumeral joint: the role of shoulder muscles, Journal of shoulder and elbow surgery 14 (1) (2005) S32–S38.

[193] E. Sarshari, A. Farron, A. Terrier, D. Pioletti, P. Mullhaupt, A simulation framework for humeral head translations, Medical Engineering and Physics 49 (2017) 140–147.

[194] E. Forster, U. Simon, P. Augat, L. Claes, Extension of a state-of-the-art optimization criterion to predict co-contraction, Journal of biomechanics 37 (4) (2004) 577–581.

[195] R. Raikova, About weight factors in the non-linear objective functions used for solving indeterminate problems in biomechanics, Journal of Biomechanics 32 (7) (1999) 689–694.

[196] B. Laursen, B. R. Jensen, G. Németh, G. Sjøgaard, A model predicting individual shoulder muscle forces based on relationship between electromyographic and 3d external forces in static position, Journal of biomechanics 31 (8) (1998) 731–739.

[197] J. Langenderfer, S. LaScalza, A. Mell, J. E. Carpenter, J. E. Kuhn, R. E. Hughes, An emg-driven model of the upper extremity and estimation of long head biceps force, Computers in biology and medicine 35 (1) (2005) 25–39.

[198] R. L. Brookham, E. E. Middlebrook, T.-j. Grewal, C. R. Dickerson, The utility of an empirically derived co-activation ratio for muscle force prediction through optimization, Journal of biomechanics 44 (8) (2011) 1582–1587.

[199] G. Bergmann, F. Graichen, A. Bender, A. Rohlmann, A. Halder, A. Beier, P. Westerhoff, In vivo gleno-humeral joint loads during forward flexion and abduction, Journal of biomechanics 44 (8) (2011) 1543–1552.

[200] A. Terrier, J. Ston, X. Larrea, A. Farron, Measurements of three-dimensional glenoid erosion when planning the prosthetic replacement of osteoarthritic shoulders, Bone Joint J 96 (4) (2014) 513–518.

[201] G. Wu, F. C. Van der Helm, H. D. Veeger, M. Makhsous, P. Van Roy, C. Anglin, J. Nagels, A. R. Karduna, K. McQuade, X. Wang, et al., Isb recommendation on definitions of joint coordinate systems of various joints for the reporting of human joint motion—part ii: shoulder, elbow, wrist and hand, Journal of biomechanics 38 (5) (2005) 981–992.

[202] M. Jackson, B. Michaud, P. Tétreault, M. Begon, Improvements in measuring shoulder joint kinematics, Journal of biomechanics 45 (12) (2012) 2180–2183.

[203] B. A. Garner, M. G. Pandy, Estimation of musculotendon properties in the human upper limb, Annals of biomedical engineering 31 (2) (2003) 207–220.

[204] R. S. Churchill, J. J. Brems, H. Kotschi, Glenoid size, inclination, and version: an anatomic study, Journal of Shoulder and Elbow Surgery 10 (4) (2001) 327–332.

[205] A. Terrier, J. Ston, A. Dewarrat, F. Becce, A. Farron, A semi-automated quantitative ct method for measuring rotator cuff muscle degeneration in shoulders with primary osteoarthritis, Orthopaedics & Traumatology: Surgery & Research 103 (2) (2017) 151–157.

[206] R. D. Crowninshield, R. A. Brand, A physiologically based criterion of muscle force prediction in locomotion, Journal of biomechanics 14 (11) (1981) 793–801.

[207] W. Wu, P. V. S. Lee, D. C. Ackland, The sensitivity of shoulder muscle and joint force predictions to changes in joint kinematics: A monte-carlo analysis, Gait & posture 54 (2017) 87–92.

[208] A. Goto, H. Moritomo, T. Murase, K. Oka, K. Sugamoto, T. Arimura, Y. Nakajima, T. Yamazaki, Y. Sato, S. Tamura, et al., In vivo elbow biomechanical analysis during flexion: three-dimensional motion analysis using magnetic resonance imaging, Journal of shoulder and elbow surgery 13 (4) (2004) 441–447.

[209] E. Sarshari, A. K. Sedigh, Selection of sensors for hydro-active suspension system of passenger car with input–output pairing considerations, Journal of Dynamic Systems, Measurement, and Control 135 (1) (2013) 011004.

[210] S. L. Delp, F. C. Anderson, A. S. Arnold, P. Loan, A. Habib, C. T. John, E. Guendelman, D. G. Thelen, Opensim: open-source software to create and analyze dynamic simulations of movement, IEEE transactions on biomedical engineering 54 (11) (2007) 1940–1950.

[211] J. Rasmussen, M. Damsgaard, E. Surma, S. T. Christensen, M. de Zee, V. Vondrak, Anybody-a software system for ergonomic optimization, in: Fifth World Congress on Structural and Multidisciplinary Optimization, Vol. 4, Citeseer, 2003.

[212] E. Sarshari, M. Mancuso, A. Terrier, A. Farron, P. Mullhaupt, D. Pioletti, Emg-assisted load-sharing for muscle force prediction in upper-extremity, subimtted to Journal Medical Engineering and Physics (MEP-D-18-00262).

[213] L. J. Soslowsky, E. L. Flatow, L. U. Bigliani, V. C. Mow, Articular geometry of the glenohumeral joint., Clinical orthopaedics and related research 285 (1992) 181–190.

[214] D. T. Greenwood, Advanced dynamics, Cambridge University Press, 2006.

[215] T. M. Guess, H. Liu, S. Bhashyam, G. Thiagarajan, A multibody knee model with discrete cartilage prediction of tibio-femoral contact mechanics, Computer methods in biomechanics and biomedical engineering 16 (3) (2013) 256–270.

[216] L. Blankevoort, J. Kuiper, R. Huiskes, H. Grootenboer, Articular contact in a three-dimensional model of the knee, Journal of biomechanics 24 (11) (1991) 1019–1031.

[217] J. E. Novotny, B. D. Beynnon, C. E. Nichols, Modeling the stability of the human glenohumeral joint during external rotation, Journal of Biomechanics 33 (3) (2000) 345–354.

[218] E. Sarshari, A. Farron, A. Terrier, D. Pioletti, P. Müllhaupt, A framework for forward-dynamics simulation of the human shoulder, in: 11th Conference of the International Shoulder Group, ISG 2016, no. EPFL-CONF-218098, 2016.

[219] J.-J. E. Slotine, W. Li, et al., Applied nonlinear control, Vol. 199, prentice-Hall Englewood Cliffs, NJ, 1991.

[220] I. Wilf, Y. Manor, Quadric-surface intersection curves: shape and structure, Computer-Aided Design 25 (10) (1993) 633–643.

[221] J. R. Dormand, Numerical methods for differential equations: a computational approach, Vol. 3, CRC Press, 1996.

[222] D. Ingram, C. Engelhardt, A. Farron, A. Terrier, P. Müllhaupt, Improving anterior deltoid activity in a musculoskeletal shoulder model–an analysis of the torque-feasible space at the sternoclavicular joint, Computer methods in biomechanics and biomedical engineering 19 (4) (2016) 450–463.

[223] C. Engelhardt, A. Farron, F. Becce, N. Place, D. P. Pioletti, A. Terrier, Effects of glenoid inclination and acromion index on humeral head translation and glenoid articular cartilage strain, Journal of Shoulder and Elbow Surgery.

[224] L. Soslowsky, E. Flatow, L. Bigliani, R. Pawluk, G. Ateshian, V. Mow, Quantitation of in situ contact areas at the glenohumeral joint: a biomechanical study, Journal of Orthopaedic Research 10 (4) (1992) 524–534.

[225] G. Hammond, J. E. Tibone, M. H. McGarry, B.-J. Jun, T. Q. Lee, Biomechanical comparison of anatomic humeral head resurfacing and hemiarthroplasty in functional glenohumeral positions, The Journal of Bone & Joint Surgery 94 (1) (2012) 68–76.

[226] R. Debski, E. Wong, S. L. Woo, F. Fu, J. Warner, An analytical approach to determine the in situ forces in the glenohumeral ligaments, Journal of biomechanical engineering 121 (3) (1999) 311–315.

[227] A. V. Fiacco, Sensitivity analysis for nonlinear programming using penalty methods, Mathematical programming 10 (1) (1976) 287–311.

[228] B. Siciliano, O. Khatib, Springer handbook of robotics, Springer Science & Business Media, 2008.

[229] J. Z. Levin, Mathematical models for determining the intersections of quadric surfaces, Computer Graphics and Image Processing 11 (1) (1979) 73–87.

[230] S. Boyd, L. Vandenberghe, Convex optimization, Cambridge university press, 2004.

[231] L. Cheze, B. Fregly, J. Dimnet, A solidification procedure to facilitate kinematic analyses based on video system data, Journal of biomechanics 28 (7) (1995) 879–884.

[232] W. R. Taylor, R. M. Ehrig, G. N. Duda, H. Schell, P. Seebeck, M. O. Heller, On the influence of soft tissue coverage in the determination of bone kinematics using skin markers, Journal of Orthopaedic Research 23 (4) (2005) 726–734.

[233] A. Seth, R. Matias, A. P. Veloso, S. L. Delp, A biomechanical model of the scapulothoracic joint to accurately capture scapular kinematics during shoulder movements, PloS one 11 (1) (2016) e0141028.

[234] B. A. Garner, M. G. Pandy, A kinematic model of the upper limb based on the visible human project (vhp) image dataset, Computer methods in biomechanics and biomedical engineering 2 (2) (1999) 107–124.

[235] H. K. Khalil, Noninear systems, Prentice-Hall, New Jersey 2 (5) (1996) 5–1.

[236] F. Hug, Can muscle coordination be precisely studied by surface electromyography?, Journal of electromyography and kinesiology 21 (1) (2011) 1–12.

[237] S. K. Gollapudi, D. C. Lin, Experimental determination of sarcomere force–length relationship in type-i human skeletal muscle fibers, Journal of biomechanics 42 (13) (2009) 2011–2016.

[238] T. Siebert, C. Rode, W. Herzog, O. Till, R. Blickhan, Nonlinearities make a difference: comparison of two common hill-type models with real muscle, Biological cybernetics 98 (2) (2008) 133–143.

[239] O. Till, T. Siebert, C. Rode, R. Blickhan, Characterization of isovelocity extension of activated muscle: a hill-type model for eccentric contractions and a method for parameter determination, Journal of theoretical biology 255 (2) (2008) 176–187.

[240] R. Woittiez, P. Huijing, H. K. Boom, R. Rozendal, A three-dimensional muscle model: a quantified relation between form and function of skeletal muscles, Journal of Morphology 182 (1) (1984) 95–113.

[241] D. G. Thelen, Adjustment of muscle mechanics model parameters to simulate dynamic contractions in older adults, Journal of biomechanical engineering 125 (1) (2003) 70–77.

[242] H. Hatze, A myocybernetic control model of skeletal muscle, Biological cybernetics 25 (2) (1977) 103–119.

[243] K. R. Kaufman, K.-N. An, W. J. Litchy, E. Chao, Physiological prediction of muscle forces—i. theoretical formulation, Neuroscience 40 (3) (1991) 781–792.

[244] S. P. Magnusson, P. Aagaard, S. Rosager, P. Dyhre-Poulsen, M. Kjaer, Load-displacement properties of the human triceps surae aponeurosis in vivo, The Journal of physiology 531 (1) (2001) 277–288.

[245] E. L. Brainerd, E. Azizi, Muscle fiber angle, segment bulging and architectural gear ratio in segmented musculature, Journal of Experimental Biology 208 (17) (2005) 3249–3261.

[246] A. J. Van Den Bogert, D. Blana, D. Heinrich, Implicit methods for efficient musculoskeletal simulation and optimal control, Procedia IUTAM 2 (2011) 297–316.

[247] L. Ljung, System identification, in: Signal analysis and prediction, Springer, 1998, pp. 163–173.

[248] E. Sarshari, M. Mancuso, A. Terrier, A. Farron, P. Mullhaupt, D. Pioletti, Motion reconstruction in upper extremity in the absence of scapula kinematics measurement-devices, subimtted to Journal of Biomechanics (BM-D-18-00419).

[249] R. J. Talmadge, R. R. Roy, V. J. Caiozzo, V. R. Edgerton, Mechanical properties of rat soleus after long-term spinal cord transection, Journal of Applied Physiology 93 (4) (2002) 1487–1497.

[250] H. Westerblad, D. Allen, J. Bruton, F. Andrade, J. Lännergren, Mechanisms underlying the reduction of isometric force in skeletal muscle fatigue, Acta Physiologica 162 (3) (1998) 253–260.

[251] K. Ranatunga, Temperature-dependence of shortening velocity and rate of isometric tension development in rat skeletal muscle, The Journal of Physiology 329 (1) (1982) 465–483.

[252] A. Pedrocchi, S. Ferrante, E. De Momi, G. Ferrigno, Error mapping controller: a closed loop neuroprosthesis controlled by artificial neural networks, Journal of neuroengineering and rehabilitation 3 (1) (2006) 25.

[253] M. K. Horsman, H. F. Koopman, F. C. van der Helm, L. P. Prosé, H. Veeger, Morphological muscle and joint parameters for musculoskeletal modelling of the lower extremity, Clinical biomechanics 22 (2) (2007) 239–247.

[254] E. Sarshari, Y. Boulanaache, A. Terrier, A. Farron, P. Mullhaupt, D. Pioletti, A matlab toolbox for scaled-generic modeling of shoulder and elbow, subimtted to Journal Source Code for Biology and Medicine (SCBM-D-18-00009).

[255] B. Jost, C. W. Pfirrmann, C. Gerber, Clinical outcome after structural failure of rotator cuff repairs, JBJS 82 (3) (2000) 304–14.

[256] F. Steenbrink, J. De Groot, H. Veeger, F. van der Helm, P. Rozing, Glenohumeral stability in simulated rotator cuff tears, Journal of biomechanics 42 (11) (2009) 1740–1745.

[257] D. C. Ackland, Y.-C. Lin, M. G. Pandy, Sensitivity of model predictions of muscle function to changes in moment arms and muscle–tendon properties: a monte-carlo analysis, Journal of biomechanics 45 (8) (2012) 1463–1471.

[258] C. Klemt, J. A. Prinold, S. Morgans, S. H. Smith, D. Nolte, P. Reilly, A. M. Bull, Analysis of shoulder compressive and shear forces during functional activities of daily life, Clinical Biomechanics 54 (2018) 34–41.

[259] P. Westerhoff, F. Graichen, A. Bender, A. Halder, A. Beier, A. Rohlmann, G. Bergmann, In vivo measurement of shoulder joint loads during activities of daily living, Journal of biomechanics 42 (12) (2009) 1840–1849.

[260] A. G. Cutti, A. Giovanardi, L. Rocchi, A. Davalli, R. Sacchetti, Ambulatory measurement of shoulder and elbow kinematics through inertial and magnetic sensors, Medical & biological engineering & computing 46 (2) (2008) 169–178.

[261] B. Kiss, J. Lévine, P. Mullhaupt, Modelling and motion planning for a class of weight handling equipments, in: 14 th International Conference on Systems Engineering, no. LA-CONF-2000-011, 2000.

[262] P. Mullhaupt, Analysis and control of underactuated mechanical nonminimum-phase systems, Department of Mechanical Engineering, EPFL.

[263] F. De Groote, A. L. Kinney, A. V. Rao, B. J. Fregly, Evaluation of direct collocation optimal control problem formulations for solving the muscle redundancy problem, Annals of biomedical engineering 44 (10) (2016) 2922–2936.

[264] D. P. Bertsekas, D. P. Bertsekas, D. P. Bertsekas, D. P. Bertsekas, Dynamic programming and optimal control, Vol. 1, Athena scientific Belmont, MA, 1995.

Ehsan Sarshari

✉ ehsan.sarshari@gmail.com

Summary

Professional mechanical engineer with eight years of experience in academia and industry.

Specialties: Multibody dynamics, biomechanics, control systems, finite element analysis, robotics, oil & gas.

Work Experience

2014–2018 **Doctoral assistant**, *Ecole Polytechnique Fédérale de Lausanne*, Switzerland

• Developed a closed-loop EMG-assisted shoulder model to predict muscle and joint forces and joint translations. The work was done in collaboration with the laboratory of biomechanical orthopedics at EPFL. Its outcome was translated for clinical applications related to treatments of osteoarthritis by total shoulder arthroplasty at CHUV university hospital. The model was presented as a Matlab toolbox.

• Supervised 15 master students on the subjects of automatic control and biomechanics.

• Worked as teaching assistant for “nonlinear control systems” and “introduction to control of dynamical systems” courses.

2012–2014 **Project engineering supervisor**, *Havayar Industrial Group*, Tehran, Iran

• Led a multidisciplinary engineering team of 7 members in 4 oil & gas EPC projects, each worths over $1 million.

• Negotiated technical aspects and consulted the sales department in meetings with national and international vendors and clients.

Project engineer, *Havayar Industrial Group*, Tehran, Iran

• Prepared detailed engineering documents according to ASME and API standards.

2011–2012 **System engineer**, *Turbotec*, Tehran, Iran

• Was a team-player in control system design of a turbo-compressor simulator (ABB GT10B).

2010–2011 **Mechanical engineer**, *Engine Research Institute*, Tehran, Iran

• Performed stress analysis on the connecting rod of a diesel engine (OM457LA).

Education

2014–2018 **PhD in Robotics, Control and Intelligent Systems**
Automatic Control Laboratory and Laboratory of Biomechanical Orthopedics
Ecole Polytechnique Fédérale de Lausanne, Lausanne, Switzerland
Thesis title: A closed-loop EMG-sssisted shoulder model
Thesis directors: Prof. Dominique Pioletti and Dr. Philippe Mullhaupt

2007–2010 **Master in Mechanical Engineering (Dynamics and Control)**
K. N. Toosi University of Technology, Tehran, Iran
Thesis title: Input-output selection in multivariable control systems
Thesis directors: Prof. Ali Khaki-Sedigh and Dr. Hossein Sadati

2003–2007 **Bachelor in Mechanical Engineering (Solid Mechanics)**
K. N. Toosi University of Technology, Tehran, Iran
Thesis title: Design and development of hydro-active suspension system
Thesis directors: Prof. Ali Ghaffari and Dr. Reza Kazemi

Software Tools

Dynamics systems modeling and control software: **Matlab, SimMechanics, ADAMS/View**.
Finite element analysis software: **ABAQUS, COMSOL**.
Sketching and 3D drafting software: **Solid Works, AutoCAD**.
Industrial control and monitoring software: **Labview**.
Miscellaneous software: **MS Office, Latex, Adobe Photoshop/Illustrator/Premier**.

Publications

E. Sarshari, A. Terrier, A. Farron, and P. Mullhaupt. An initialization technique for hill-type musculotendon models. *submitted to ASME Journal of Biomechanical Engineering*, (BIO-18-1186), 2018.

E. Sarshari, M. Mancuso, A. Terrier, A. Farron, P. Mullhaupt, and D. Pioletti. Motion reconstruction in upper extremity in the absence of scapula kinematics measurement-devices. *submitted to Journal of Biomechanics*, (BM-D-18-00419), 2018.

E. Sarshari, M. Mancuso, A. Terrier, A. Farron, P. Mullhaupt, and D. Pioletti. Emg-assisted load-sharing for muscle force prediction in upper-extremity. *subimtted to Journal Medical Engineering and Physics*, (MEP-D-18-00262), 2018.

E. Sarshari, M. Mancuso, A. Farron, A. Terrier, D. Pioletti, and P. Mullhaupt. Emg-based vs optimization-based prediction of muscle forces in human upper-extremity. In *8th World Congress of Biomechanics, Dublin, Irland, July 8-12*, 2018.

E. Sarshari, Y. Boulanaache, A. Terrier, A. Farron, P. Mullhaupt, and D. Pioletti. A matlab toolbox for scaled-generic modeling of shoulder and elbow. *subimtted to Journal Source Code for Biology and Medicine*, (SCBM-D-18-00009), 2018.

E. Sarshari, A. Farron, A. Terrier, D. Pioletti, and P. Mullhaupt. A simulation framework for humeral head translations. *Journal of Medical Engineering and Physics*, 49:140–147, 2017.

E. Sarshari, A. Farron, A. Terrier, D. Pioletti, and P. Müllhaupt. Application of forward-dynamics simulation to estimate humeral-head translations. In *23rd Congress of the European Society of Biomechanics, Seville, Spain, July 2-5*, 2017.

E. Sarshari, A. Farron, A. Terrier, D. Pioletti, and P. Müllhaupt. A framework for forward-dynamics simulation of the human shoulder. In *11th Conference of the International Shoulder Group, Winterthur, Switzerland, 14-16 July*, 2016.

E. Sarshari and P. Mullhaupt. Application of artificial neural networks in assessing the equilibrium depth of local scour around bridge piers. In *ASME 34th International Conference on Ocean, Offshore and Arctic Engineering, St John's, Canada, 31 May-5 June*, 2015.

E. Sarshari, D. Ingram, C. A. Engelhardt, A. Farron, D. Pioletti, A. Terrier, and P. Mullhaupt. Active stability of glenohumeral joint diminishes during the end-range motions. In *21st Congress of the European Society of Biomechanics, Prague, Czech Republic, July 5-8*, 2015.

E. Sarshari, N. Vasegh, M. Khaghani, and S. Dousti. Sliding mode control in ziegler's pendulum with tracking force: Novel modeling considerations. In *ASME International Mechanical Engineering Congress and Exposition, San Diego, California, USA, 15–21 November*, 2013.

E. Sarshari and A. K. Sedigh. Selection of sensors for hydro-active suspension system of passenger car with input–output pairing considerations. *Journal of Dynamic Systems, Measurement, and Control*, 135(1):011004, 2013.

M. Shojaeefard, I. Sohrabiasl, and **E. Sarshari**. Investigation the effect of inlet ports design on combustion characteristics and emission levels of diesel engines. *International Journal of Automotive Engineering*, 145:175, 2011.

E. Sarshari, A. K. Sedigh, and H. Sadati. Optimal control of ride comfort of a passenger car: comparison between the hydro active and the fully active suspension systems. Technical report, SAE Technical Paper, 2010.

E. Sarshari, N. Asadi, and R. Yousefi. Design of hydractive optimal suspension for a passenger vehicle. In *ASME 2010 International Mechanical Engineering Congress and Exposition,Vancouver, British Columbia, Canada, 12-18 November*, 2010.